Chapter 7: Extratropical Upper Troposphere and Lower Stratosphere (ExUTLS)

Chapter lead authors

Cameron R. Homeyer	School of Meteorology, University of Oklahoma	USA
Gloria L. Manney	(1) NorthWest Research Associates (2) New Mexico Institute of Mining and Technology	USA

Co-authors

Luis F. Millán	Jet Propulsion Laboratory, California Institute of Technology	USA
Alexander C. Boothe	(1) School of Meteorology, University of Oklahoma (2) Meteorologist, National Weather Service	USA
Tao Xian	(1) School of Meteorology, University of Oklahoma (2) School of Earth and Space Sciences, University of Science and Technology of China	USA China
Mark A. Olsen	NOAA/Oceanic and Atmospheric Research/Weather Program Office, *previously at: Goddard Earth Sciences Technology and Research, Morgan State University*	USA
Michael J. Schwartz	Jet Propulsion Laboratory, California Institute of Technology	USA
Michaela I. Hegglin	Department of Meteorology, University of Reading	United Kingdom
Zachary D. Lawrence	(1) Cooperative Institute for Research in Environmental Sciences (CIRES), Univ. of Colorado (2) NOAA Physical Sciences Laboratory (PSL) (3) NorthWest Research Associates	USA
Krzysztof Wargan	(1) Science Systems and Applications Inc. (2) Global Modeling and Assimilation Office, NASA Goddard Space Flight Center	USA

Abstract. The ExUTLS is an important region for understanding the impacts of and feedbacks to anthropogenically forced climate change. Modern reanalyses provide output at vertical resolution that facilitates detailed examination of the ExUTLS and the myriad dynamical, chemical, and physical processes that occur in this layer. This chapter compares diagnostics of many ExUTLS processes in modern reanalysis datasets. The diagnostics include characterization of the tropopause based on different definitions (including multiple tropopauses, vertical structure, comparison of temperature-gradient based tropopause characteristics with radiosonde observations, *etc.*); UTLS jet characteristics and long-term changes; atmospheric transport from trajectory model calculations; and diagnostics of mixing and stratosphere-troposphere exchange (STE). In addition, assimilated UTLS ozone from recent reanalyses is evaluated and compared with satellite observations. Overall results highlight the importance of using high-resolution (particularly in the vertical) reanalyses on their native grids to capture many ExUTLS processes including tropopause structure and evolution. Most of the diagnostics evaluated show the MERRA-2, ERA-Interim, JRA-55, and CFSR/CFSv2 reanalysis to be suitable for UTLS studies with some limitations; in particular, CFSR/CFSv2 does not agree well with the other reanalyses for several of the diagnostics. While useful information on trends in the tropopause and jet characteristics was obtained, great caution is urged in conducting trend studies from reanalyses, and agreement among several reanalyses is one of the key elements for assessing robustness of the ExUTLS trends shown here.

Contents

7.1 Introduction

The ExUTLS is a layer of large dynamical, chemical, and physical variability in the atmosphere. It is the transition between the often turbulent, well-mixed troposphere and the relatively quiescent and stratified stratosphere (*e.g.*, *Gettelman et al.*, 2011). Discontinuities in vertical temperature gradients, trace gas concentrations, and occurrence of clouds exist in this layer and are generally centered near the extratropical tropopause. Dynamical processes that lead to mixing between the upper troposphere (UT) and lower stratosphere (LS) can lead to changes in the chemical characteristics of this layer and, ultimately, its radiative forcing. Namely, several key trace gases that are also greenhouse gases have dominant sources that are confined to either the troposphere or stratosphere: H_2O is prevalent in the troposphere and Earth's radiative forcing is most sensitive to changes in its concentration in the LS (*e.g.*, *Solomon et al.*, 2010; *Forster and Shine*, 1999). O_3 is prevalent in the stratosphere and Earth's radiative forcing is most sensitive to changes in its concentration in the UT (*e.g.*, *Lacis et al.*, 1990). *Riese et al.* (2012) showed that the radiative effects of both O_3 and H_2O are sensitive to mixing processes in the UTLS.

The separation between the tropical UTLS (often referred to as the "Tropical Tropopause Layer" or TTL) and the ExUTLS is often based on the location of the subtropical jets in each hemisphere or the tropopause break (the sharp discontinuity in lapse rate tropopause altitude between tropics and extratropics); that separation is thus the region where the isentropes slope sharply downward with increasing latitude. This chapter focuses on the ExUTLS as defined in this manner (*i.e.*, poleward of the subtropical jet and tropopause break), while *Chapter 8* focuses on the TTL. Processes related to tropical width and monsoon evolution occur at the interface between these two regions, and, because of their close ties to tropical circulations, are discussed primarily in *Chapter 8*. Because the UTLS is strongly coupled to the troposphere below and the stratosphere above, the altitude region we focus on here extends from below the high-latitude tropopauses to above the tropical tropopauses, thus, very roughly, from about 300 hPa to 70 hPa.

The definition of the tropopause (outlined further below) is a necessary element of any UTLS study. Its location defines the transition from troposphere to stratosphere (and, as a result, the depth and altitude location of the UTLS region) and enables further analysis of topics such as transport, composition, dynamics, and their collective impacts on radiation and climate. For example, trace gas profiles and stratosphere-troposphere exchange (STE) are commonly evaluated in a tropopause-relative altitude framework (*e.g.*, *Pan et al.*, 2010; *Hegglin et al.*, 2006; *Hoor et al.*, 2004). Assessing the accuracy of tropopause altitudes and evaluating appropriate methods of defining the tropopause for various applications are thus important focuses of recent and ongoing research using reanalyses.

STE is often assessed in reanalyses by coupling their three-dimensional wind fields with a trajectory model or through nudging CTMs with reanalysis output and including passive tracers. Many ExUTLS studies focus on individual, large-scale STE processes that are resolved in the reanalyses, such as Rossby wave breaking (RWB; *e.g.*, *Kunz et al.*, 2015; *Homeyer and Bowman*, 2013; *Song et al.*, 2011; *Sprenger et al.*, 2007; *Hitchman and Huesmann*, 2007), stratospheric intrusions or tropopause folds (*e.g.*, *Knowland et al.*, 2017; *Škerlak et al.*, 2015; *Sprenger et al.*, 2003), and extratropical cyclones (*e.g.*, *Jaeglé et al.*, 2017; *Reutter et al.*, 2015). Some studies point to long-term changes in these STE processes, which are important to consider in the context of a changing climate because of their impacts on the radiation budget through changes in the distribution of UTLS water vapor, ozone, and additional greenhouse gases (*e.g.*, *Orbe et al., 2018*; *Zeng et al.*, 2010; *Hegglin and Shepherd*, 2009). Smaller scale phenomena (*e.g.*, shearing instabilities, gravity wave breaking associated with tropopause-penetrating convection) have received increasing attention in ExUTLS research (*e.g.*, *Kunkel et al.*, 2019; *Homeyer et al.*, 2017; *Wang et al.*, 2016a), but these processes will not be evaluated in reanalyses until grid resolution meets the scales necessary to resolve such processes. However, tropopause altitudes from reanalyses (and other global models) are often used in observational studies of such phenomena.

The ExUTLS is particularly important because changes in radiatively active trace gases in the region are important drivers of climate variability and change. *Chapter 4* and *Davis et al.* (2017) did not focus much on the UTLS, but did show zonal mean ozone evaluations that indicated persistent biases in the UTLS, as well as deficiencies in their ability to capture the seasonal cycle of ozone. We include some further evaluations of UTLS ozone here, particularly in dynamical coordinate (EqL, tropopause, jet-relative) frameworks. *Chapter 4* and *Davis et al.* (2017) showed water vapour in the reanalyses evaluated here to be generally unsuitable for scientific use, so we do not further evaluate reanalysis water vapour in the UTLS.

7.2 Reanalyses and General Approach

In situ observations of composition and transport events are historically sparse. As a result, reanalyses are the primary source of input for climatological studies of the ExUTLS. UTLS processes in general involve very strong dynamical and chemical gradients, and thus require fine resolution to properly resolve. Older reanalyses (such as NCEP-R1, NCEP-R2, and ERA-40) not only have inadequate resolution in both the horizontal and vertical, but also are usually not available on model levels. *Manney et al.* (2017; see *Sections 7.3.3* and *7.4.2* below) showed that even the latest generation high resolution reanalyses do not capture tropopause and UTLS jet structure when interpolated to a standard pressure grid.

Because of the strong dependence on resolution, we use only the latest generation high-resolution reanalyses in this chapter; these comprise MERRA, MERRA-2, ERA-Interim, CFSR/CFSv2, and JRA-55. For most diagnostics (exceptions will be noted) the reanalyses are used on (or, in the case of spectral models, near) the full model horizontal resolution and on the model vertical grid. For detailed information on model grids and configurations, please see *Chapter 2* and *Fujiwara et al.* (2017); we briefly summarize the most relevant aspects here. The horizontal resolution for these reanalyses is 0.5×0.67, 0.5×0.625, 0.75×0.75, 0.5×0.5, and approximately 0.56x0.56 degrees; the JRA-55 dataset is provided on the Gaussian grid corresponding to the model horizontal resolution. The vertical resolution of these reanalyses in the ExUTLS ranges from about 0.8km to about 1.5km, varying with reanalysis and altitude (Figure 2.1 of *Chapter 2*; Figure 3 of *Fujiwara et al.*, 2017): CFSR/CFSv2 vertical spacing increases gradually from about 0.6km at 7km altitude to about 0.95km at 20km altitude; ERA-Interim and JRA-55 have very similar vertical grids, increasing smoothly from about 0.6km at 7km altitude to about 1.4km at 20km altitude; MERRA and MERRA-2 increase rapidly from about 0.6km at 7km altitude to about 1.2km at 9km altitude and remain nearly constant above that up to above 20km altitude. Details of the assimilation systems, data inputs and reanalyses are given in *Fujiwara et al.* (2017) and *Chapters 2* and *4*.

Most of the comparisons shown here are done starting in 1979 or 1980, and the end dates vary from 2010 to 2015. As noted in *Chapter 3* and *Long et al.* (2017) (as well as several other chapters), some diagnostics show significant changes in reanalysis agreement over the 30 - 40-year periods studied here, generally in relation to large changes in the reanalysis data inputs. Except where specifically noted, most of the diagnostics in this chapter do not show strong sensitivity to the exact time period analyzed, or to such changes in the reanalysis inputs. A few diagnostics are computed for shorter time periods to compare with observational datasets with more limited records.

The reanalyses used have very different treatments of, and inputs for, ozone that affect the UTLS, as described in detail in *Fujiwara et al.* (2017), *Davis et al.* (2017), and *Chapter 4*. Of particular relevance to this chapter is that MERRA-2 assimilates Aura MLS profile and OMI total column ozone after October 2004, and ERA-Interim assimilates these ozone data in 2008 and the near real time (NRT) MLS ozone data starting in mid-2009. *Davis et al.* (2017) and *Chapter 4* show results that suggest persistent biases in assimilated ozone in the UTLS, which are not generally well understood given increasing uncertainties in ozone observations in this region.

7.3 The Extratropical Tropopause

Tropopause altitudes are critical to ExUTLS transport studies, especially those leading to STE. Due to their global and continuous coverage, reanalyses have often been used to identify the tropopause for observational and modeling-based transport studies. Differences in assimilation and model design (*e.g.*, grid resolution) between reanalyses result in differing tropopause altitudes. Incorrect tropopause altitudes can lead to significant biases in transport estimates owing to the typically strong gradients in trace gases at the tropopause level. Thus, it is important to evaluate the accuracy of reanalysis tropopause altitudes and identify the similarities and differences between reanalyses to inform their uses in ExUTLS studies.

Many previous studies have employed unique methods to determine the altitudes of the tropopause. In the ExUTLS these methods can be summarized into 5 general types:

1. Temperature lapse rate: this approach identifies changes in vertical temperature gradients (or lapse rates) to distinguish the well-mixed troposphere from the stably stratified stratosphere. The most common lapse-rate tropopause definition is that outlined by the WMO (*World Meteorological Organization*, 1957). Issues related to its application with model output are outlined in *Homeyer et al.* (2010).

2. Potential vorticity (PV) isosurface: often referred to as the 'dynamical tropopause', this approach depends largely on atmospheric stability but enables unique tracking of air mass history since PV is quasi-conserved over time periods of several days. It is most commonly used in transport analyses. Recent efforts have also used a PV gradient approach to identify the tropopause, especially for studies that evaluate isentropic transport (*e.g.*, *Kunz et al.*, 2011b).

3. Chemical tropopause: this approach identifies changes in atmospheric composition with height. In observations, ozone is typically used as it is often uniformly low in the troposphere but increases rapidly with altitude in the lower stratosphere (*e.g.*, *Bethan et al.*, 1996). In models, an artificial tracer with sources at the lower boundary is typically used to identify the chemical transition associated with the tropopause (*e.g.*, *Prather et al.*, 2011).

4. Stability transition: this approach is similar to the temperature lapse rate in that it identifies the sharp change in static stability between troposphere and stratosphere, but it depends on the Brunt-Vaisälä frequency. Some studies identify the stability transition using curve-fitting techniques (*e.g.*, *Homeyer et al.*, 2010) and others simply search for the LS stability maximum in combination with the temperature lapse rate definition (*e.g.*, *Gettelman and Wang*, 2015).

5. Lagrangian tropopause: this approach uses a trajectory model to determine the fraction of particles in a given volume that have recently (within the prior 15 - 60 days) been located within the planetary boundary layer and is similar to the Eulerian artificial tracer approach for the chemical tropopause. The time period used for trajectory calculation is fixed for this method and is commonly 30 days (*e.g.*, *Berthet et al.*, 2007).

Regardless of the method used to identify the extratropical tropopause, its altitude commonly spans a range from ~8 km to ~13 km (350 hPa > p > 150 hPa). Temperatures of the extratropical tropopause are typically between 205 K and 225 K.

Several of the diagnostics and evaluations shown below use tropopauses calculated within the JETPAC (JEt and Tropopause Products for Analysis and Characterization) software package (*Schwartz et al.*, 2015; *Manney et al.*, 2014, 2011). In JETPAC, the dynamical tropopause is defined by PV values in the extratropics from 2.0 to 6.0 PVU, joined with the 380 K PV contour in the tropics; the PV values cover the range that has been widely used (*e.g.*, *Schoeberl*, 2004; *Highwood et al.*, 2000). The primary lapse rate tropopause is defined using the WMO definition. Multiple lapse rate tropopauses are then identified if dT/dz drops below -2 K km^{-1} after (that is, at a higher altitude) remaining below it for at least 2 km above the primary lapse rate tropopause, and then rises above -2 K km^{-1} again; *Randel et al.* (2007a) showed that this criterion results in a climatology of multiple tropopauses in (relatively coarse-resolution) meteorological analyses comparable to that from high-resolution measurements.

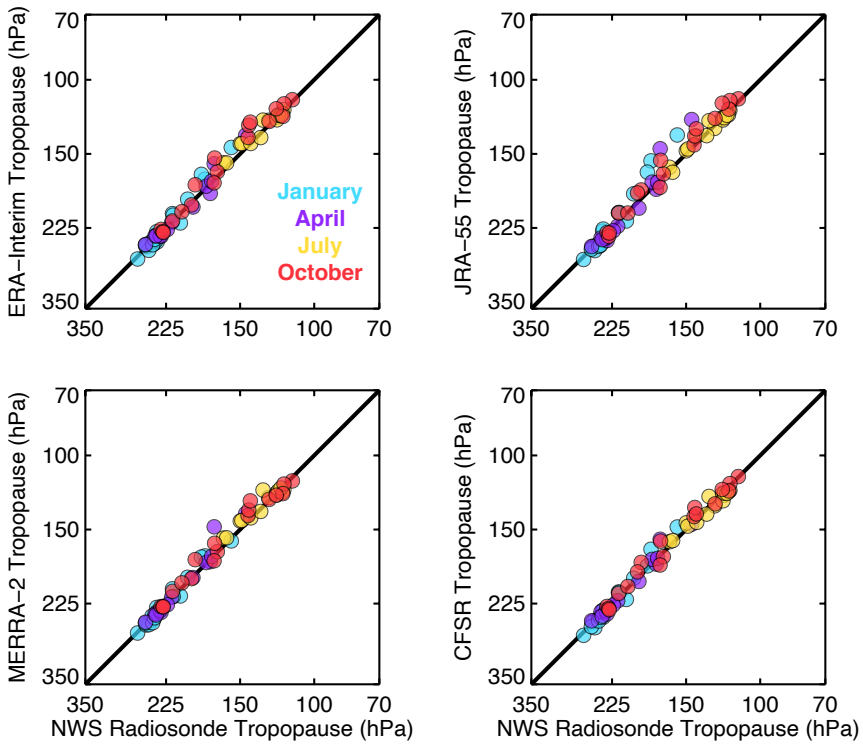

Figure 7.1: *Scatterplots of monthly mean WMO lapse-rate tropopause pressure from reanalyses and NWS radiosondes over the CONUS. Results for ERA-Interim, JRA-55, MERRA-2, and CFSR are shown from January 2001 to October 2001 in 3-month increments. The thick black lines are 1-to-1 lines. The comparisons are only for NWS stations with a continuous record of observations throughout each month (typically ~15 out of ~50).*

7.3.1 Lapse Rate Tropopause Altitudes

The uncertainty (*i.e.*, error) of the tropopause altitude calculated using numerical model output such as that from a reanalysis (based on comparisons with radiosonde observations) is typically comparable to the vertical resolution of the model in the UTLS (*e.g.*, *Xian and Homeyer*, 2019; *Solomon et al.*, 2016; *Homeyer*, 2014; *Homeyer et al.*, 2010). For ERA-Interim, JRA-55 and CFSR/CFSv2, the expected uncertainty in the extratropical tropopause altitude is therefore ~800 m, while it is ~1000 m in MERRA-2. For more information on differences in grid resolution, see *Section 7.2*, *Chapter 2* and Figure 3 of *Fujiwara et al.* (2017). In addition to uncertainty, it is important to assess the accuracy of tropopause altitudes in the reanalyses. Such an assessment is typically done by determining the bias in tropopause altitude through comparisons of the reanalysis tropopause altitudes with those computed from high-resolution radiosonde observations.

Figure 7.1 shows comparisons of monthly mean tropopause altitudes from four modern reanalyses (ERA-Interim, JRA-55, MERRA-2, and CFSR) with those computed using operational high-resolution National Weather Service (NWS) radiosondes in the Contiguous United States (CONUS). These comparisons are valid for four months from a single year, but the results are comparable to those from alternative months within all years examined (2001 - 2010; not shown). In particular, this comparison reveals that reanalysis tropopause altitudes are largely unbiased, while some unique biases can be found throughout the year. Namely, there is some evidence of a slight high bias for tropopause altitudes near ~150 hPa during NH winter (DJF) and spring (MAM) in each reanalysis, with the largest such biases commonly found in JRA-55. *Xian and Homeyer* (2019) show similar comparisons for instantaneous tropopause identifications using a global set of long-term radiosonde observations and find that MERRA-2 tropopauses are most often biased high, while the remaining reanalyses are most often biased low. Errors in instantaneous tropopause altitudes in all reanalyses are greatest in the subtropics (*i.e.*, the transition between the ExUTLS and TTL). Globally, the average instantaneous tropopause error (rms difference) is ~1 km in all modern reanalyses.

To examine differences in reanalysis tropopause altitudes at a larger scale, global comparisons of monthly mean tropopause altitudes from several combinations of the ERA-Interim, JRA-55, CFSR, and MERRA-2 reanalyses are shown in **Figure 7.2**.

These comparisons correspond to the same time period as that in **Figure 7.1** and reveal that reanalyses that share a common vertical grid agree on the location of the tropopause. Most reanalysis tropopause comparisons closely follow each other in NH winter and spring, but deviate in the ~225 to ~100 hPa altitude range in NH summer (JJA) and fall (SON). These differences occur near the common location of the tropopause break within the SH (not shown). As is true for the analysis presented in **Figure 7.1**, these results are found consistently throughout the reanalysis record.

Long-term changes in the extratropical tropopause temperature and/or altitude are an indication of climate change and are relevant to the assessment of transport and other ExUTLS processes. *Xian and Homeyer* (2019) evaluate long-term changes in the WMO lapse-rate tropopause altitude during the period 1981 to 2015 and show that ERA-Interim, JRA-55, and MERRA-2 indicate similar changes in magnitude, pattern, and sign, while CFSR provides a substantially different picture. They also show that trends in each reanalysis are broadly consistent with radiosonde observations, but the extent of patterns is not yet known given the relatively poor global coverage of such observations. **Figure 7.3** shows these 35-year trends from ERA-Interim, JRA-55, MERRA-2, and CFSR in a tropopause break-relative latitude coordinate, which enables assessment of tropopause altitude changes within tropical and extratropical reservoirs (*i.e.*, ExUTLS alone). Trends are mostly positive (*i.e.*, tropopause altitudes are increasing) for the three reanalyses in agreement, with the greatest changes found within the tropics and extratropical Pacific. It is not yet clear how these patterns are affected by changes in UTLS dynamics or regional variations in tropospheric heating.

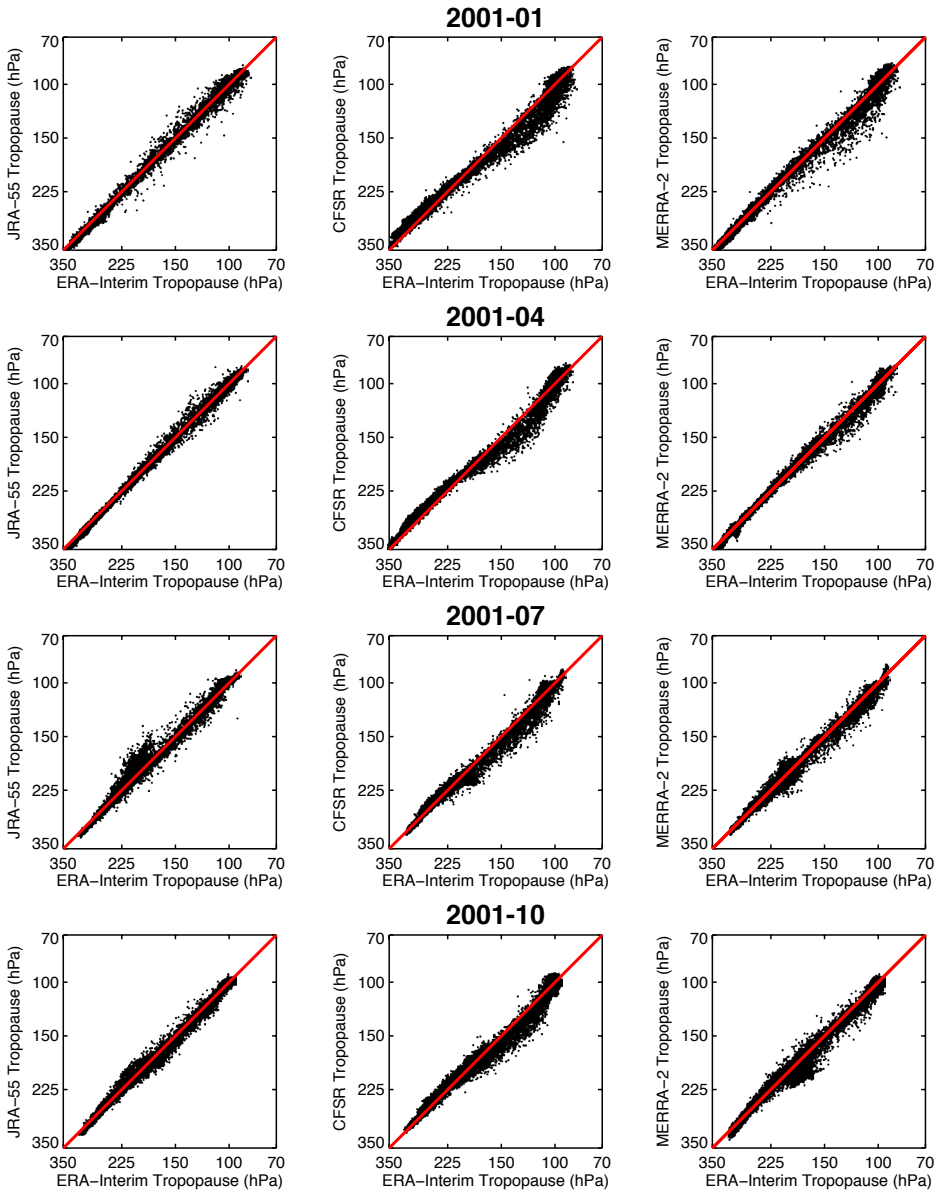

Figure 7.2: *Scatterplots comparing global monthly mean WMO lapse-rate tropopause pressures from multiple reanalyses. Comparisons are given left to right between JRA-55 and ERA-Interim, CFSR and ERA-Interim, and MERRA-2 and ERA-Interim, respectively. Results for January 2001 to October 2001 in 3-month increments are provided from top to bottom. The red lines are 1-to-1 lines.*

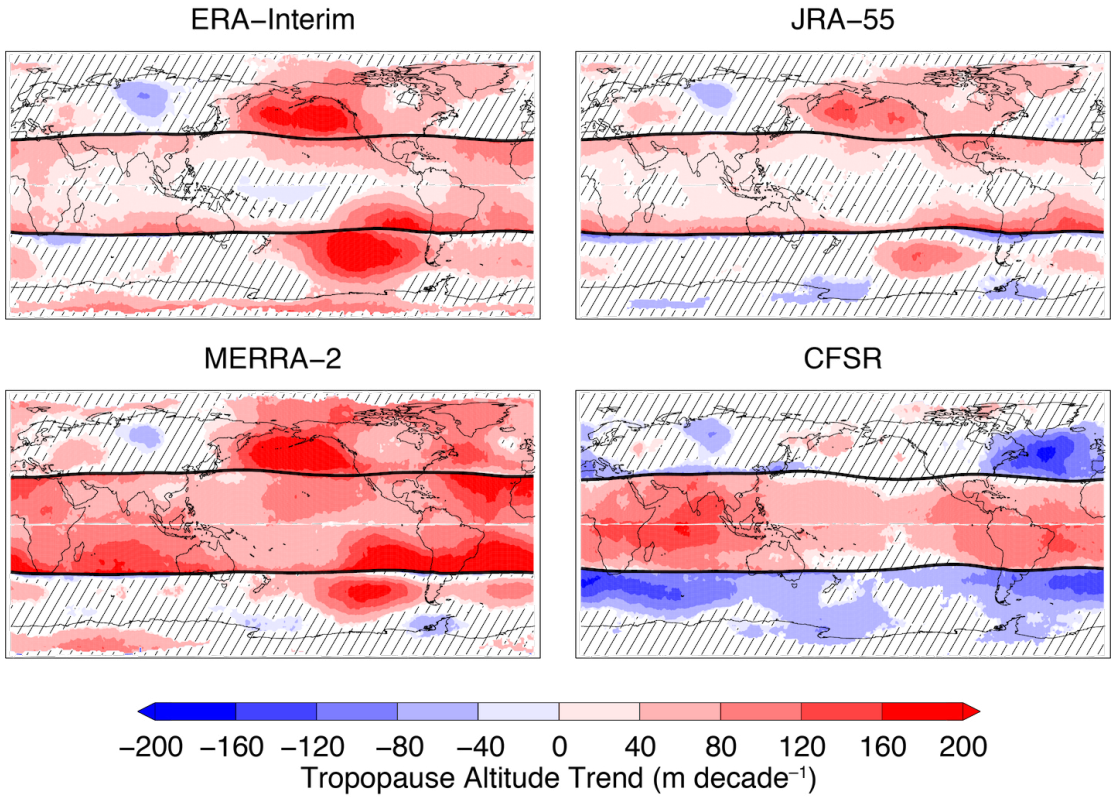

Figure 7.3: *Figure 5 from Xian and Homeyer (2019). Maps of 35-yr (1981 - 2015) trends in the WMO lapse-rate tropopause altitude in a tropopause break-relative latitude coordinate from four modern re- analyses: ERA-Interim, JRA-55, MERRA-2, and CFSR. Color-filled regions are statistically significant at the 99 % level. Thick black lines show the annual-mean tropopause break latitudes for each reanalysis.*

7.3.2 Dynamical Tropopause Altitudes

The dynamical tropopause is typically defined by a three-dimensional contour of PV in the extratropics, joined with an isentropic surface, usually 380 K, in the tropics (*i.e.*, where the PV contour lies at higher potential temperature or is ill-defined). The most appropriate PV value to use depends on the focus of the study and on latitude, with higher values (*e.g.*, 4.5 PVU) typically lying near the lapse rate tropopause at higher latitudes. Furthermore, *Kunz et al.* (2011a) found that the barrier to isentropic transport was at higher PV (up to about 5.5 PVU) on higher potential temperature levels. Here we have compared the dynamical tropopauses using 1.5, 2.0, 3.5, 4.5, and 6.0 PVU in the extratropics joined with the 380 K isentropic surface in the tropics (the tropopause calculations are from JETPAC, described by *Manney et al.*, 2011). Qualitatively similar results were found for each of the tropopause values, with lower values usually showing slightly larger differences between the reanalyses. The examples shown below are for 2.0 PVU, one of the most commonly used values for a PV-based tropopause. To assess differences that could be related to the large increases in input data sources and changes from TOVS to ATOVS in the 1998 through 2002 time frame (see, *e.g.*, *Chapters 2* and *3*, and *Fujiwara et al.*, 2017; *Long et al.*, 2017), we examined climatologies for two separate 8-year periods, 1986 - 1993 and 2003 - 2010; the results showed no substantial differences in patterns of reanalysis agreement between the periods, so we show only the full comparison period here. We compare MERRA-2, ERA-Interim, JRA-55, and CFSR/CFSv2 for 1980 - 2014; the tropopauses are calculated using the data on the full model grid but averaged in 2-degree bins for the comparisons.

Figure 7.4 shows climatological dynamical tropopause altitude maps for DJF and JJA, showing the REM (the average of the four reanalyses used) and the differences of each of the reanalyses from the REM (reanalysis - REM, so positive values indicate that the reanalysis tropopause altitude is higher than that of the REM). In both seasons, the differences from the REM are generally less than 0.2 km over most of the globe, with some regions near 30°N and 30°S (near the latitude of the tropopause break in LRT, where the dynamical tropopause height also drops sharply) showing larger differences (magnitudes up to about 1.5 km). The relatively large differences in the tropopause break region primarily arise from small differences in the latitude location of the sharp gradient in tropopause altitudes. These differences are most prominent in CFSR/CFSv2 and JRA-55 in the regions where the subtropical jets are climatologically strongest (see, *e.g.*, *Manney et al.*, 2014), *i.e.*, in the NH over Africa and Asia in DJF, and in the same longitude region in both hemispheres in JJA.

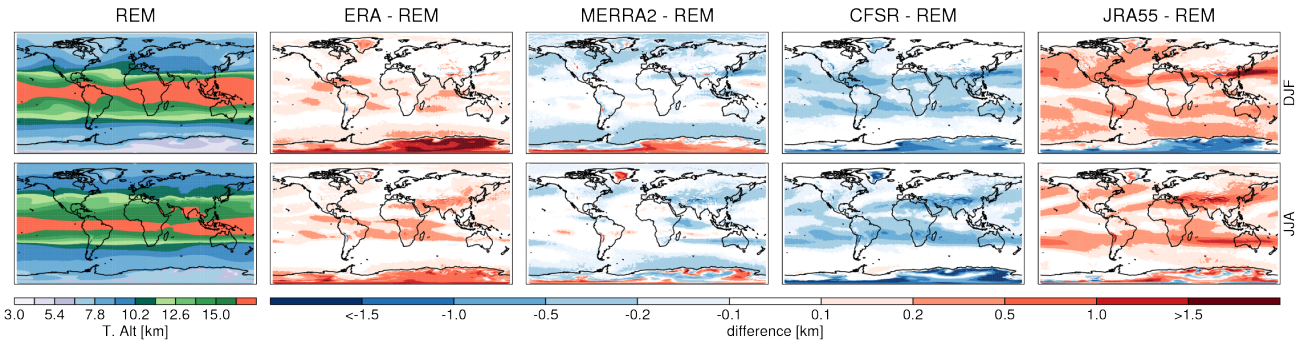

Figure 7.4: *Climatological (1980 - 2014) 2 PVU tropopause altitudes for DJF (top row) and JJA (bottom), from the REM for the four reanalyses, and (second through right panels) the difference of each reanalysis from the REM (reanalysis – REM) for that climatological period. Adapted from Millán et al. 2021.*

In general ERA-Interim and JRA-55 have higher, and MERRA-2 and CFSR/CFSv2 lower, dynamical tropopauses than the REM, except over Antarctica in DJF, where MERRA-2 (JRA-55) is higher (lower). CFSR/CFSv2 shows very low and MERRA-2 very high dynamical tropopauses over Greenland in JJA, with values up to about 1.5 km from the REM. The exception to the good agreement among the reanalyses is over large portions of Antarctica, where ERA-Interim and CFSR/CFSv2 show positive and negative differences, respectively, from the REM in both seasons, with magnitudes of over 3 km for ERA-Interim in DJF and CFSR/CFSv2 in JJA. In DJF, MERRA-2 and JRA-55 show opposite-signed differences from the REM over Antarctica than they do over the rest of the globe, with smaller differences that vary in sign locally in JJA. Because both LRT and dynamical tropopauses are often somewhat ill-defined in the polar regions, especially during winter, and conventional data inputs (*e.g.*, high resolution radiosonde temperature profiles that help capture the vertical structure) to the reanalyses are sparser (especially over Antarctica), larger disagreements in the Antarctic are not surprising. In general, there are no dramatic differences in the agreement among reanalyses between the early and late periods, though there is a small decrease in the range of differences from the REM in the Antarctic (not shown). The lack of difference before to after the TOVS/ATOVS transition mentioned above (not shown) indicates that the increases in data inputs that so profoundly affect reanalysis differences in Antarctic temperature values (*e.g.*, *Lawrence et al.*, 2018; *Long et al.*, 2017) do not have a strong influence on the PV values demarking the tropopause. Similarly, *Xian and Homeyer* (2019) found no apparent (or significant) trends, steps or discontinuities in the LRT time series in the Antarctic associated with changes in data inputs.

Figure 7.5 shows frequency distributions of each of the four reanalyses versus the REM for DJF and JJA. All of the reanalyses cluster strongly around the one-to-one line with the REM, as expected given the generally good agreement seen in the climatological maps. The largest departures from the REM are seen for low REM tropopause altitudes, below about 8 km, where the distributions for each of the reanalyses become quite wide, indicating considerable uncorrelated variability among the reanalyses in the lowest tropopause altitude values.

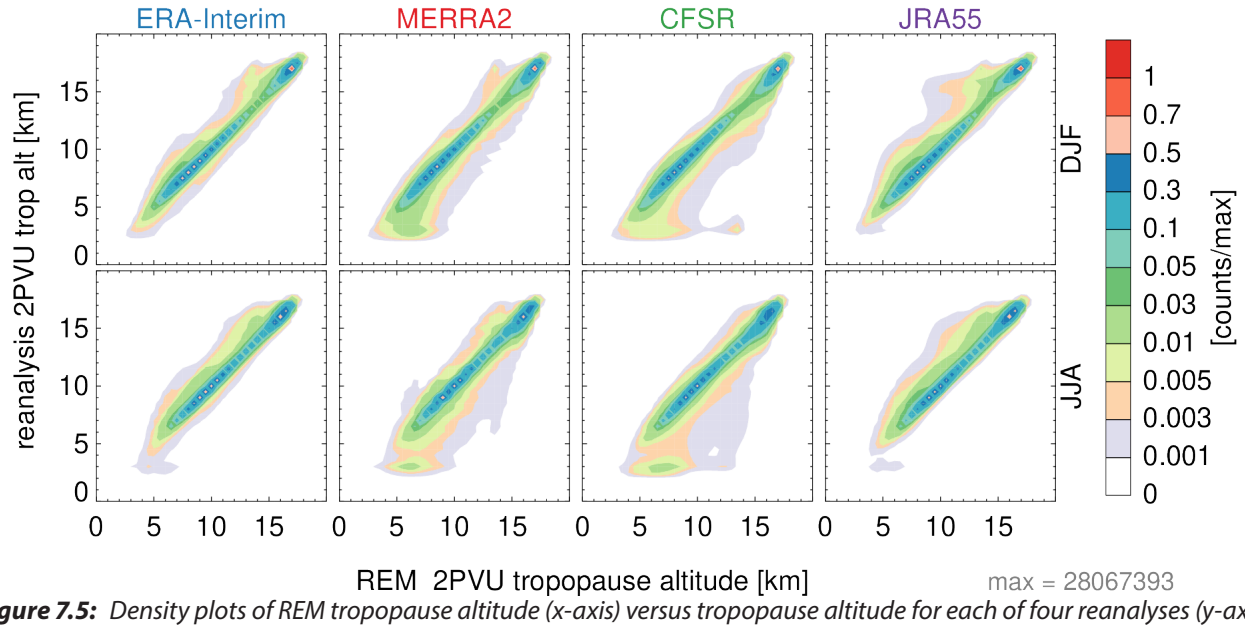

Figure 7.5: *Density plots of REM tropopause altitude (x-axis) versus tropopause altitude for each of four reanalyses (y-axis), for DJF (top) and JJA (bottom), for 1980 - 2014. Adapted from Millán et al. 2021.*

7.3.3 Multiple Tropopauses

Manney et al. (2017) examined the climatology of multiple lapse rate tropopauses identified using the JETPAC tools, as described above. Regions with multiple tropopause altitudes occurring in the altitude layer between approximately 10 km and 20 km have been linked with poleward transport of tropical upper tropospheric air into the extratropical lower stratosphere (*e.g.*, *Homeyer et al.*, 2011; *Pan et al.*, 2009; R*andel et al.*, 2007b) and with poleward RWB (*e.g.*, *Homeyer and Bowman*, 2013).

Figure 7.6 shows comparisons of zonally averaged multiple tropopause frequency distributions over the seasonal cycle from multiple reanalyses. As described in detail by *Manney et al.* (2017), the frequency distributions (here and in other JETPAC-based frequency distribution plots shown later) are normalized based by dividing by the total number of points that would "fill" each bin, thus in this case the number of grid points and days in each bin (latitudes × longitudes × years). We compute differences of MERRA, ERA-I, JRA-55, and CFSR/CFSv2 from MERRA-2, the most recent of the reanalyses used. Differences are fairly large among the reanalyses, and depend largely on vertical resolution and grid spacing in the UTLS, which is significantly different among the reanalyses (see *Chapter 2*, Figure 2.1, and *Fujiwara et al., 2017*, Figure 3). In the NH, smallest differences are seen between MERRA and MERRA-2, which share a vertical grid in addition to being different versions of the same data assimilation system/model. JRA-55 generally shows fewer multiple tropopauses than MERRA-2 and CFSR/CFSv2 generally shows more. CFSR/CFSv2 shows many more multiple tropopauses in the tropics than any of the other reanalyses. In the SH winter and spring, MERRA, ERA-Interim, and CFSR/CFSv2 show substantially lower multiple tropopause frequencies than MERRA-2 in mid-latitudes and substantially higher multiple tropopause frequencies in the south polar region; the pattern is similar in JRA-55 but muted because of the overall lower frequencies.

Manney et al. (2017) showed that these differences are relatively zonally symmetric, especially in the SH. Vertical cross-sections of multiple tropopauses (*Manney et al.*, 2017) indicate that MERRA-2 shows more sharply peaked secondary tropopause altitudes, leading to a layered pattern of differences with the other reanalyses; these differences were larger in the period before the TOVS/ATOVS transition, suggesting that they are related to differences in the temperature structure related to reanalysis input changes (as shown in zonal means by, *e.g.*, *Long et al.*, 2017, also see *Chapter 3*). *Manney et al.* (2017) also evaluated multiple tropopauses in JRA-55C versus JRA-55 and found large differences (up to about 30 %) in SH middle to high latitudes, with high-latitude multiple tropopauses clustered in different longitude regions. In addition, *Manney et al.* (2017) showed that CFSR/CFSv2 interpolated to pressure levels (which significantly degrades the vertical resolution) does very poorly at representing multiple tropopauses, with much lower frequency distributions (see *Section 7.4.2* and **Figure 7.11** below).

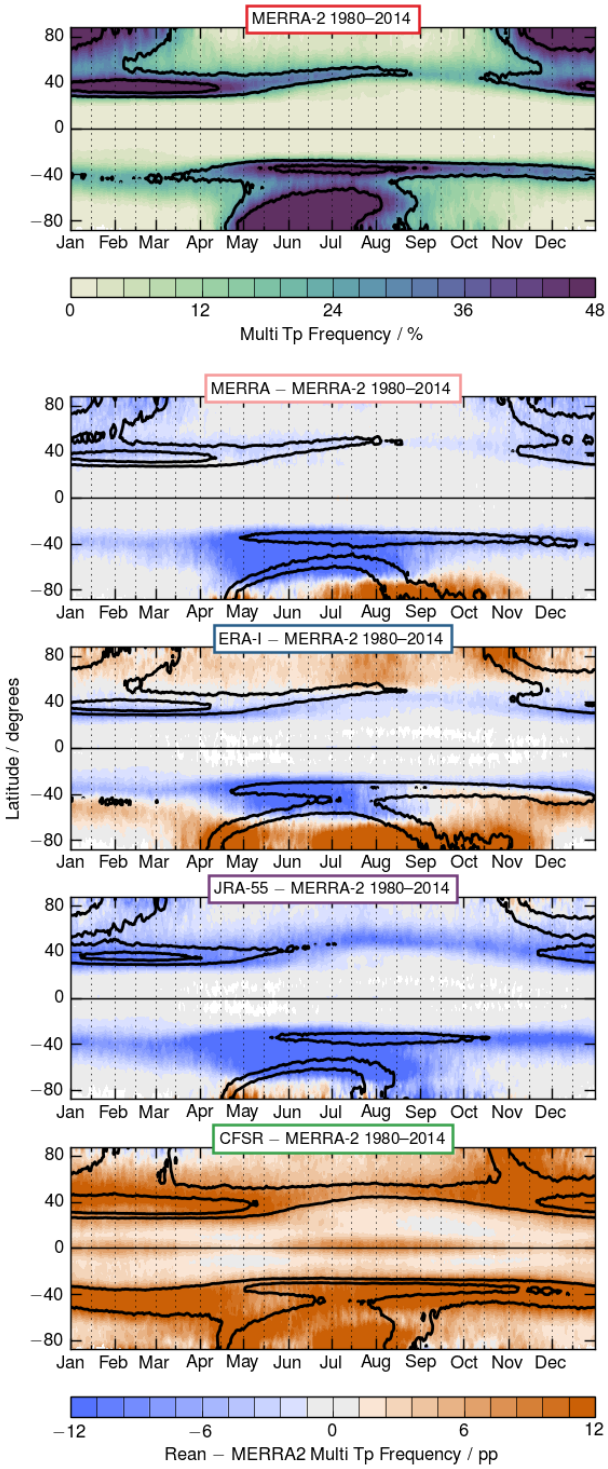

Figure 7.6: *Climatological seasonal cycle of zonally averaged frequency distributions of multiple tropopauses from MERRA-2 (top), and differences between those frequency distributions and the other reanalyses (remaining rows). Black overlays show frequency contours of 24 % and 48 %, for the reanalysis in each panel. The differences are expressed in "percentage points" (see Manney et al., 2017) to indicate that they are the absolute differences of va1l4ues initially expressed as a percent. (Adapted from Manney et al., 2017).*

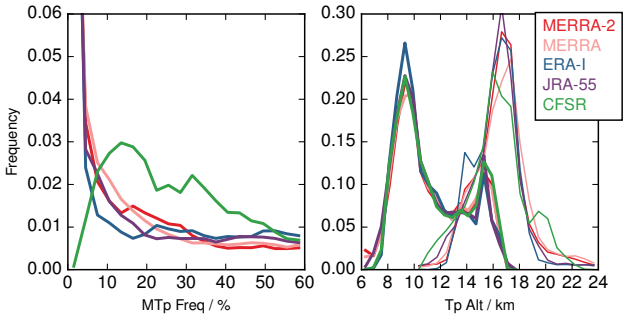

Figure 7.7: *Summary of globally / seasonally averaged frequency distributions of multiple tropopause frequencies (left) and altitudes (right; primary tropopause thick lines, secondary tropopause thin lines) in five reanalyses. (Adapted from Manney et al., 2017).*

Global annual mean multiple tropopause frequency differences are summarized in **Figure 7.7**. In this broad average, the multiple tropopause frequency distributions agree fairly well among the reanalyses except for CFSR/CFSv2, which shows many fewer instances of low multiple tropopause frequencies and many more of high ones than the other reanalyses, reflecting the patterns (especially the large frequencies in low latitudes) seen in **Figure 7.6**. The primary tropopause altitudes show good agreement on average for all of the reanalyses. The same is mostly the case for secondary tropopause altitudes, except that ERA-Interim shows a secondary peak near 14 km and CFSR/CFSv2 shows a lower frequency of peaks near 16 - 18 km and a secondary peak near 20 km.

Figures 7.8 and **7.9** show 2005 - 2015 climatologies of dynamical fields from the MERRA-2, ERA-Interim, JRA-55, and CFSR/CFSv2 reanalyses at the measurement locations of the Aura Microwave Limb Sounder (MLS), along with MLS ozone in multiple tropopause regions as identified in JETPAC using each of the reanalyses' temperature profiles at the MLS measurement locations; the differences of these profiles from the REM of those four reanalyses are also shown. The profiles are screened and interpolated to MLS locations as described by *Schwartz et al.* (2015), wherein multiple tropopauses associated with the extreme thermal structure under the winter polar vortices are screened out. Generally similar results are seen in other seasons. In both hemispheres, there are typically larger differences among the reanalyses in multiple tropopause than in single tropopause regions. JRA-55 stands out as usually having larger differences from the REM than the other reanalyses, especially in the NH. For many of the fields, MERRA-2 and ERA-Interim are closer to the REM, with JRA-55 and CFSR/CFSv2 showing opposite extremes. The temperature differences from the REM in the UTLS range up to about 0.8 K in single tropopause regions and nearly 2 K in double tropopause regions. As can be deduced from the ozone profiles, which are the same ozone data but averaging the profiles identified as single and double tropopause regions in each reanalysis, the reanalyses show significant differences in which profiles are identified as having double tropopauses, and these differences have implications for using reanalysis dynamical fields in analysis of trace gas observations. Reanalysis ozone in multiple tropopause regions is discussed below in *Section 7.6.1.*

The tropopause inversion layer (TIL), a region of enhanced static stability just above the primary LRT (*e.g.*, *Birner et al.*, 2006) is clearly seen in all of the reanalyses evaluated here (*Schwartz et al.,* 2015, also noted good representation of the TIL in MERRA and in operational GMAO analyses of that generation), in contrast to the poor representation in older reanalyses evaluated by *Birner et al.* (2006); this is in agreement with the findings of *Pilch Kedzierski et al.* (2016), who showed that ECMWF operational analyses and ERA-Interim substantially improved the TIL representation over earlier reanalyses. Indeed, several other recent studies have shown the latest generation of reanalyses to be useful for studying TIL variability and evolution (*e.g.*, *Wargan and Coy*, 2016; *Wang et al.*, 2016b; *Gettelman and Wang*, 2015). The TIL is generally strongest in CFSR/CFSv2 and weakest in JRA-55, but in each case shown still appears to be somewhat weaker than seen in high resolution data such as GNSS-RO, as was found by *Pilch Kedzierski et al.* (2016) and as is consistent with the climate model results of *Hegglin et al.* (2010). The distance above the primary tropopause appears to be similar to that seen in GNSS-RO data (GNSS-RO analyses are shown by *Wang et al., 2016b*; *Pilch Kedzierski et al.*, 2016; *Hegglin et al.*, 2010) for the reanalyses evaluated here. Our evaluations indicate that differences in TIL representation among the reanalyses cannot be attributed solely to differences in the vertical resolution, since MERRA and MERRA-2 have somewhat coarser vertical resolution in this region than the other three reanalyses evaluated here (*Chapter 2*, *Section 7.2* and *Fujiwara et al.*, 2017), yet do not show the weakest TIL; this is consistent with other studies (*e.g.*, as shown for climate models by *Hegglin et al., 2010*), and suggests a dependence on differences in the data assimilation procedures, which is also supported by the studies cited above.

Xian and Homeyer (2019) evaluate long-term changes in double tropopause frequencies in radiosondes and modern reanalyses, focusing on profiles where multiple WMO tropopauses are identified at 20 km and below (to isolate multiple tropopauses indicative of STE between the trop- ical UT and ExLS). For these studies, the WMO definition is used, wherein additional tropopauses (*i.e.*, secondary and above) are identified using the same criteria as that for the first tropopause if the lapse-rate exceeds 3 Kkm^{-1} in a layer at least 1 km deep above a previous identification. *Xian and Homeyer* (2019) find good agreement for global patterns of double tropopause events between the observations and reanalyses, but an under-representation of the frequency of events. **Figure 7.10** shows trends in monthly double tropopause frequency in radiosondes and reanalyses over the period from 1981 to 2015 and reveals that double tropopause events are increasing globally throughout the subtropics. CFSR/CFSv2 is the only reanalysis that is broadly inconsistent with the observations and differs considerably from the remaining reanalyses. Tropopause break-relative analysis of double tropopause trends (not shown here) demonstrates that increases in double tropopause frequency are largely poleward of instantaneous tropopause break locations in the reanalyses (*i.e.*, in the extratropics).

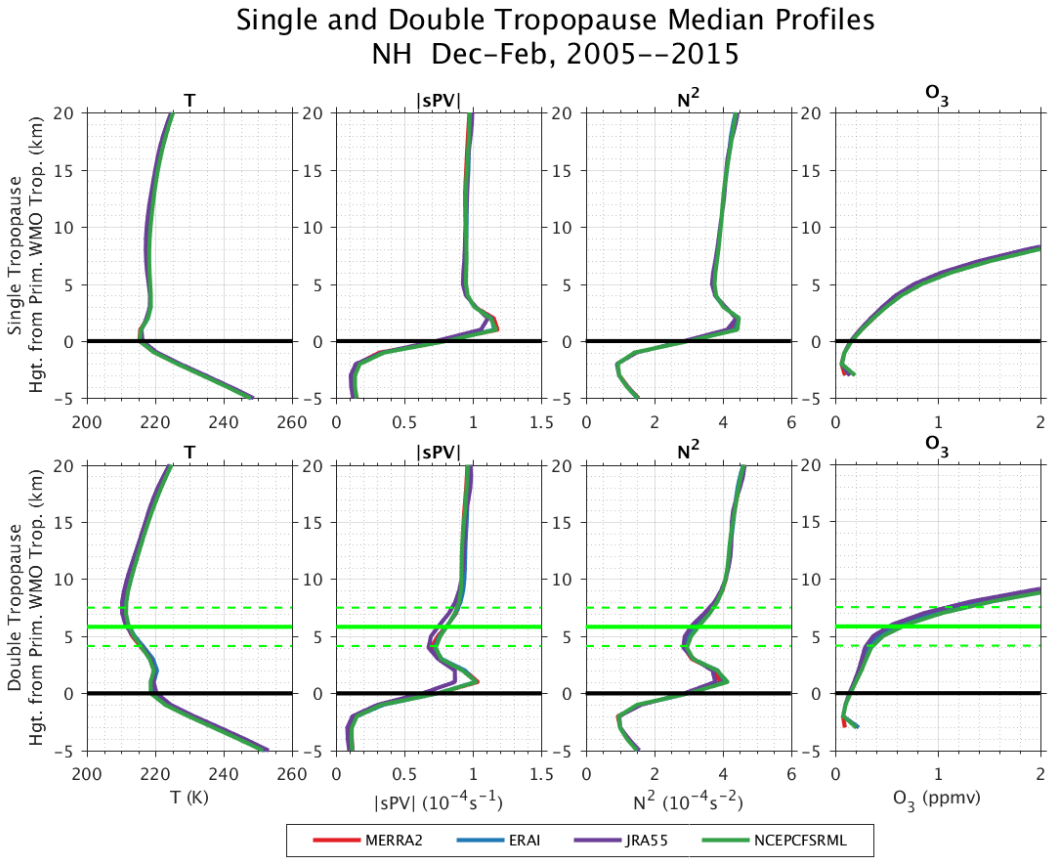

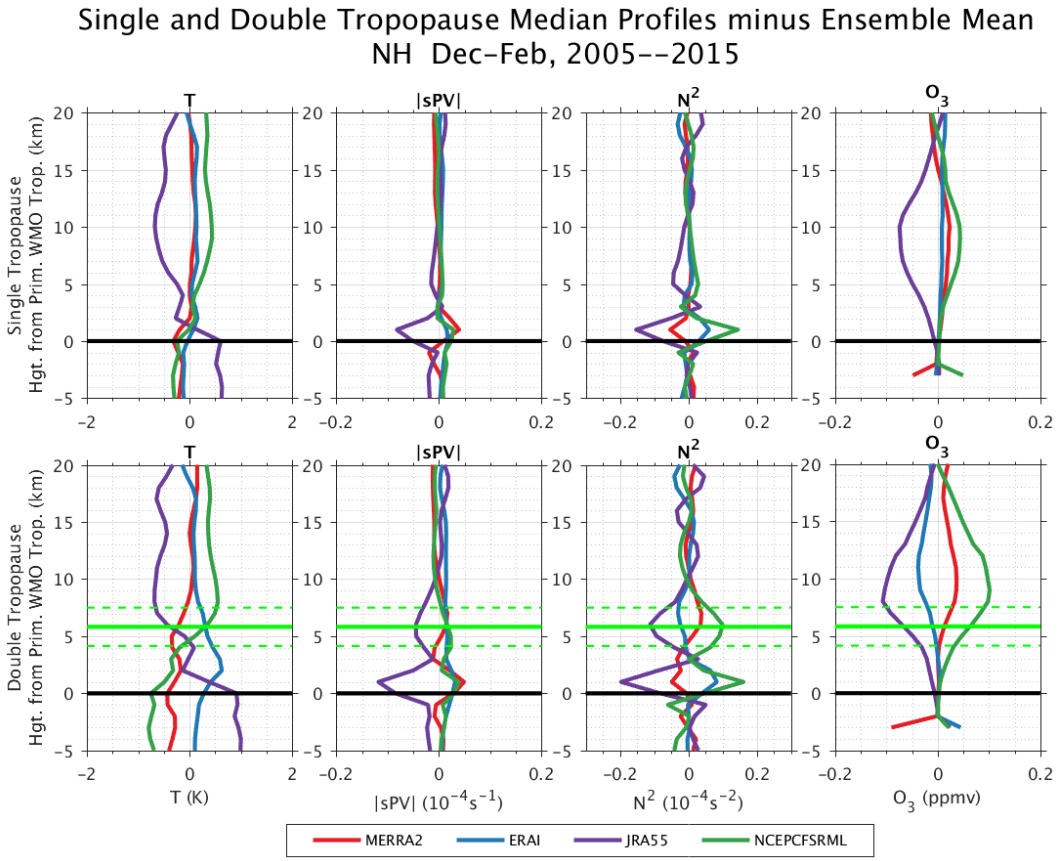

Figure 7.8: *(Top) Climatological (left to right) temperature, sPV, N^2, and MLS ozone distributions from MERRA-2, ERA-Interim, JRA-55, and CFSR/CFSv2 in regions with and without multiple lapse rate tropopauses, for the NH in DJF in 2005 through 2015. All fields are interpolated to the MLS measurement locations before averaging. (Bottom) Differences of those profiles from the REM of the four reanalyses. The ozone shown is from MLS in all cases – the differences thus arise solely from the identification of different profiles as having single and double tropopauses.*

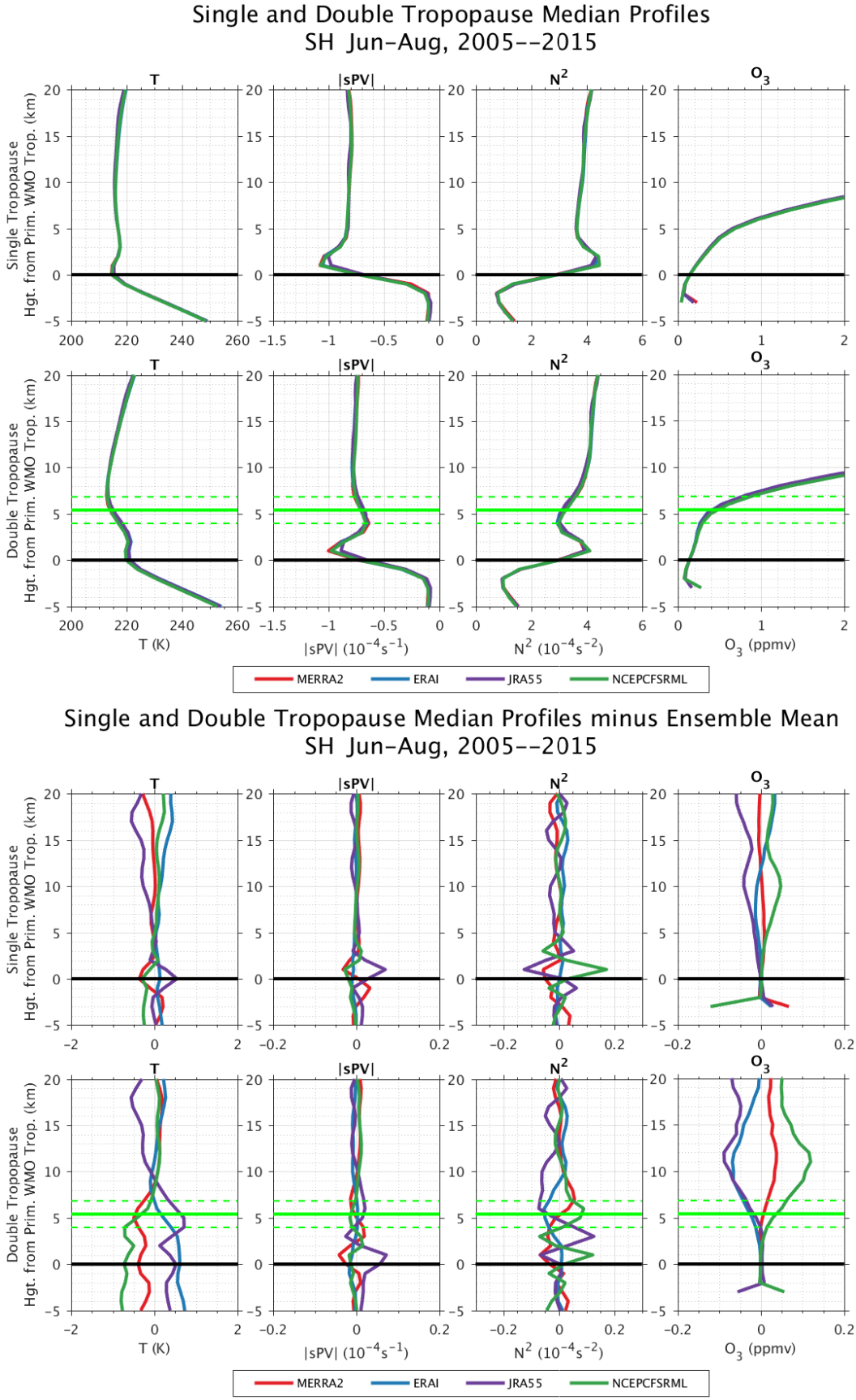

Figure 7.9: *As in* ***Figure 7.8*** *but for the SH in JJA.*

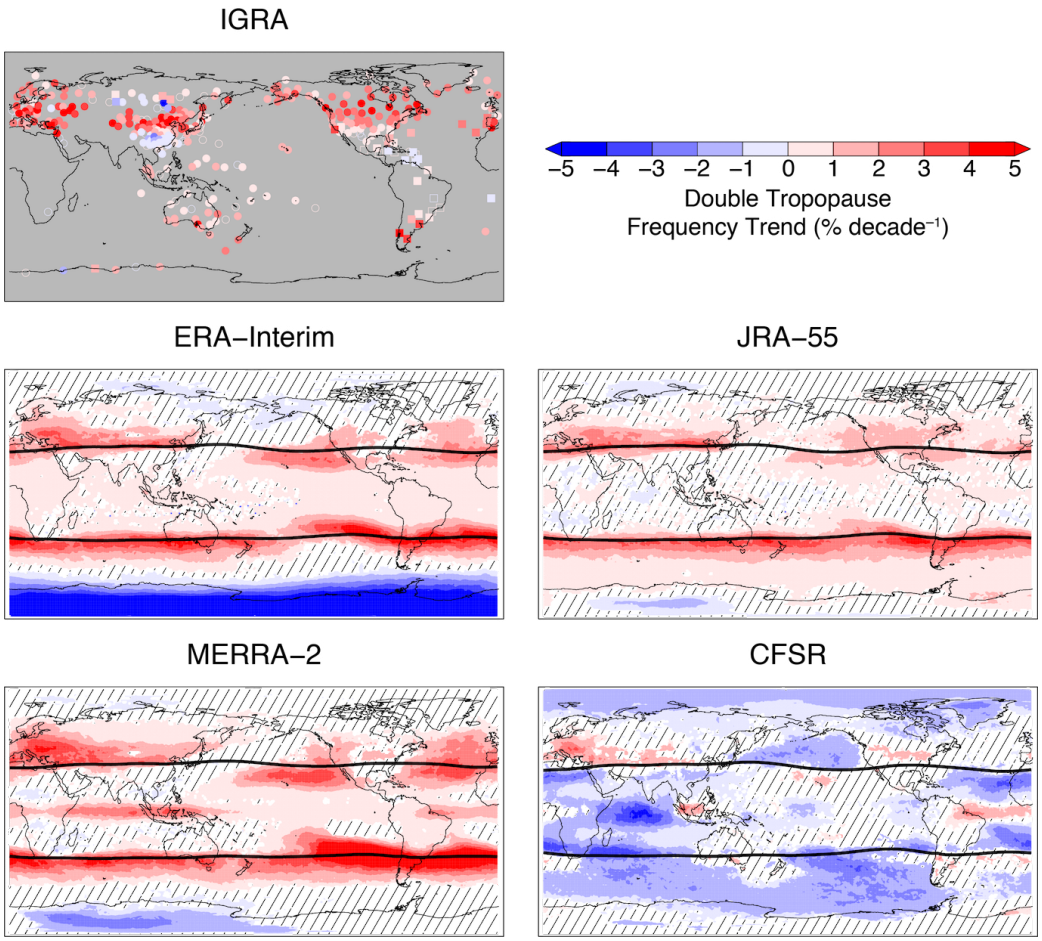

Figure 7.10: ***Figure 7*** *from Xian and Homeyer (2019). Maps of 35-yr (1981 - 2015) trends in the WMO lapse-rate tropopause double tropopause frequency from global radiosonde observations and four modern reanalyses: ERA-Interim, JRA-55, MERRA-2, and CFSR/CFSv2. Color-filled regions are statistically significant at the 99% level. Thick black lines show the annual-mean tropopause break latitudes for each reanalysis.*

While changes in double tropopause frequency over this time period may be related to changes in the Hadley cell circulations (see *Chapter 8*), the relationship between the two has not been thoroughly investigated.

7.4 Jet Streams

7.4.1 Jet Characterization for UTLS Studies

The upper tropospheric (UT) jet streams are a key component of the atmospheric circulation and closely linked with weather and climate phenomena such as storm tracks, precipitation, and extreme events (*Mann et al.*, 2017; *Harnik et al.*, 2016; *Koch et al.*, 2006, and references therein). The UT jets and the tropopause are themselves sensitive to climate change and ozone depletion (*Waugh et al.*, 2015; *Grise et al.*, 2013; *McLandress et al.*, 2011; *WMO*, 2011; *Lorenz and DeWeaver,* 2007, and references therein), as well as to natural modes of variability such as ENSO and QBO (*Olsen et al.*, 2016; *Lin et al.*, 2014, 2015; *Hudson*, 2012, and references therein). The upper tropospheric jets (as well as the tropopauses) are important drivers of composition variability in the UTLS, acting as transport barriers and controlling STE and long-range transport. Assessing UTLS composition and its relationships to the dynamics of the tropopauses and UTLS jets is an important outstanding problem (*e.g.*, *Hegglin et al.*, 2016). As noted by *Manney and Hegglin* (2018a), many of the critical characteristics of jets cannot be directly observed, so reanalyses are one of our most important tools for understanding UTLS jets and their impact on composition. In the following sections we use JETPAC to characterize and compare UTLS jets in the most recent suite of reanalyses. The jet characterization from JETPAC is as described by *Manney et al.* (2011, 2014, 2017) and *Manney and Hegglin* (2018a); briefly:

A UT jet is identified wherever there is a wind speed maximum greater than 40 m s^{-1}; the boundaries of the jet region are the points surrounding that (in both horizontal and vertical directions) where the wind speed drops below 30 m s^{-1}. When more than one maximum above 40 m s^{-1} appears within a given 30 m s^{-1} contour, they are defined as separate cores if the latitude distance between them is greater than 15 degrees or the decrease in wind speed between them is greater than 25 m s^{-1}. These parameters were tuned to approximate as closely as feasible the choices that would be made by visual inspection.

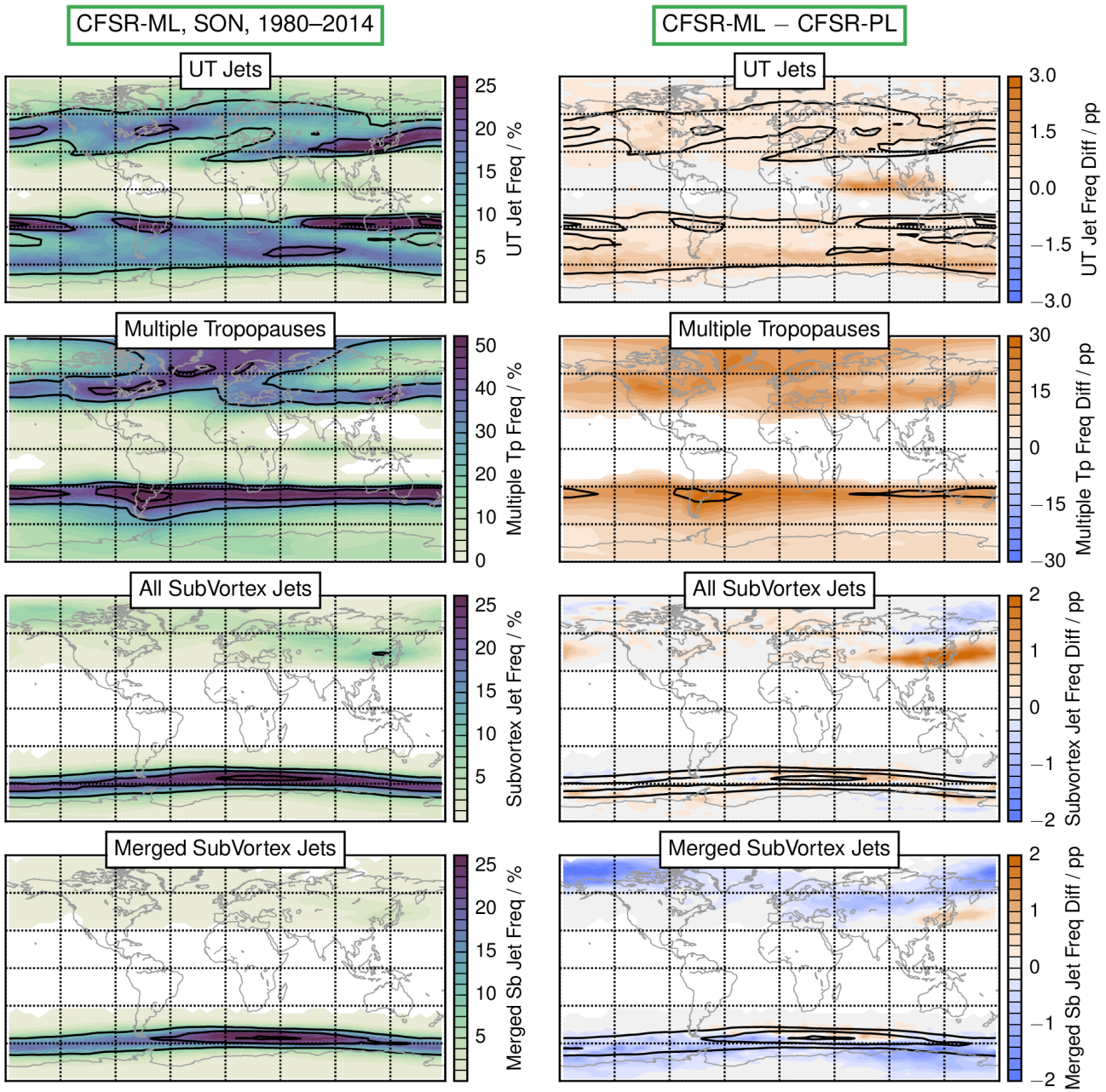

Figure 7.11: *Comparison of CFSR/CFSv2 on (left) model levels and pressure levels, showing climatological (1980 - 2014) SON frequency distributions of (top to bottom) upper tropospheric jets, multiple tropopauses, all subvortex jets, and merged subvortex jets. The difference between model and pressure levels is shown in the right column. Black overlays show frequency contours (10, 20, and 30 % on jet plots; 30, 45, and 60 % on multiple tropopause plots). (From Manney et al., 2017).*

The UT jets may be further characterized as "subtropical" (STJ; thought of as primarily radiatively driven) or "polar" (PJ; also referred to as "eddy-driven") (see *Manney et al.*, 2014, and references therein, for detailed discussion of the spectrum of jet characteristics). *Manney et al.* (2011, 2014) used a simple latitude criterion (appropriate for climatological studies) to identify STJ and PJ. A more robust definition is needed for regional and case studies. We follow *Manney and Hegglin* (2018a) here, and define the STJ as the most equatorward westerly jet for which the WMO tropopause altitude at the equatorward edge of the jet is greater than 13.0 km and that tropopause altitude drops by at least 2.0 km from the equatorward to the poleward side of the jet. This definition identifies the jet across which the "tropopause break" occurs. The PJ is then defined as the strongest jet poleward of the STJ, or poleward of 40 degrees latitude if no STJ was identified.

The subvortex jet core is identified at each reanalysis model level as the most poleward maximum in westerly wind speed that exceeds 30 m s^{-1}, and the locations of the 30 m s^{-1} contour crossings poleward and equatorward of this define the boundaries of the subvortex jet region. The bottom of the subvortex jet often extends down to the level of the tops of the upper tropospheric jets. To distinguish between the two in such cases, we first identify the subvortex jet at levels down to a pressure near 300 hPa.

We then work down from the level nearest 80 hPa to identify the lowest altitude at which the wind speed of the jet is still decreasing with decreasing altitude; this is defined as the bottom of the subvortex jet. Those cases where the subvortex jet joins with the top of a UT jet are referred to as "merged" jets here.

The tropopause definitions in JETPAC were discussed in *Section 7.3*.

7.4.2 Climatology of UTLS Jets in Reanalyses

Manney et al. (2017) described a comprehensive comparison of UTLS jets and multiple tropopauses. An important aspect of this study was to assess differences between alternate products from individual reanalysis systems. Of particular note is a comparison of CFSR/CVSv2 data on model and pressure levels that highlights the importance of vertical grid spacing for both tropopause and UTLS jet characteristics (*e.g.*, **Figure 7.11** shows such a comparison for SON; other seasons show generally similar differences, albeit somewhat smaller in the equinox seasons). The pressure level data substantially underestimate upper tropospheric jet and multiple tropopause frequencies primarily because of the coarser spacing of the levels, while they overestimate merged jet frequencies for the same reason (because relatively shallow layers where neither upper tropospheric nor subvortex jets exist are missed).

Figure 7.12 shows differences in the climatological (1980 through 2014) zonally averaged annual cycle of upper tropospheric jets frequencies, with other reanalyses compared to MERRA-2; see *Manney et al.* (2017) for a discussion of significant regional differences among the reanalyses. Generally good qualitative agreement is seen among the reanalyses for large-scale climatological features in UTLS jet distributions, but quantitative differences are sufficient that they could have significant consequences for transport and variability studies. Most of the differences in distributions of UTLS jets were found to be consistent with differences in assimilation model grids and resolution - for example, ERA-Interim (with coarsest native horizontal resolution) typically shows a significant low bias in upper tropospheric jet frequencies with respect to MERRA-2, and JRA-55 a more modest one, while CFSR/CFSv2 (with finest native horizontal resolution) shows a high bias with respect to MERRA-2. Agreement between the subvortex jets characterized using model-level data was also generally good, with ERA-Interim showing slightly higher and JRA-55 slightly lower maximum subvortex jet frequencies than MERRA-2 in NH winter (see *Manney et al.*, 2017). Because the subvortex jets are identified on individual levels, whether a reanalysis shows higher or lower frequencies is dependent on a complex interplay of horizontal resolution, vertical resolution, and vertical grid level locations, as well as potentially other model differences.

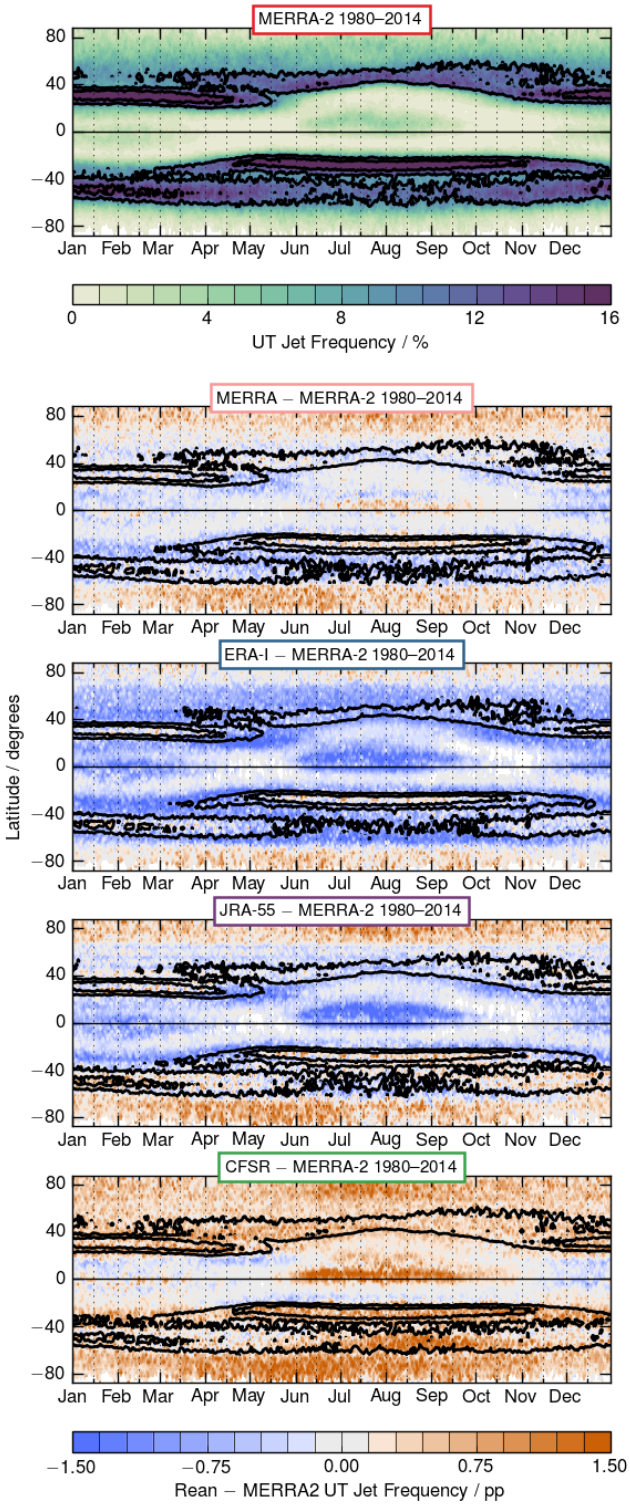

Figure 7.12: *Climatological (1980 - 2014) annual cycle of zonally averaged frequency distributions of upper tropospheric jets from MERRA-2 (top), and differences between those frequency distributions and the other reanalyses (remaining rows). Black overlays show frequency contours of 10 % and 15 %, from the corresponding reanalysis in each panel. (Adapted from Manney et al., 2017).*

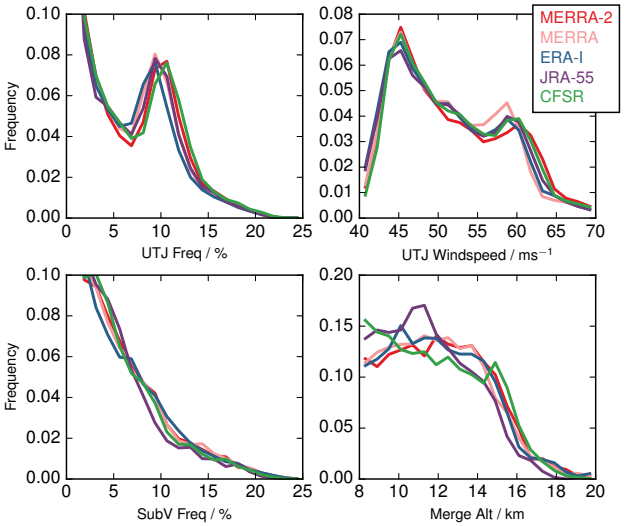

Figure 7.13: *Climatological frequency distributions of subvortex jets in NH winter from MERRA-2 (top), and differences between those frequency distributions and the other reanalyses (remaining rows). (Adapted from Manney et al., 2017).*

Figure 7.13 shows a top level summary of UT jet frequencies and windspeeds, and subvortex jet frequencies and merge altitudes. When averaged globally and seasonally, UT jets show very good agreement among the reanalyses in frequency and windspeed. The subvortex jet frequencies also show very good agreement, but with slightly larger differences in the altitude at which subvortex and UT jets merge. As noted above and by *Manney et al.* (2017), the merge altitude is very sensitive not only to the vertical resolution, but also to the specific altitudes of the model levels.

7.4.3 Trends in UTLS Jets in Reanalyses

Manney and Hegglin (2018a) (see *Manney and Hegglin*, 2018b, for figure labeling corrections) examined variability and trends in UT jets by using the JETPAC fields to calculate the monthly and seasonal mean latitude, altitude, and wind speed of the jets, both averaged over all longitudes and by longitude region. Trends in STJ latitude are used as a measure of tropical width, and the results for this diagnostic, as well as other jet and tropopause based diagnostics are discussed in *Chapter 8* of this report.

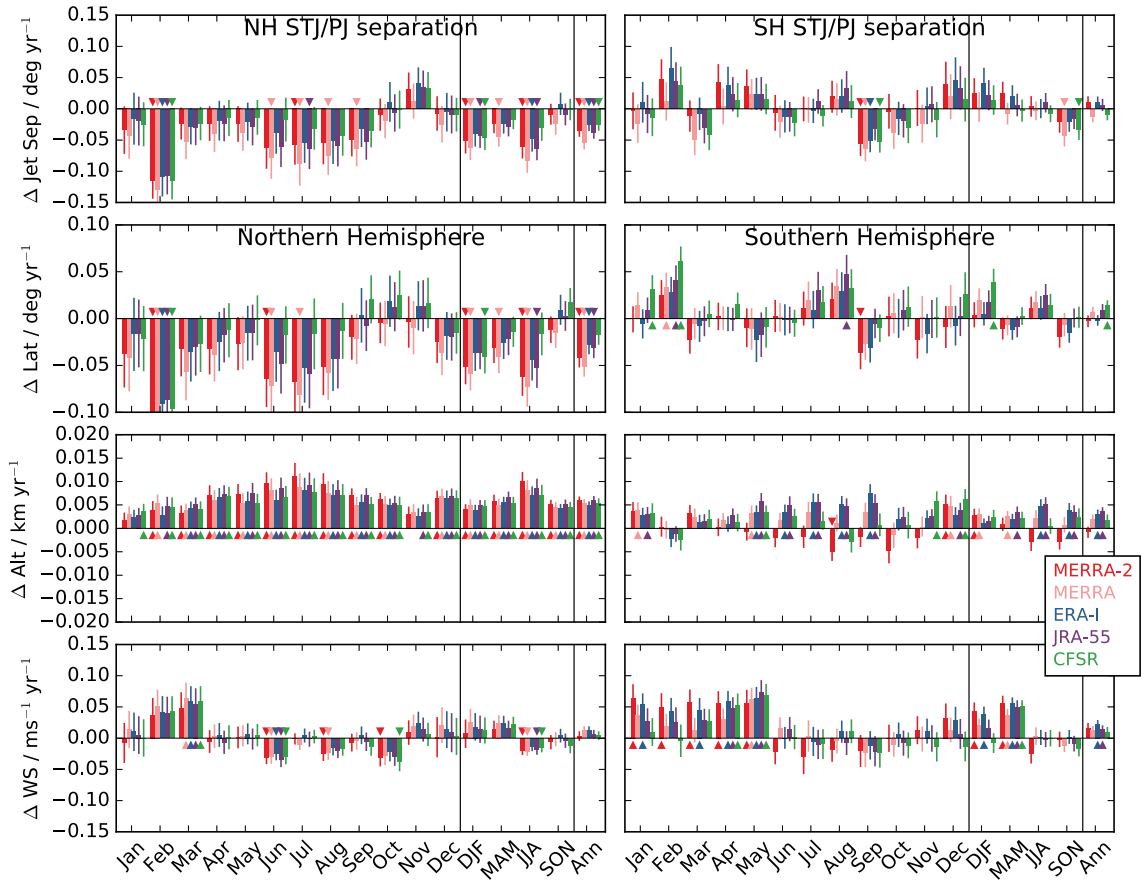

Figure 7.14: *Bar charts of zonally averaged NH and SH polar jet and polar/subtropical jet separation trends as a function month and season, showing five reanalyses. The bars show the slopes of the fits, and the error bars (centered about the top of the bars) show the 1-σ uncertainty in that slope. Note that the absolute value of latitude is used, so positive slopes (bars extending upward from the zero line) indicate a poleward shift in both hemispheres. The zero line in each case indicates no trend in the quantity shown. Triangles indicate cases where a permutation analysis (see Manney and Hegglin, 2018a) shows the slope to be significant at the 95 % confidence level. (From Manney and Hegglin, 2018a). © 2018 American Meteorological Society, used with permission.*

Figure 7.14 shows monthly, seasonal, and annual zonally averaged trends in PJs from five reanalyses, and **Figure 7.15** shows PJ trends as a function of longitude for DJF. For the most part, the NH polar jet shows a relatively robust equatorward and upward shift, with good consistency among the reanalyses. However, there are some times (*e.g.*, October to November in the zonal mean) and regions (*e.g.*, over the north Atlantic in DJF) that show poleward shifts or inconsistent shifts. Zonal mean trends are less consistent among reanalyses in the SH, and smaller in the zonal mean; however, a robust poleward shift of the SH PJ is seen in DJF (*Manney and Hegglin*, 2018a) except in the eastern to central Pacific. In general, the trends vary strongly with both longitude and season (see *Manney and Hegglin*, 2018a, for a detailed summary of all regional and seasonal trends and their significance), and in many cases the trends are not robust, either because they are not statistically significant or because they do not agree among all the reanalyses. As discussed in detail in *Chapter 8*, there are only a few regions / seasons with robust tropical widening, and also some with robust tropical narrowing. Agreement among the reanalyses in the trend direction is a necessary (but not sufficient) condition to consider a trend robust. *Manney and Hegglin* (2018a) found several cases where one or more reanalyses showed a statistically significant trend that was opposite in sign to that from other reanalyses. In particular, there are several cases in the SH when either MERRA-2 or CFSR/CFSv2 shows opposite behavior to the other reanalyses (*e.g.*, **Figure 7.15**, lower right panel).

Although some of the reanalyses do show better or worse agreement in assessment of trends, because the attribution of trends in reanalyses can be so strongly dependent on possible changes in the input data, we recommend extreme caution in attempting to evaluate trends from reanalysis data. However, because many diagnostics (such as jet core locations) cannot be obtained from observational data, consistency among the reanalyses is an important condition for concluding that an apparent trend *may* be robust. Furthermore, given the sensitivity to horizontal and vertical resolution of jet characteristics demonstrated in *Section 7.4.2*, and large regional and seasonal variability, it is recommended that trend studies should use data on the model grids when possible and account for regional and seasonal variability.

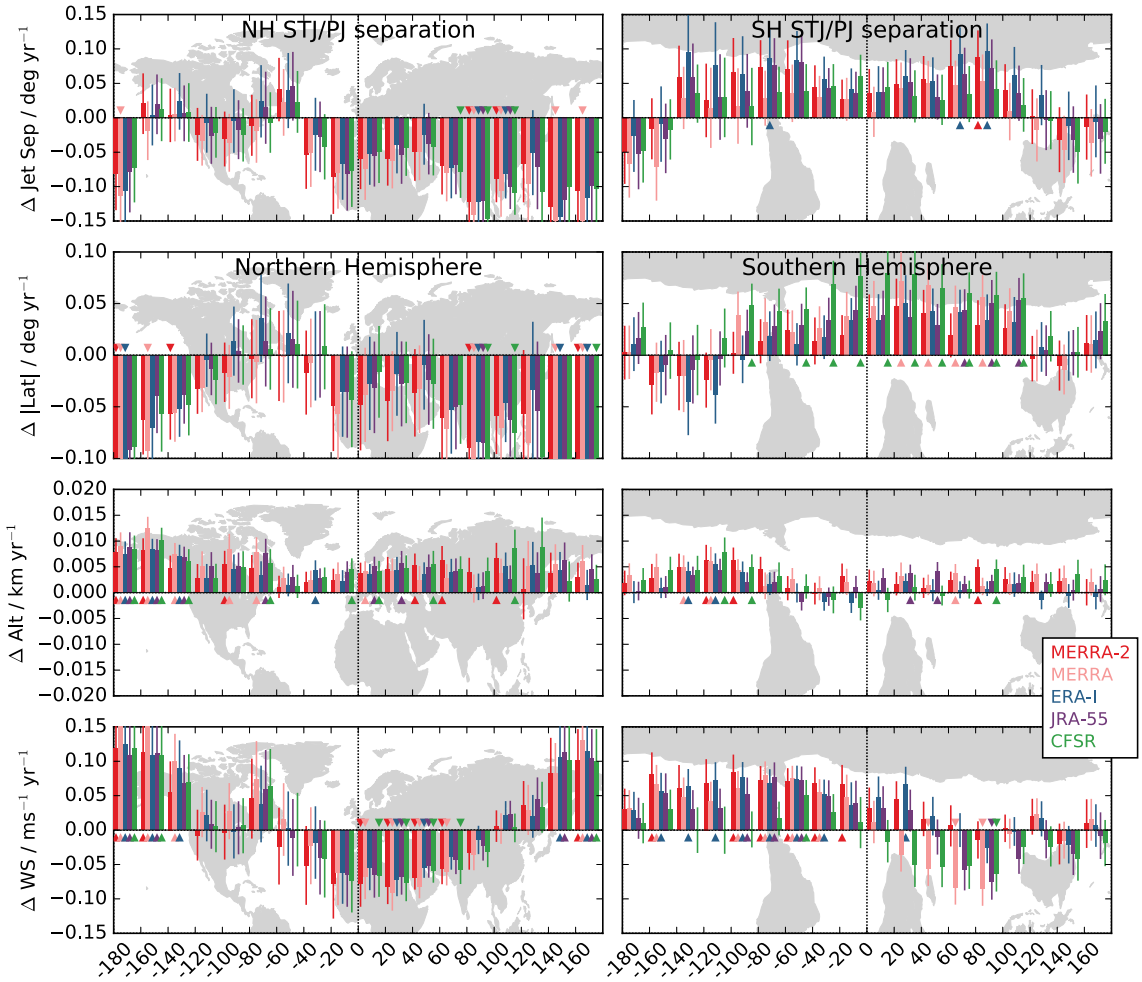

Figure 7.15: *Bar charts of global polar jet and polar/subtropical jet separation trends as a function of longitude in 20 -degree bins, showing five reanalyses for DJF. Layout is as in* ***Fig. 7.14****. (From Manney and Hegglin, 2018a). © 2018 American Meteorological Society, used with permission.*

7.5 Transport and Mixing

Transport and mixing in the ExUTLS has important impacts on the chemical and radiative characteristics of this layer. In particular, transport that involves exchanges of air across the tropopause (STE) most often leads to the greatest impacts. As discussed in the Introduction, only large-scale transport processes are resolved in reanalyses, so diagnostics used to compare transport and mixing are limited to such scales here.

7.5.1 Stratosphere-Troposphere Exchange

STE is commonly examined using trajectory-based (*i.e.*, Lagrangian) methods. Such trajectories are driven by horizontal winds and either kinematic vertical velocity (*i.e.*, omega) or diabatic heating rates for the vertical component. Trajectory paths are compared to a representation of the tropopause (commonly an iso-surface of PV, but alternatively the lapse-rate tropopause) and those that cross this surface are identified as either troposphere-to-stratosphere transport (TST) or stratosphere-to-troposphere transport (STT). Eulerian methods to calculate STE provide a complimentary bulk transport diagnosis and may differ considerably from Lagrangian methods.

Operational forecast model analyses and reanalyses have been used for STE studies over the past few decades (*e.g.*, *Škerlak et al.*, 2014; *Sprenger and Wernli*, 2003; *Seo and Bowman*, 2002; *Wernli and Bourqui*, 2002; *Stohl*, 2001; *Appenzeller et al.*, 1996). Some studies have been regional, focused on single transport processes, or limited to short time periods (*i.e.*, a few years or less). Others have evaluated global transport over longer time periods. Despite the common use of trajectories in these studies, differences in trajectory integration times, conditions applied to categorize an individual particle's path as irreversible exchange, and the input wind fields have led to significant differences in estimates of STE.

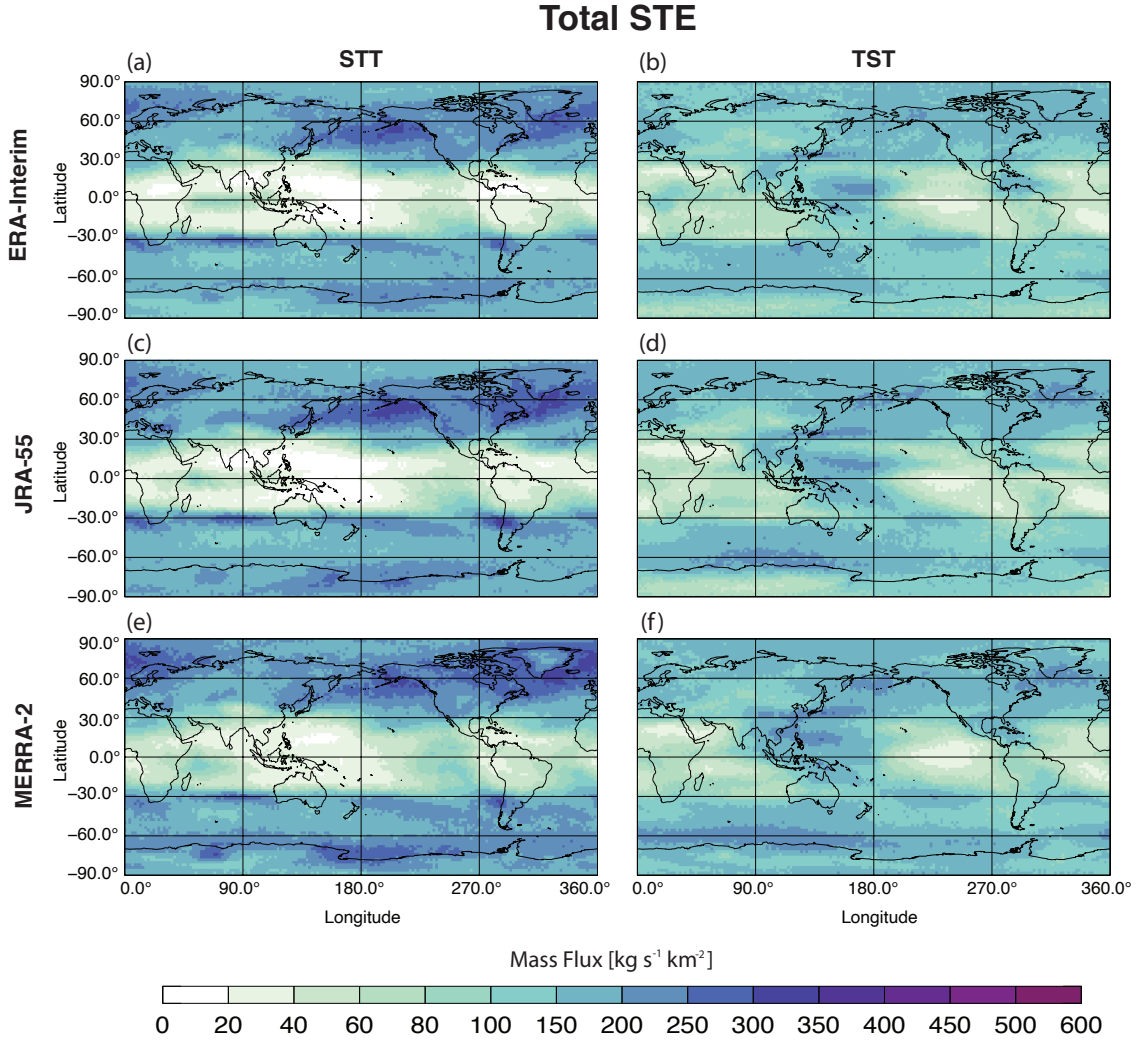

Figure 7.16: *A modified version of Figure 4 from Boothe and Homeyer (2017): global distributions of annual-mean (left) STT and (right) TST from (top-to-bottom) ERA-Interim, JRA-55, and MERRA-2. These STE estimates were calculated using a trajectory model. This figure is modified from that in Boothe and Homeyer (2017) by excluding results for MERRA and revising the analysis to use ASM wind fields for MERRA-2 (instead of the ANA fields used in the original).*

Few studies have conducted STE calculations using multiple wind fields (*e.g.*, those from more than one reanalysis).

Boothe and Homeyer (2017) conducted trajectory calculations driven by the 3D wind fields of four modern reanalyses (ERA-Interim, JRA-55, MERRA, and MERRA-2) over a 15-year period (1996 - 2010) to determine global STE. In particular, forward and backward trajectories were computed each day for a global 3D lapse-rate tropopause-relative grid of particles, each having constant mass. Trajectories that crossed the tropopause during 1 day downstream and remained in their destination reservoir (*i.e.*, stratosphere for TST, troposphere for STT) for at least 4 out of 5 days downstream were flagged as likely irreversible transport. These particles were also required to have been in their parent reservoir (*i.e.*, troposphere for TST, stratosphere for STT) for at least 4 out of 5 days upstream to be kept for STE analyses. For complete details on the trajectory model used and STE identification methods, the reader is referred to *Boothe and Homeyer* (2017).

Findings from *Boothe and Homeyer* (2017) include important differences in the magnitudes, geographic locations, annual cycles, and long-term changes and variability of STE between the reanalyses. The authors separate STE into three regions (tropics, subtropics, and extratropics) and two directions (TST and STT) to further evaluate the similarities and differences in STE among the reanalyses. **Figure 7.16** shows comparisons of the geographic distributions of annual mean TST and STT from three of the four reanalyses (modified from *Boothe and Homeyer,* 2017). These distributions highlight some of the important differences found in the locations of TST and STT maxima, especially in the tropics. Despite these differences, *Boothe and Homeyer* (2017) show that the annual cycles of TST and STT are similar among the reanalyses and that differences in the amounts of TST, STT, and net STE (TST-STT) occur primarily in the extratropics.

Analysis of the long-term variability of TST and STT was also found in *Boothe and Homeyer* (2017) to differ considerably among the reanalyses. In particular, for ERA-Interim and JRA-55, TST was found to increase in the tropics and STT was found to increase in the extratropics during the 15-year study period, while MERRA and MERRA-2 showed the opposite behavior. MERRA also showed large increases in TST in the extratropics, while the remaining analyses showed little change in this component of STE. **Figure 7.17** shows these results from *Boothe and Homeyer* (2017).

While the objective of *Boothe and Homeyer* (2017) was to compare STE in the reanalyses, questions remain on the source of the differences found. The authors did show that differences in STE amounts are accompanied by consistent differences in the frequency of exchange events. The authors also hypothesize that differences in the dynamics (both horizontal and vertical motion), tropopause altitudes, assimilated datasets, and model grids may contribute to the observed differences in STE. Evidence for systematic differences in vertical motion and tropopause altitude was given in *Boothe and Homeyer* (2017) and also in **Figures 7.1** and **7.2** of this report.

One caveat of the *Boothe and Homeyer* (2017) study is that the MERRA and MERRA-2 wind fields used were not those recommended for transport studies by the NASA team. Guidelines were released after the *Boothe and Homeyer* (2017) study to specify that ASM fields should be used instead of ANA fields. Thus, an update to the *Boothe and Homeyer* (2017) analysis was completed to determine differences in transport calculated using 3D winds from these two products. **Figure 7.18** compares geographic distributions of global mean STT and TST from the MERRA-2 ANA and ASM analyses. While some slight differences in patterns are observed, the biggest change in STE results from using ASM fields instead of ANA is that STT increases and TST decreases, leading MERRA-2 transport patterns and magnitudes to be more similar to ERA-Interim and JRA-55. Time series analyses shown in *Boothe and Homeyer* (2017) was also revisited, but no significant changes in the results were found (*i.e.*, long-term variability and changes are consistent in the ANA and ASM analyses; not shown).

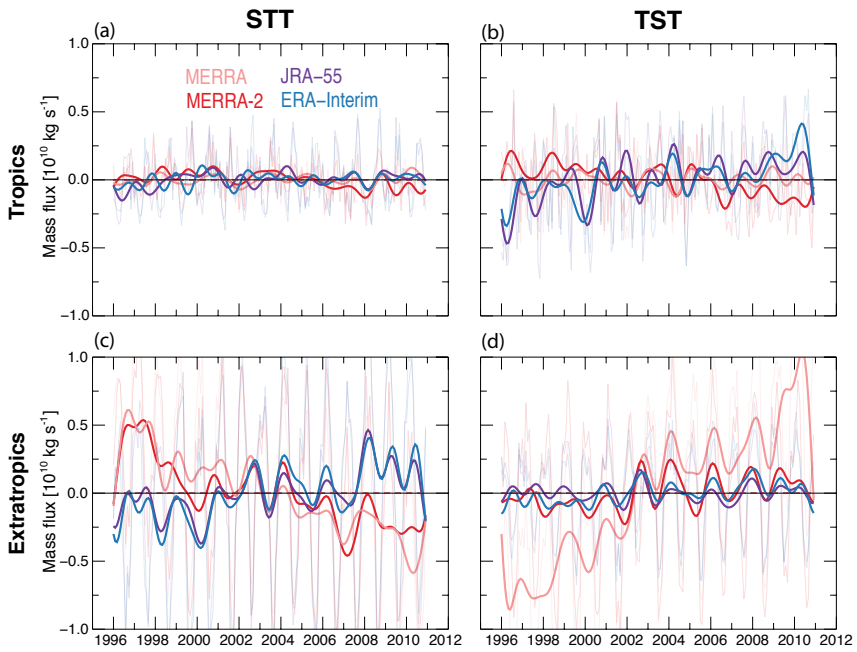

Figure 7.17: *Figure 14 from Boothe and Homeyer (2017): 15-year timeseries of long-term mean relative (left) STT and (right) TST in the (top) tropics and (bottom) extratropics in ERA-Interim, JRA-55, MERRA-2, and MERRA. These STE estimates were calculated using a trajectory model.*

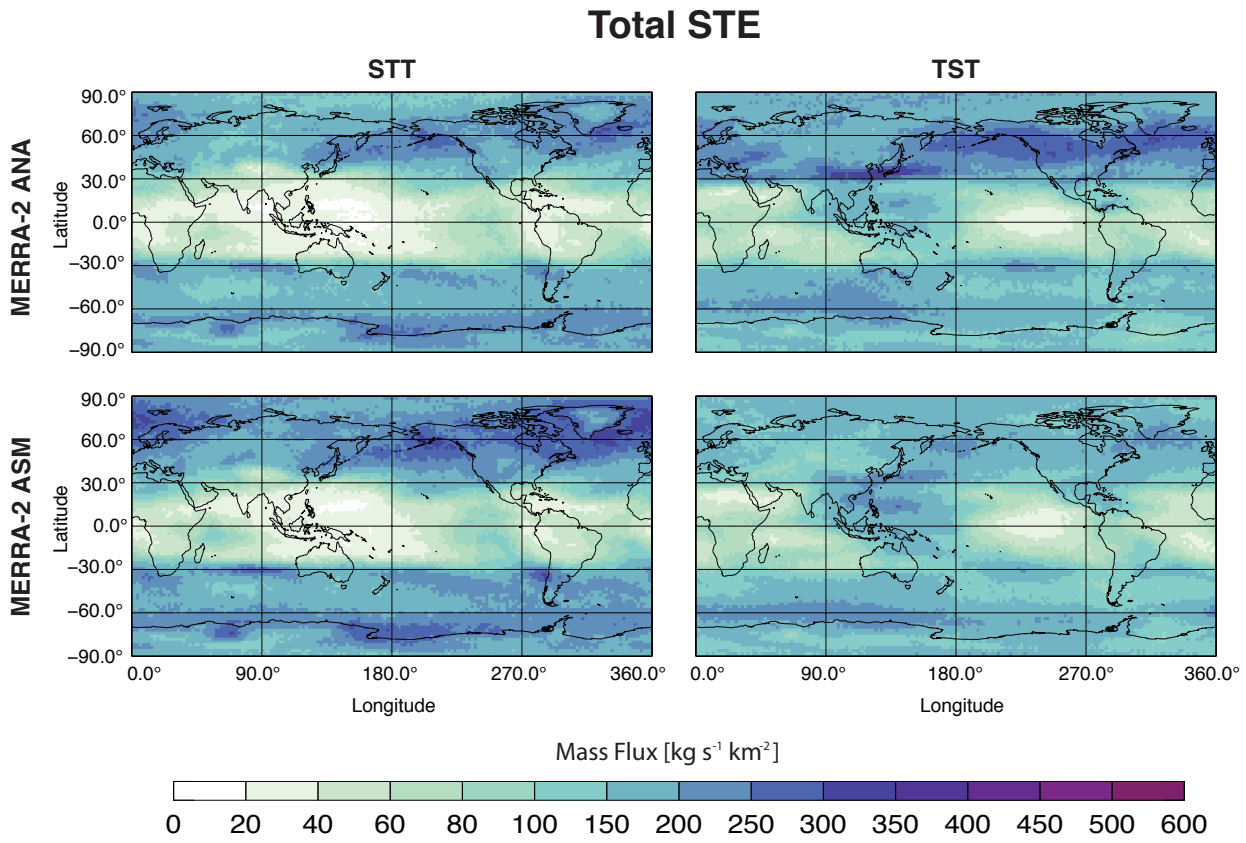

Figure 7.18: *An comparison of (top) MERRA-2 ANA panels from Figure 4 of Boothe and Homeyer (2017) and (bottom) the revised MERRA-2 ASM analysis. Global distributions of annual-mean (left) STT and (right) TST. These STE estimates were calculated using a trajectory model.*

7.5.2 Mixing and Transport Barriers

PV-based diagnostics in equivalent latitude (EqL) coordinates can provide information on mixing and transport barriers. In particular, PV gradients indicate the strength of transport barriers such as the stratosphere polar vortex or the tropopause (*e.g.*, *Manney and Lawrence*, 2016; *Kunz et al.*, 2011a; *Mahlman*, 1997; *McIntyre and Palmer*, 1983, and references therein). Effective Diffusivity (K_{eff}) is also commonly used to assess the location and strength of mixing and transport barriers in stratospheric and UTLS studies (*e.g.*, *Abalos et al.*, 2016; *Allen and Nakamura*, 2001, 2003; *Haynes and Shuckburgh*, 2000a,b, and references therein). Here we show comparisons of PV gradients and K_{eff} as a function of equivalent latitude and time for 2005 through 2015 to assess potential differences in the representation of mixing and transport barriers in reanalyses. For this analysis, K_{eff} is calculated directly from the PV fields (as described by, *e.g.*, *Santee et al.*, 2011; *Manney et al.*, 2009, and references therein), with PV used on the native model levels, as described by *Lawrence et al.* (2018). As noted by *Lawrence et al.* (2018), some caution is required in using PV fields from different reanalyses as they are derived from the reanalysis fields provided in different ways. The calculation of PV gradients and (especially) K_{eff}, depends on horizontal resolution. To the extent that overall biases represent the ability of the reanalyses to resolve small-scale mixing processes, they may represent reanalysis differences that are meaningful to evaluating their use in transport studies. However, scaling K_{eff} (which is typically used as a qualitative measure of mixing and transport barriers) to a similar range allows more quantitative comparison of the locations, times, and relative strength of mixing regions and transport barriers. We thus scale K_{eff} by subtracting the global climatology for 2005 - 2015 for each reanalysis from the daily values and dividing by the standard deviation of that climatological mean. The time period 2005 through 2015 was chosen to facilitate comparisons of EqL/time series of assimilated and MLS ozone (see *Section 7.6* below).

Figures 7.19 and **7.20** show climatological sPV gradients as a function of EqL on the 350 K and 390 K isentropic surfaces, respectively. Plots of sPV in the same format (not shown; also see *Millán et al.*, 2021) indicate that, while biases exist between the reanalyses' sPV fields in the UTLS, they are typically less than about 10 % except near the equator (where sPV values themselves are very low). The sPV gradients at 350 K are largely tropospheric in character, with strongest gradients along the UT subtropical jets, whereas the sPV gradients at 390 K are largely stratospheric, with strongest gradients along the polar vortex edges in winter.

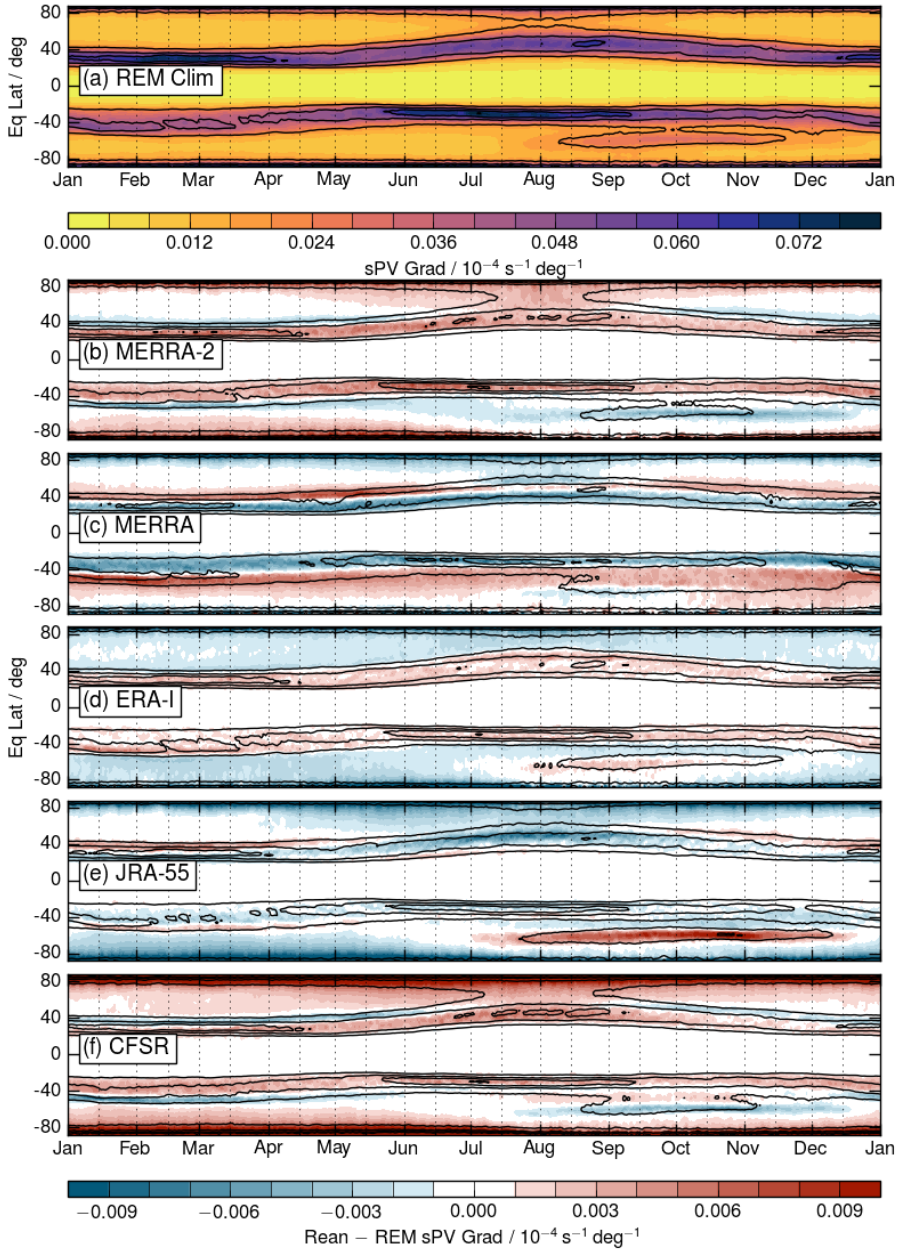

Figure 7.19: *Climatological (2005 - 2015) annual time series of (Top) sPV gradients at 350 K as a function of equivalent latitude from a reanalysis ensemble mean (REM, including MERRA-2, MERRA, ERA-Interim, JRA-55, and CFSR/CFSv2 reanalyses), and (following rows) the difference of each reanalysis from the REM. The black overlays show the same selected contours, from the REM on the top panel, and each of the reanalyses on the following panels.*

In the SH, enhanced gradients near 60 °S demark the lowest extension of the subvortex. At 390 K, the top of the subtropical jet is apparent in each hemisphere (more clearly in the NH) as enhanced sPV gradients near 30 latitude from about November through May in the NH and May through August in the SH, times with the strongest sPV gradients along the UT subtropical jet at lower levels.

The differences among reanalysis sPV gradients are generally modest, on the order of 10 % (much larger differences at the highest EqLs are likely due to noise in the sPV fields there and are not physically meaningful). The differences at 350 K along the NH subtropical jet tend to have a dipole structure in latitude, suggesting small differences in the location of the strongest sPV gradients; the patterns of biases with respect to the jets appear to be largely consistent throughout the annual cycle. MERRA-2 and (especially) CFSR/CFSv2 350 K sPV gradients are generally stronger than those in the REM, while those in the other reanalyses tend to be weaker, which may be related to the higher horizontal resolution of those reanalyses.

Differences in sPV gradients among the reanalyses at 390 K are still generally modest, and are largest at the locations of the winter stratospheric subvortex jet.

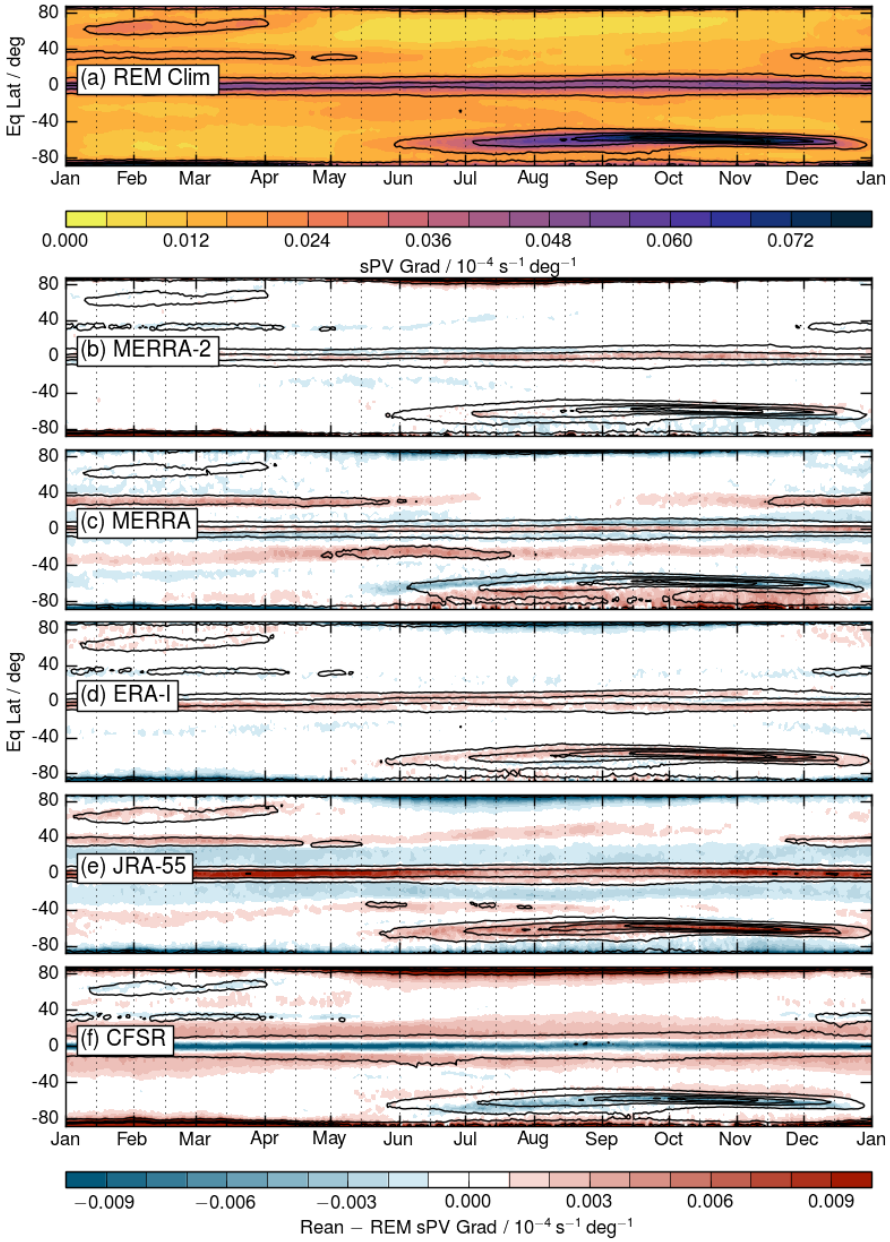

Figure 7.20: *As in* ***Fig. 7.19*** *but at 390 K.*

Near the SH subvortex jet, ERAI and JRA-55 show stronger gradients and CFSR/CFSv2 weaker gradients than the REM, while MERRA-2 gradients are close to the REM and MERRA shows a dipole pattern suggestive of a slightly more poleward transport barrier. A similar pattern is seen near the NH subvortex jet, but the differences are much smaller.

The patterns of climatological K_{eff} (**Figures 7.21** and **7.22**) are consistent with those in the sPV gradients, with low/high values of K_{eff} in regions of high/low sPV gradients. Strong mixing regions are seen at 390 K during and following the breakup of the stratospheric vortices in the LMS (May through October in the NH, November through April in the SH). At 350 K, the transport barriers align with the UT subtropical jets, with relatively strong mixing away from those regions, except from about August through October in the SH when the subvortex jet presents a significant transport barrier.

At 350 K, MERRA, JRA-55, and ERA-Interim tend to have higher values in the strong mixing regions poleward of the subtropical jets, suggesting more mixing. MERRA-2 and CFSR/CFSv2 show higher values at low latitudes, suggesting more mixing in the tropics. At 390 K, the reanalyses show large differences in the transport barrier at the edge of the SH subvortex jet, with MERRA and ERA-Interim showing higher values and MERRA-2 and CFSR/CFSv2 lower values than the REM. While quantitative differences at all UTLS levels in K_{eff} are relatively large, the qualitative seasonal patterns of mixing and transport barriers are captured well in all of the reanalyses.

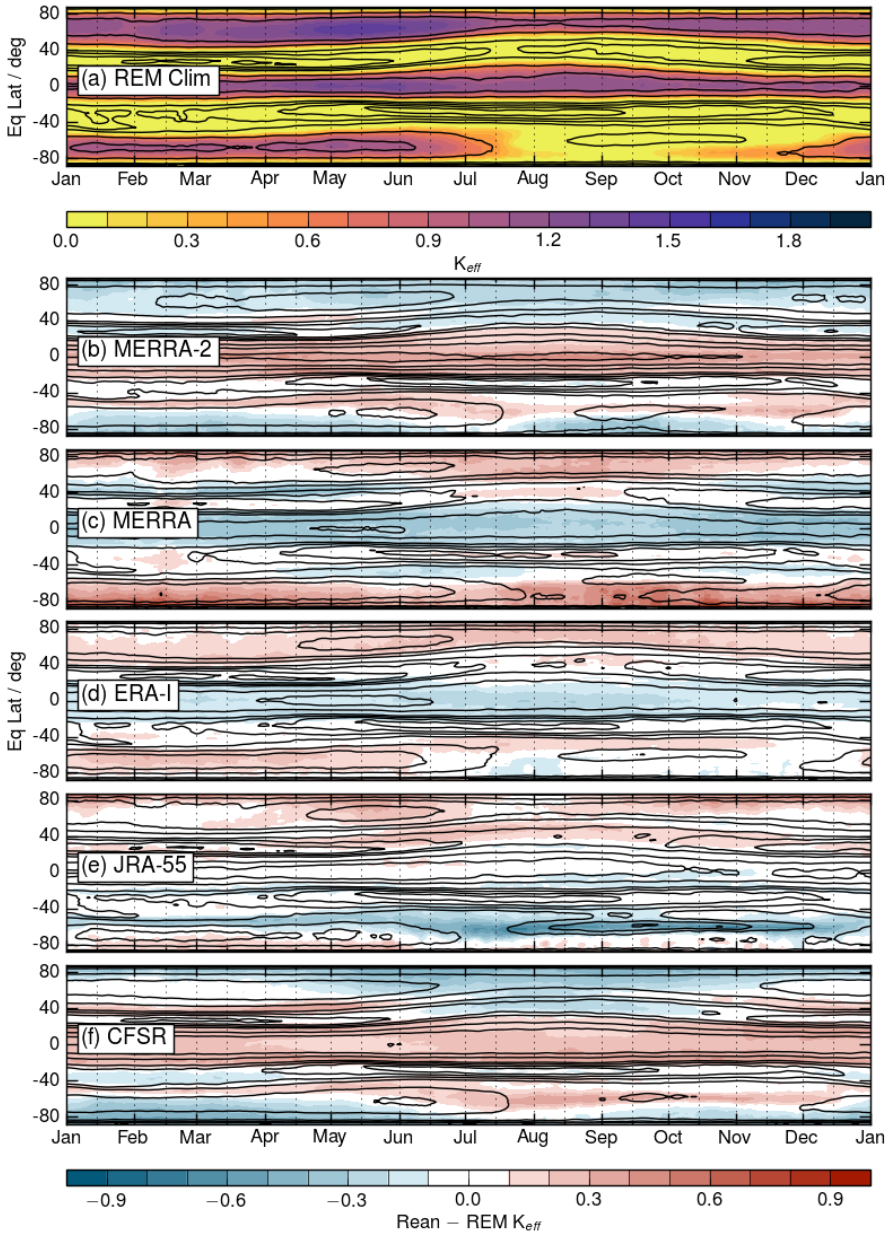

Figure 7.21: *As in* ***Fig. 7.19*** *but for effective diffusivity, scaled as described in the text.*

Figure 7.23 shows a comparison of interannual variability in K_{eff} at 350 K among the reanalyses. Overall patterns are similar to those seen in the climatology, indicating substantial differences in the K_{eff} gradients, but good agreement in the timing and location of mixing and transport barriers. Of particular note is a stepwise change at the time of the transition between CFSR and CFSv2, suggesting that overall CFSv2 indicates more mixing than CFSR; a similar stepwise change is seen at other UTLS levels. The other fields evaluated in the EqL/time plane (sPV and its gradients, wind speed, assimilated ozone) show no more than small discontinuities at this time; the large discontinuity in K_{eff} probably arises because that calculations is highly sensitive to "noise" (that is, small scale structure) in the fields, which is likely to have changed across the CFSR/CFSv2 transition.

While relatively large differences in K_{eff} magnitudes and ranges (even when scaled by the global mean and standard deviation) argue against any quantitative use, all of the reanalysis capture well the timing and locations of mixing regions and transport barriers.

7.5.3 Mass Flux Across 380 K Isentropic Surface

The flux of mass across the 380 K potential temperature surface can be used to directly measure TST in the tropics and also as a proxy for the net STT in the extratropics (*e.g.*, *Olsen et al.*, 2013). The 380 K isentrope is assumed to be the lowest potential temperature surface that lies entirely at or above the tropopause for all seasons; it does not intersect the tropopause where isentropic cross-tropopause flux can occur.

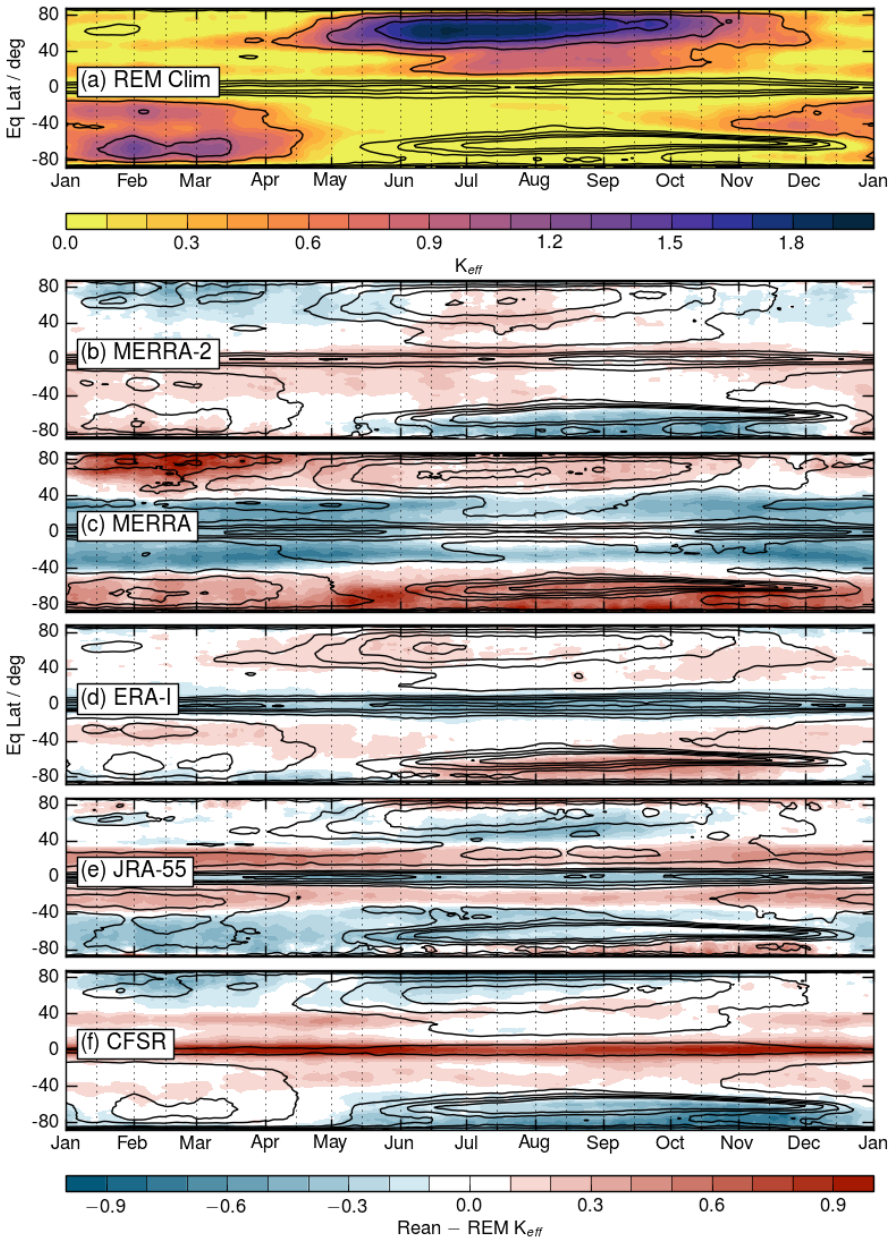

Figure 7.22: *As in* ***Figure 7.20*** *but for effective diffusivity, scaled as described in the text.*

Thus, the 380 K cross-isentrope transport computed from the net heating rate is used to estimate the net bulk flow through the tropopause in the region below. The hemispherically-integrated, extratropical flux can also be considered a single-valued quantity related to the stratospheric circulation in that hemisphere. A change in the net extratropical flux of mass must necessarily be caused by some change in the stratospheric circulation. The net flux of a chemical species, such as ozone, across the 380 K potential temperature surface can be interpreted as the convolution of the total air mass flux and the concentration of the species near the surface. (These quantities are not entirely independent since the transport will impact the concentration of the species). Therefore, it is valuable to evaluate and compare the 380 K air mass flux in the reanalyses, particularly since the meteorological fields are frequently used to drive chemical transport models (CTMs).

The radiative heating rate information provided for each reanalysis (see *Chapter 2*) is postprocessed to get total daily-mean radiative heating rates; in some reanalyses total heating rates are provided, in others (*e.g.*, JRA-55) all of the physical terms provided are summed to get them; the general procedures used and details for each reanalysis are summarized in the context of zonal means by *Martineau et al.* (2018); here, the fields are used on a 1 (for ERA-Interim and CFSR) or 1.25 (for MERRA, MERRA-2, and JRA-55) degree latitude/longitude grid. ASM fields are used for MERRA and MERRA-2. The flux across the 380 K surface is calculated for each reanalysis using these diabatic heating rates interpolated to the 380 K surface, as follows:

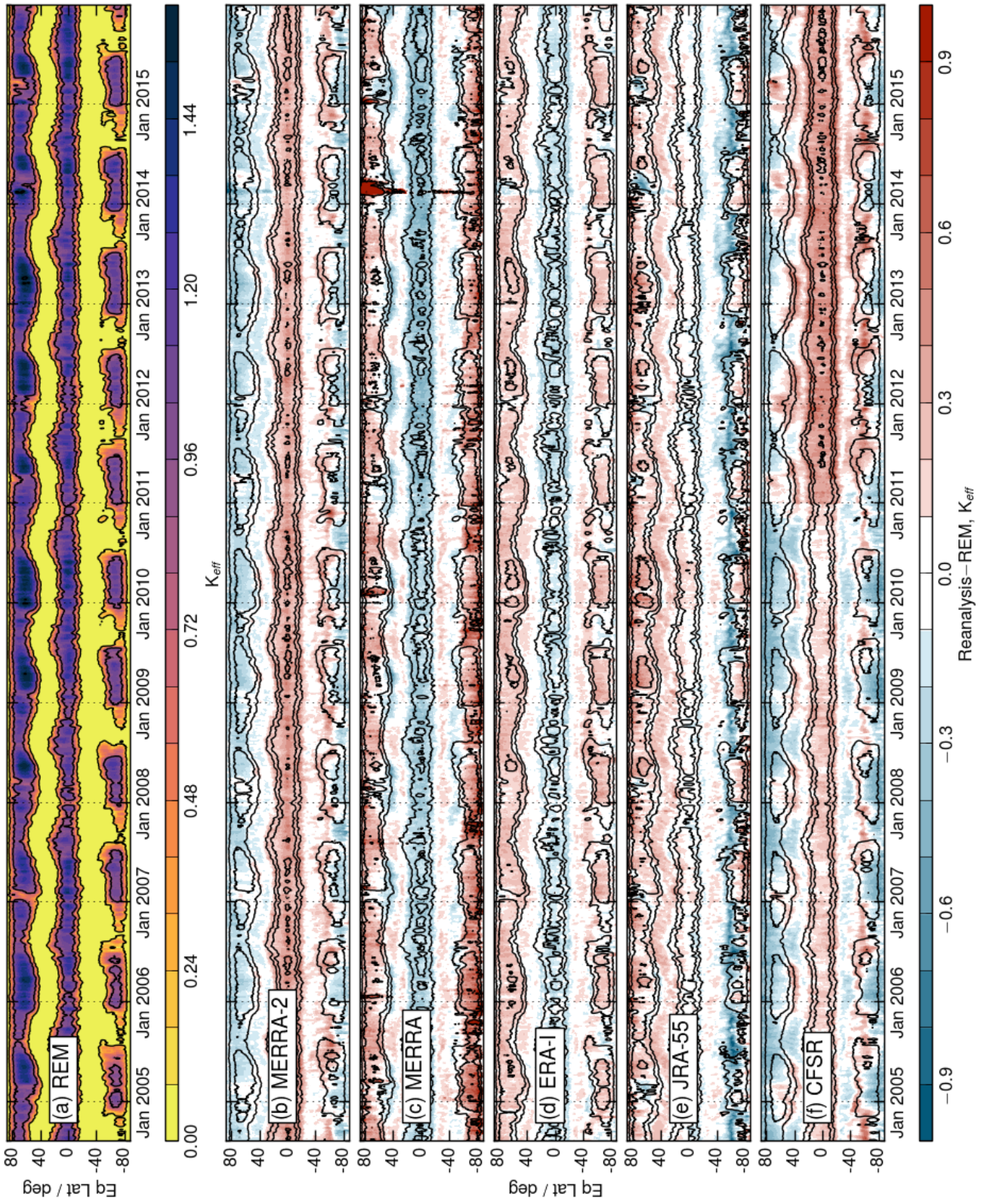

Figure 7.23: *(Top) Time series of effective diffusivity (scaled as described in the text) on the 350 K isentropic surface for 2005 through 2015 as a function of equivalent latitude from (Top) the REM, and (following rows) the difference of each reanalysis from the REM. The black overlays show the same selected contours from the REM on the top panel, and each of the reanalyses on the following panels.*

$$F = -\int \left(\frac{\dot{\theta}}{g}\right)\left(\frac{dp}{d\theta}\right) dA \qquad (7.1),$$

where p is pressure, θ is potential temperature, $\dot{\theta}$ is the diabatic heating rate, and A is the area (*e.g.*, *Schoeberl*, 2004; *Olsen et al.*, 2004). **Figure 7.24** shows the time series for 1980 through 2010 of the annual net mass flux integrated from 30 ° to the pole in each hemisphere. In the NH, all of the reanalyses have similar interannual variability and are well correlated at greater than 99 % confidence except for CFSR, which is not statistically significantly correlated to the other reanalyses. The relative difference between each reanalysis remains fairly constant throughout the time period, although the MERRA-2 flux shows a slight increasing trend during the last decade not seen in the others. This result appears on the surface as if it might be inconsistent with the results of *Boothe and Homeyer* (2017), but the two calculations cannot be directly compared since the 380 K surface is typically substantially above the extratropical tropopause; moreover, the uncertainties in both calculations are difficult to quantify, and may depend on different ways in which the radiative heating rates are provided for the reanalyses. Thus, understanding this possible discrepancy would require further detailed study. The multi-year mean flux and standard deviation of each time series is shown in **Table 7.1**. The multi-year mean of ERA-I is about 10 % - 20 % greater than the other reanalyses excluding CFSR. However, the standard deviation of these time series remains at 3 % - 4 % of each mean, reflecting the high correlation. In contrast, the interannual variability of CFSR is much greater with a standard deviation of 11 %.

In the SH, CFSR is generally better correlated with the other reanalyses, but there is an unexplained downward jump around the year 2000 (**Figure 7.24**). the other reanalyses show a smaller apparent discontinuity around the same time; these changes could results from the relationship of temperature changes during TOVS/ATOVS transition around 1998 to 1999 (see *Chapters 2* and *3*, and *Long et al.*, 2017) being reflected in the diabatic heating rates. The difference of the ERA-I flux from the other reanalyses is much smaller in the SH than it is in the NH. Again, excluding CFSR, the standard deviations of the time series' are consistent at 4 % (**Table 7.1**). Thus, the reanalyses agree that the interannual variability is similar between the hemispheres.

Figure 7.25 shows maps of the 1980 - 2010 average 380 K air mass flux for each reanalysis. In all cases, the patterns are comparable with similar locations of maxima and minima. The maximum upwelling tends to occur in a subtropical band from northeastern Africa to southeast Asia just south of 30 ° N. The minimum upwelling occurs just to the south along the equator from Africa to the Maritime continent. The maximum extratropical downwelling in the SH occurs in a band between about 45 ° S and 60 ° S. In contrast, the maximum downwelling in the NH occurs in the polar region.

The mean "turn-around" latitudes (where the flux is zero) are consistent between all the reanalyses and are located at about 30 ° N and 30 ° S. The differences between the reanalyses occur primarily in the magnitude of the maxima and minima. For example, the maximum upwelling in JRA-55 over India is about 0.9 g cm^{-1} day^{-1} and the maximum in ERA-I at this same location reaches 1.3 g cm^{-1} day^{-1}.

7.6 UTLS Ozone

Chapter 4 provided an overview of assimilated ozone in the most recent reanalysis, and briefly discussed zonal mean diagnostics of UTLS ozone. They found persistent biases in UTLS ozone, as well as inconsistencies in the reanalyses' representations of the ozone annual cycle. We add here comparisons of diagnostics of ozone distributions and evolution in dynamical coordinates and evaluation of transient dynamically-driven low ozone events. Reanalysis ozone fields are compared with v4 Aura Microwave Limb Sounder (MLS) data (*Livesey et al.*, 2018).

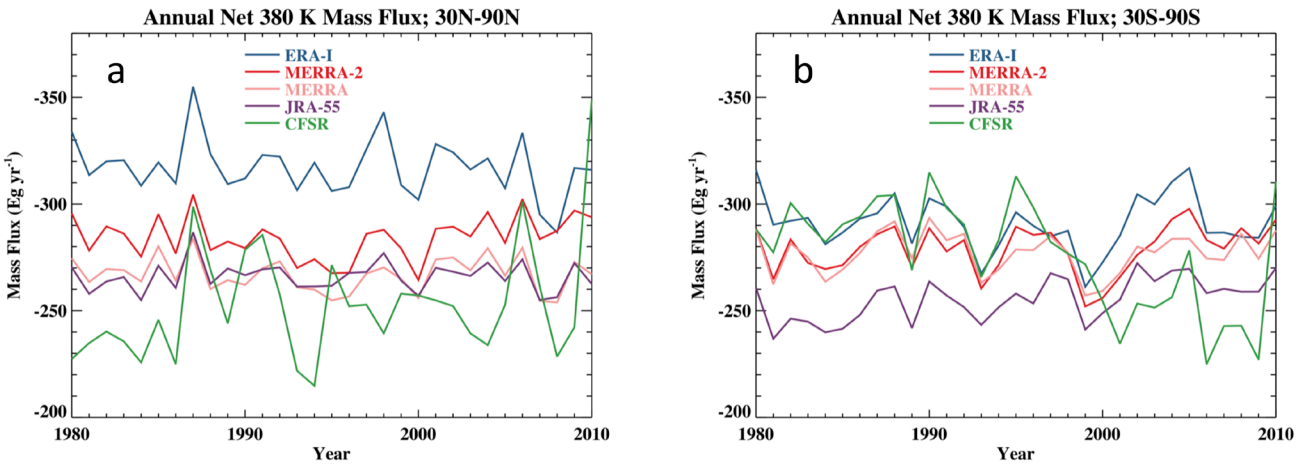

Figure 7.24: *Time series for 1980 through 2010 of the annual net mass flux integrated from 30 °- 90° latitude in (a) the NH and (b) the SH. Values are in 1018 grams per year and negative values denote a net downward flux.*

Table 7.1: *The 1980 - 2010 mean 380 K air mass flux and standard deviation (10^{18} g yr^{-1}) for each reanalysis. Standard deviations are given as a percent of the value in parentheses.*

(10^{18} g yr^{-1})	NH Mean Flux	NH Std Dev	SH Mean Flux	SH Std Dev
ERA-I	317	13 (4%)	291	13 (4%)
MERRA-2	284	10 (4%)	279	11 (4%)
MERRA	267	8 (3%)	277	10 (4%)
JRA-55	266	7 (3%)	255	10 (4%)
CFSR	253	28 (11%)	276	26 (9%)

7.6.1 Ozone in Tropopause-relative Coordinates

Figures 7.26 and **7.27** show reanalysis ozone profiles compared to those from MLS for 2005 through 2015, using the same classification of single and double tropopause regions described in *Section 7.3.3* and *Schwartz et al.* (2015), for each hemisphere's winter season. Generally similar patterns of differences are seen in other seasons. MERRA-2 (which assimilates MLS data throughout the period compared) shows closer agreement with MLS throughout the UTLS and lower stratosphere than the other reanalyses. At altitudes greater than about 5 km above the primary tropopause, ERA-Interim (JRA-55) ozone values become much higher (lower) than those from MLS; however, since the ozone values themselves increase rapidly, above about 10 km above the primary tropopause the differences are less than 10 %.

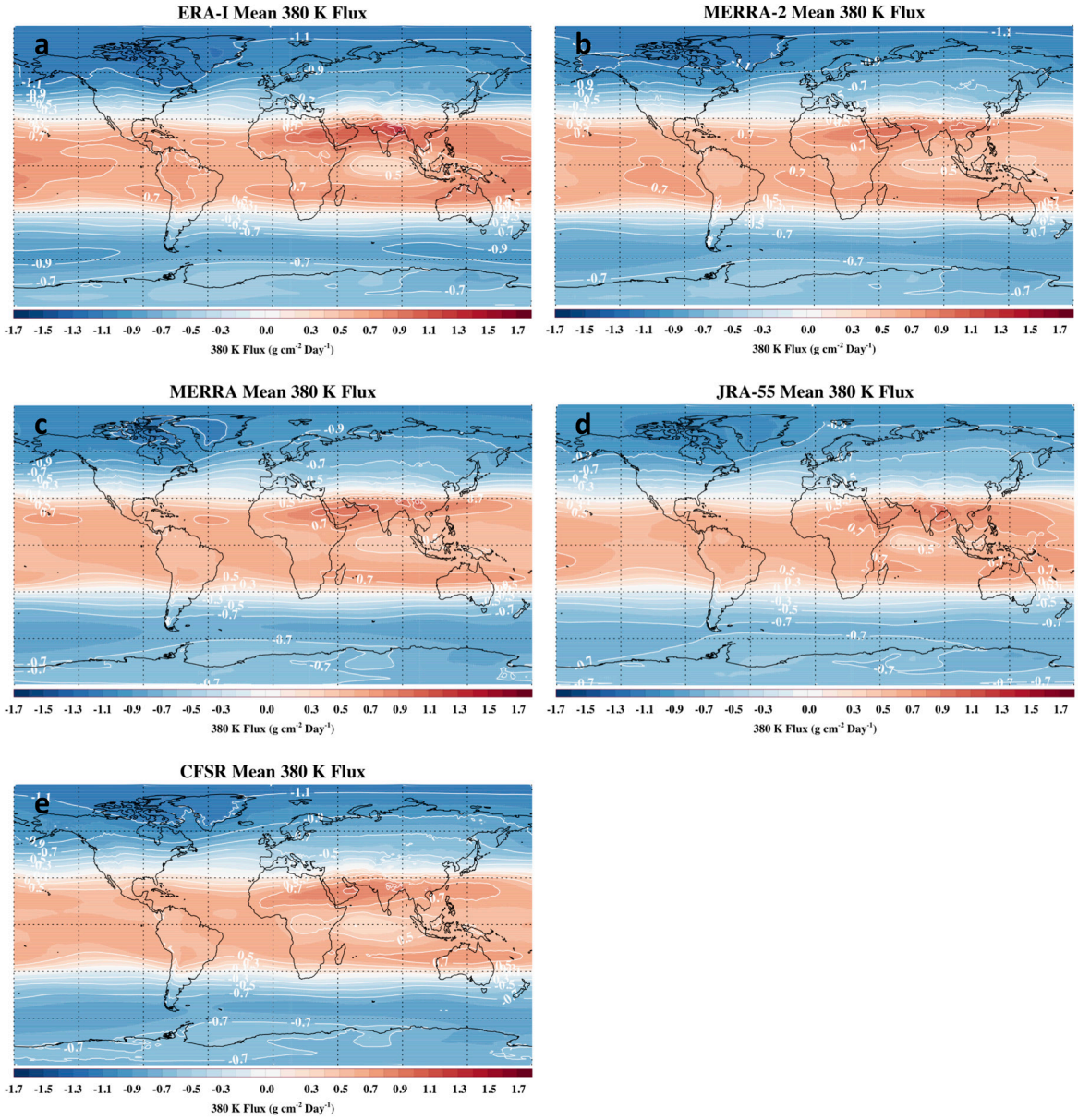

Figure 7.25: *Distribution of the 1980 - 2010 mean air mass flux across the 380 K surface for (a) ERA-I, (b) MERRA-2, (c) MERRA, (d) JRA-55, and (e) CFSR. White contours at increments of 0.2 g cm^{-1} day^{-1}. Negative values denote a net downward flux.*

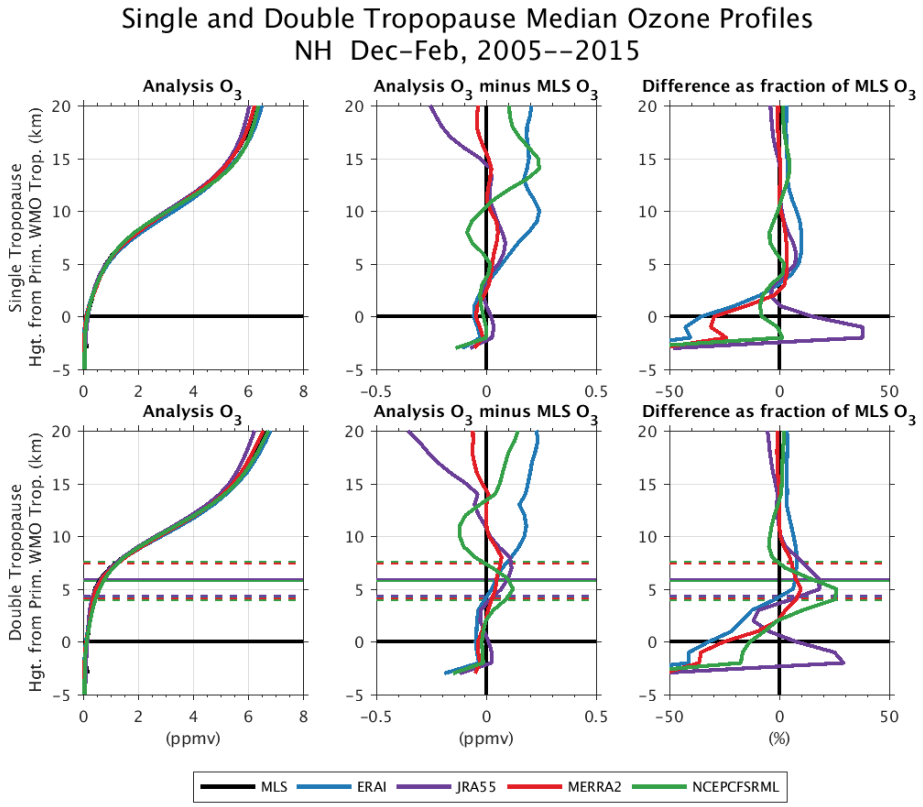

Figure 7.26: *Climatological (2005 - 2015) ozone profiles from MLS and four reanalyses interpolated to the MLS measurement locations for DJF in the NH in (top) single and (bottom) double tropopause regions, plotted relative to primary tropopause altitude. Left plots show the ozone profiles, center plots the mixing ratio differences from MLS, and right plots the difference from MLS expressed as a percent of the MLS value. Horizontal lines show the mean (solid) and standard deviation (dashed) of the mean secondary tropopause altitude from the primary for each reanalysis.*

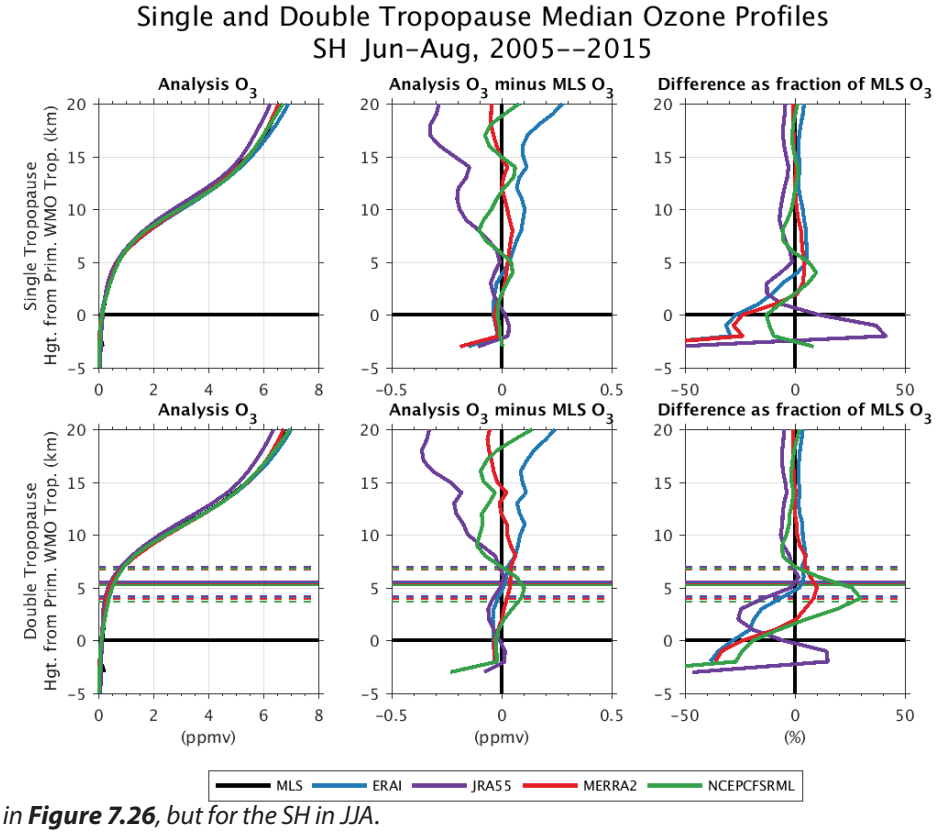

Figure 7.27: *As in* ***Figure 7.26****, but for the SH in JJA.*

In the region up to about 10 km above the primary tropopause, the reanalyses' differences from MLS are up to about ± 100 ppbv (up to about 10 %) in single tropopause regions and about ± 200 ppbv (20 - 30%) in double tropopause regions.

7.6.2 Ozone in Equivalent Latitude Coordinates

Chapter 4 shows a brief overview of stratospheric (520 K and 850 K) and UTLS (350 K) ozone as a function of EqL and time compared with MLS values. Here we update and extend this analysis with a focus on the UTLS. *Section 7.5.2* shows comparisons of some diagnostics of mixing and transport barriers for the same coordinate system and time period, which can be useful for interpretation of similarly mapped trace gas fields. **Figures 7.28** and **7.29** compare the climatological (2005 - 2015) distributions of ozone as a function of EqL over the annual cycle in the reanalyses with that from MLS data at 340 K and 390 K, respectively. At 340 K strong ozone gradients are seen along the transport barrier represented by the tropopause and the subtropical jet (see, *e.g.*, sPV gradients as a function of EqL shown in *Section 7.5.2*), with high ozone in the high latitude winter and spring arising from descent into the stratospheric subvortex. In the SH, decreasing high latitude MLS ozone in September through October demarks the lowest extent of chemical loss in the stratospheric vortex. At 390 K, the high ozone values are confined to the polar winter regions (arising from descent in the stratospheric vortex) and a strong signature of chemical ozone loss is seen from September through December (as noted by *Manney et al.*, 2005; *Santee et al.*, 2011, the SH subvortex does not break up until late December to early January).

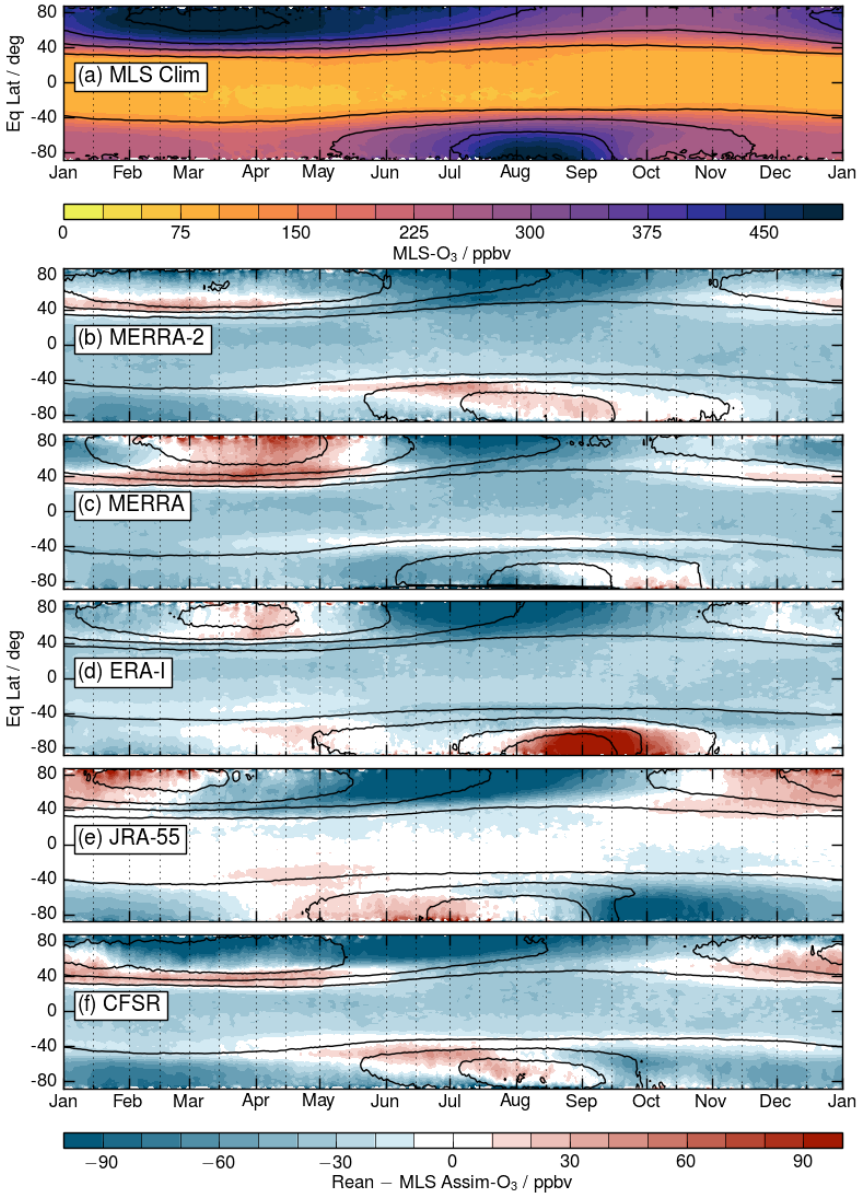

Figure 7.28: *Climatological (2005 - 2015) annual cycle of ozone as a function of EqL at 340 K, showing (top) v4.2 MLS ozone and (following rows) difference (reanalysis – MLS) of MLS from each of the MERRA-2, MERRA, ERA-Interim, JRA-55, and CFSR/CFSv2 reanalyses. The black overlays show the same selected ozone contours, from MLS on the top panel, and each of the reanalyses on the following panels.*

MERRA-2, which assimilates MLS ozone at pressures below about 178 hPa (261 hPa in the last half of 2015, which is included in this record), shows much smaller differences from MLS than the other reanalyses at 390 K and slightly smaller differences at 340 K (generally below the level where MLS data are assimilated). At 390 K, all of the reanalyses overestimate ozone in the SH spring (that is, they underestimate chemical loss); the differences are smallest for MERRA-2 and largest for ERA-Interim. Large differences are also seen in the NH subvortex, with MERRA and, to a lesser degree, CFSR, underestimating ozone and ERA-Interim overestimating it. All reanalyses tend to underestimate 390 K ozone in the SH winter before extensive chemical ozone loss has occurred, though the magnitude of the underestimate in MERRA-2 is smaller. At 340 K the reanalyses generally tend to underestimate MLS ozone except in the polar winter to spring – ERA-Interim substantially overestimates SH polar ozone (by over 20 %) in August through October, and the other reanalyses overestimate polar winter/spring ozone by around 10 %, with varying timing and EqL extent. Despite these differences, all of the reanalyses represent the seasonal cycle well qualitatively (that is, timing and approximate magnitude) at both levels.

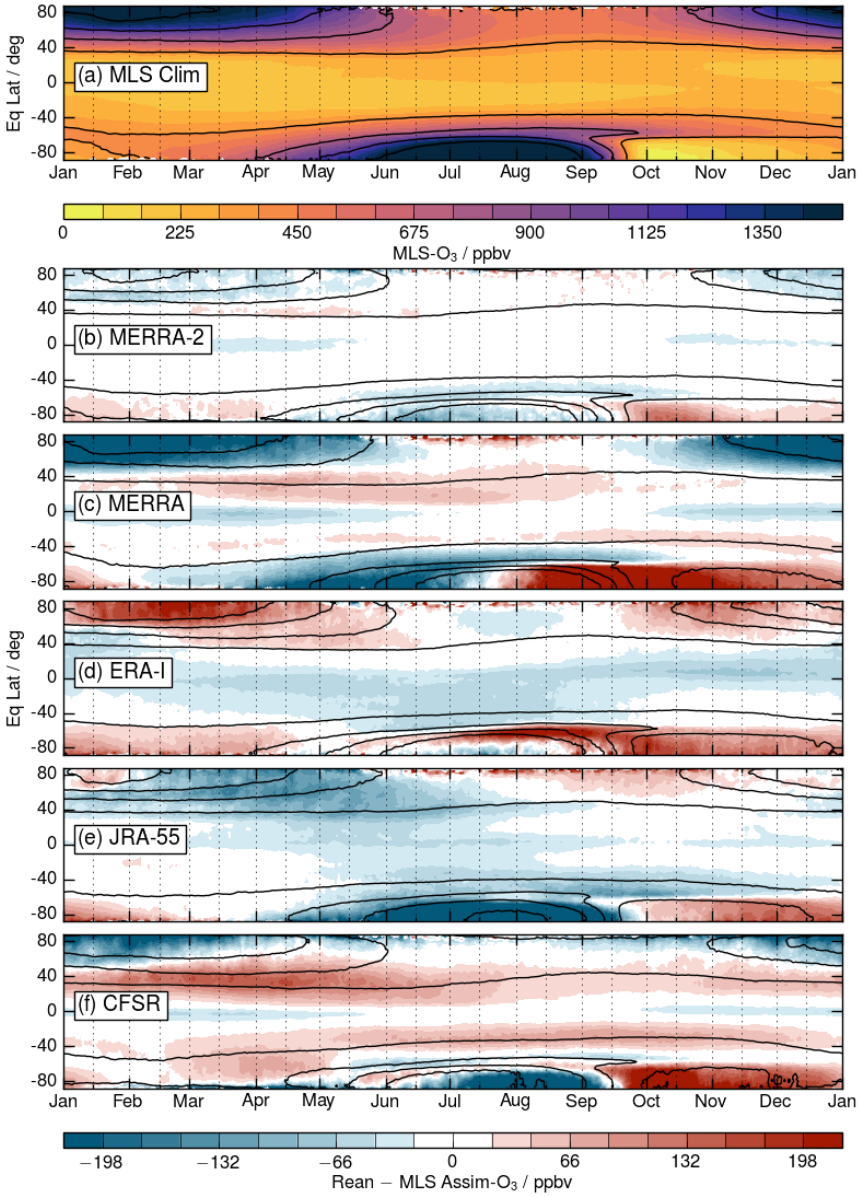

Figure 7.29: *As in* ***Fig. 7.28****, but at 390 K*

Figures 7.30 and **7.31** show the time series from 2005 through 2015 of daily MLS ozone as a function of EqL and the differences from the reanalyses. The general features noted in the climatology are also apparent here, and the reanalyses appear to do a reasonable job of capturing interannual variations in that the differences from MLS are not more extreme in extreme years. However, several discontinuities in the time series are worth noting: At the beginning of June 2015, MERRA-2 switched from assimilating v2 to v4 MLS ozone profile data, and the lowest level assimilated changed from about 178 hPa to 261 hPa (for May 2016 and thereafter, not shown in this analysis, this was changed to 215 hPa). (*Wargan et al.*, 2017). A small discontinuity is seen in the MERRA-2 / MLS differences at this time, with slightly better agreement at 340 K and overall slightly more negative differences at 390 K. ERA-Interim also shows several discontinuities related to changes in MLS data assimilated. MLS v2.2 data were assimilated in 2008, at pressure levels up to 215 hPa, and MLS NRT data were assimilated starting in mid-2009 (v2-NRT through 2012 and v3-NRT thereafter). MLS v2.2-NRT ozone data were very limited and were not suitable for scientific use at pressures above 68 hPa (*Lambert et al.*, 2008); during the period when these data were assimilated, the ERA-Interim fields show biases with v4 MLS data that are as large as or larger than those before any MLS data were assimilated. A marked improvement is seen when ERA-Interim began assimilating v3-NRT data, which speaks to the improvements in those retrievals (which allowed these data to be assimilated down through 215 hPa), and the biases are similar to those in 2008 when operational MLS ozone data were assimilated down to the same presssure level.

7.6.3 Ozone in Jet-relative Coordinates

Figures 7.32 and **7.33** show climatological comparisons of assimilated ozone distributions in jet-relative coordinates (see, *e.g.*, *Manney et al.*, 2011) with Aura MLS ozone in the same coordinate system. The assimilated ozone is evaluated both as mapped directly from the native reanalysis grid to jet coordinates (right column in these figures), and as first interpolated (bi-linearly in the horizontal and linearly in time) to the MLS measurement locations and then mapped into jet coordinates (center column in these figures; the latter is restricted to ozone at the same geographic locations, so provides a more fair comparison). The differences in MLS data when mapped to jet coordinates using jet information from each of the reanalyses (left column in these figures) are relatively small (up to about 15 %), suggesting that, at least in the zonal mean climatological view, all of the reanalyses provide jet information that is appropriate for this mapping; this is consistent with the results of (*Manney et al.*, 2017, see *Section 7.4.2*) showing a consistent climatology of the upper tropospheric jets in all of the most recent reanalyses when analyzed at (or near) their native model resolutions. That the differences between MERRA and MERRA-2 in this mapping are much smaller than those between MERRA-2 and the other reanalyses suggests that these arise primarily from the differing grids/resolutions of the reanalyses (those of MERRA and MERRA-2 being the most similar in the horizontal and the same in the vertical).

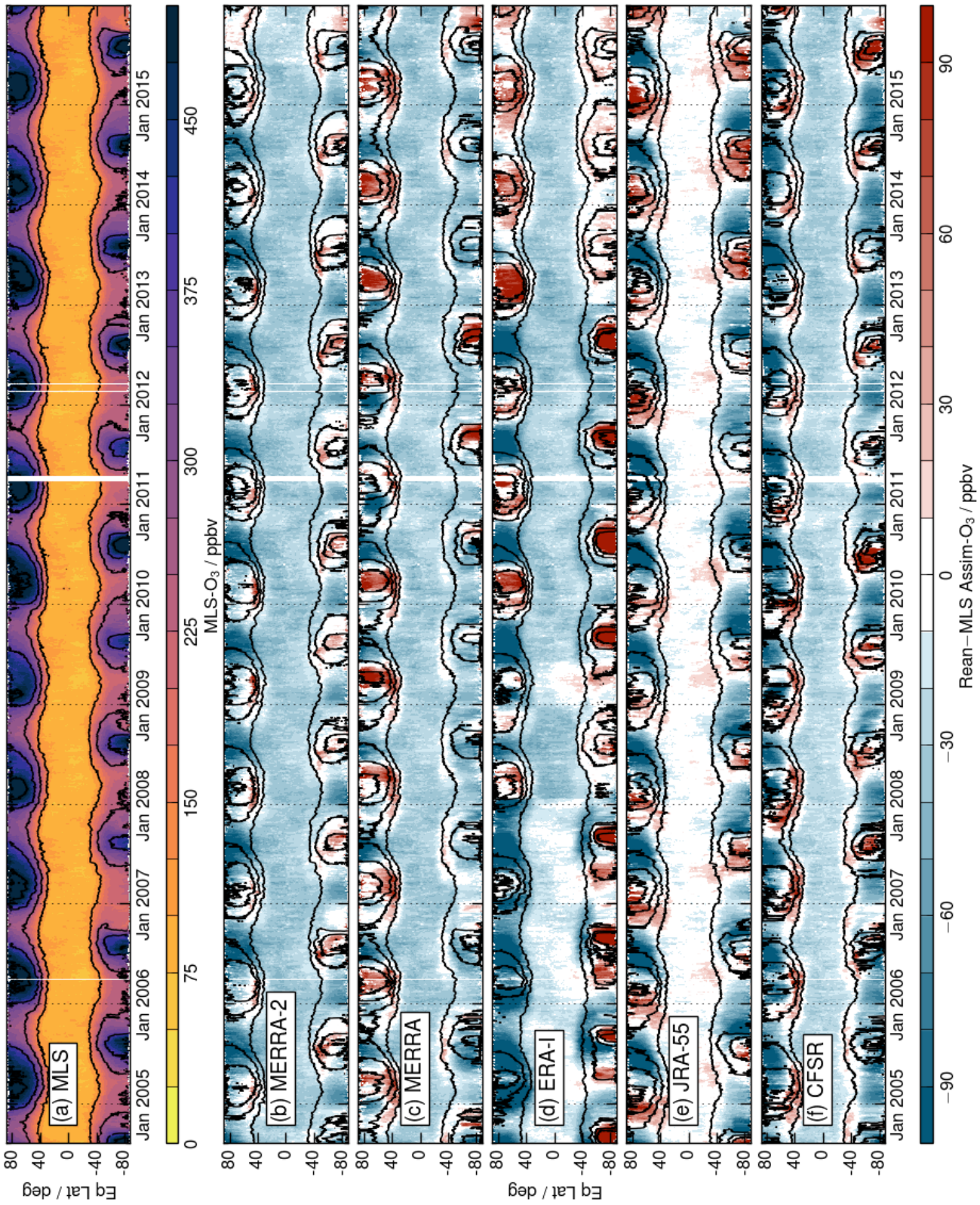

Figure 7.30: *(Top) Time series of 340 K MLS ozone for 2005 through 2015 and (following rows) the difference of each reanalysis from MLS. The black overlays show the same selected ozone contours, from MLS on the top panel, and each of the reanalyses on the following panels.*

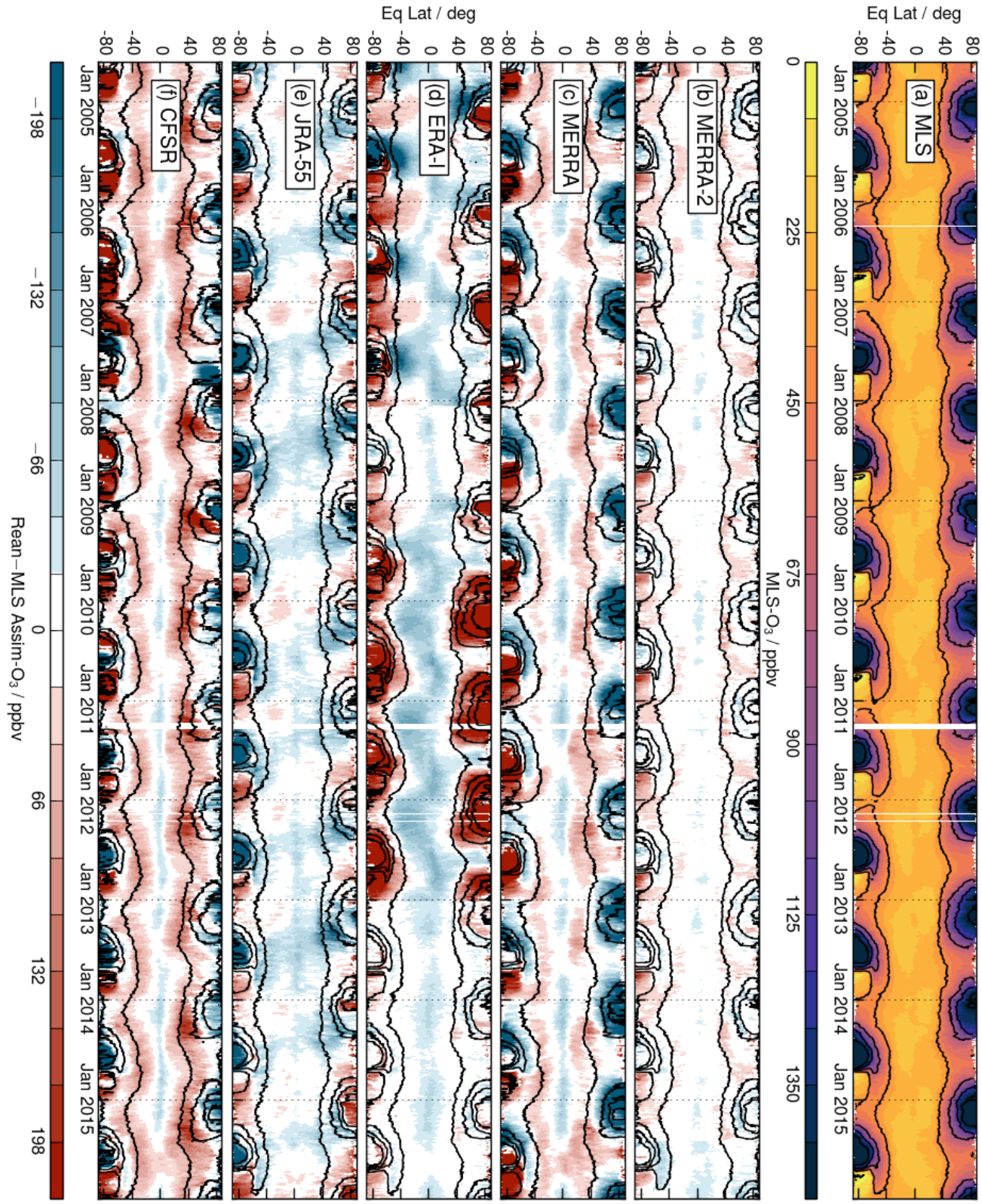

Figure 7.31: *As in* ***Figure 7.30*** *but at 390 K.*

Figure 7.32 shows reasonably good agreement between ozone in all of the reanalyses and MLS near and above the tropopause, with the sign of the differences varying in different reanalyses. Except in the SH in JRA-55, all of the reanalyses show lower ozone than MLS in the region below about 2 km below the tropopause. Since earlier versions of MLS data have shown high biases in this region (*e.g.*, *Hubert et al.*, 2016), it is unclear whether this is primarily due to MLS biases or whether the reanalyses may capture less stratosphere-to-troposphere transport than the MLS measurements indicate. The low bias in reanalysis ozone in the extratropical upper troposphere compared to MLS is consistent with that shown in zonal mean satellite data comparisons in *Chapter 4*. The reanalyses re-mapped from their native grids often, but not always, show similar patterns of differences from MLS data to those re-mapped after being interpolated to the MLS measurement locations. That these differences do sometimes show different qualitative patterns suggests that, even with the dense sampling of MLS data, the satellite sampling can be an important confounding factor in comparisons that are not based on geographically coincident data even when those data are mapped (as they are here) in coordinate systems that match dynamically similar air masses.

Similar results are seen for cross-sections in jet coordinates in other seasons. **Figure 7.33** shows the annual cycle in jet-coordinate MLS and reanalysis ozone as a climatological (1980 - 2015) slice as a function of latitude from the jet and time at the subtropical jet core altitude. The timing of the seasonal cycle is well-defined and agrees well with that from MLS in all of the reanalyses studied.

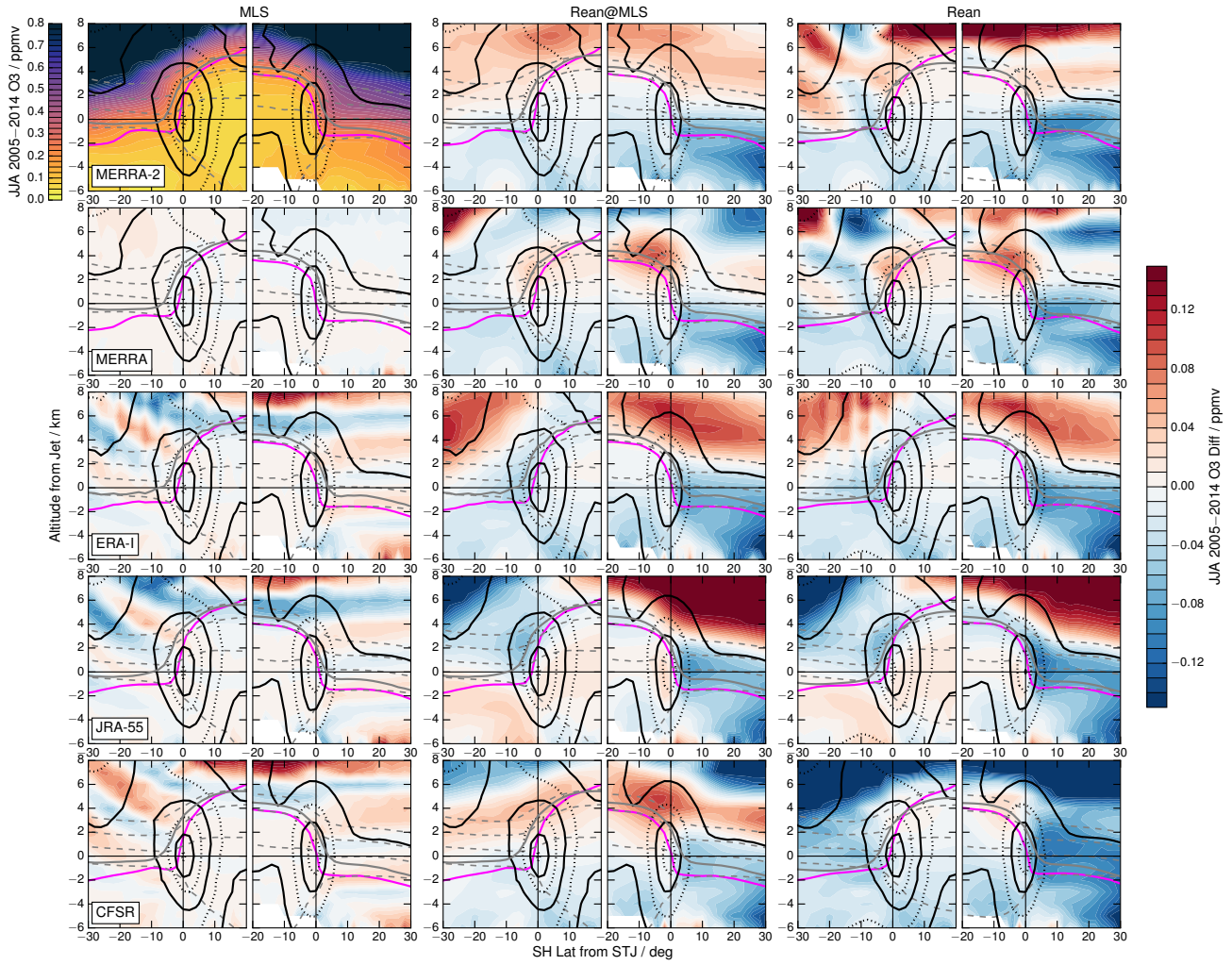

Figure 7.32: *JJA mean climatological ozone in jet-relative coordinates, for 2005 through 2014. Top left plots shows MLS ozone mapped in jet coordinates using MERRA-2; the remainder of the left column shows the difference between that and MLS ozone mapped to jet coordinates with each of the other reanalyses. The center column shows the difference between each reanalyses' ozone mapped after interpolating to the MLS measurement locations and the MLS ozone mapped with that reanalyses; the right column is similar, except the reanalysis ozone is mapped into jet coordinates directly from its native grid. Overlays show: Windspeeds (black, from 10 to 80 by 10 m s^{-1}, even values dotted), potential temperature (grey dashed, 330 to 390 by 20 K), the 3.5 PVU contour (magenta, negative in SH), and the LRT (grey solid).*

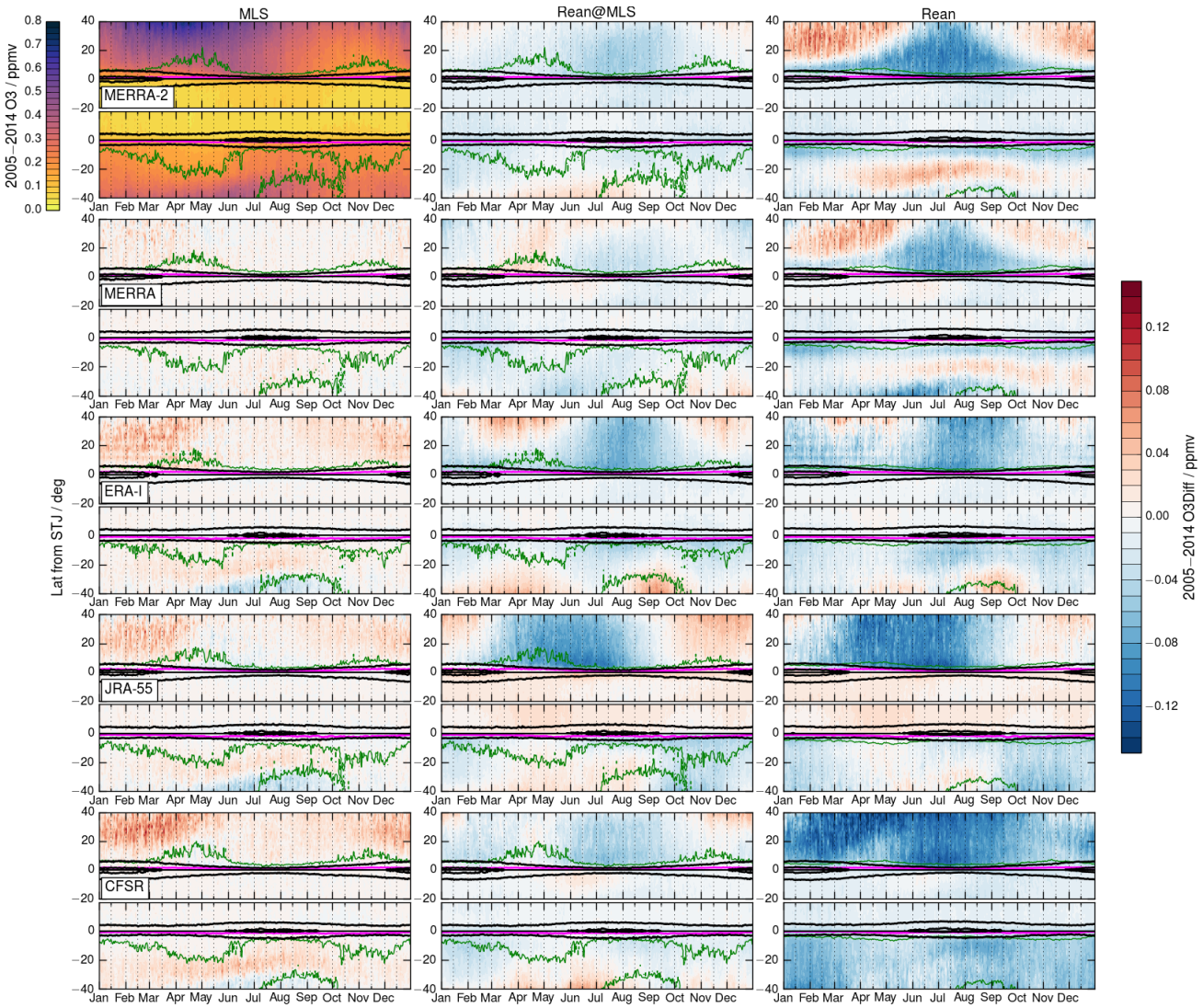

Figure 7.33: *Annual cycle in climatological (2005 - 2014) ozone at the subtropical jet core altitude as a function of time and latitude from the subtropical jet. Columns are as in* ***Figure 7.32****. Overlays show: Windspeeds (black, 40, 60, and 80 m s^{-1}), the 3.5 PVU contour (magenta, negative in SH), and the LRT (green).*

At the level of the jet core (where the ozone fields are strongly influenced by the subtropical jet), it is clear that interpolation to MLS locations before mapping into this dynamical coordinate is critical in providing a fair comparison, and thus that sampling effects are substantial. When comparing the reanalyses first interpolated to MLS measurement locations with MLS, the differences themselves show a seasonal cycle that varies among the reanalyses. Those differences are largest (up to about 20 % in the NH spring and summer) in JRA-55 and smallest (below 10 %) in MERRA-2; this is unsurprising since MERRA-2 assimilates MLS ozone and JRA-55 has the crudest ozone assimilation system of the reanalyses studies here.

7.6.4 Ozone mini-holes

Dynamical redistribution of ozone can produce large transient and localized reductions in total column ozone, also known as mini-holes (*e.g., Hood et al.*, 2001; *James*, 1998a,b; *Newman et al.*, 1988). *Millán and Manney* (2017) analyzed the representation of mini-hole events in the northern hemisphere from several reanalyses (ERA-Interim, MERRA, MERRA-2, CFSR/CFSv2, and JRA-55) using data from OMI (*Levelt et al.*, 2006) and MLS (*Waters et al.*, 2006). OMI column ozone data allow us to compare their geographical representation while MLS ozone profile data allow us to study their vertical representation. Several definitions of mini-holes exist in the literature (*e.g., Koch et al.*, 2005; *Hood et al.*, 2001; *James*, 1998a). Here, we define mini-hole events as regions where the total column ozone value is less than 25 % below the monthly mean. Further, we only consider as mini-hole events those ozone fluctuations with an area larger than 200,000 km^2.

Millán and Manney (2017) found that the reanalysis fields display the same mini-hole seasonal variability as OMI, with more mini-hole events during winter when the atmosphere is more dynamically active (see **Figure 7.34**).

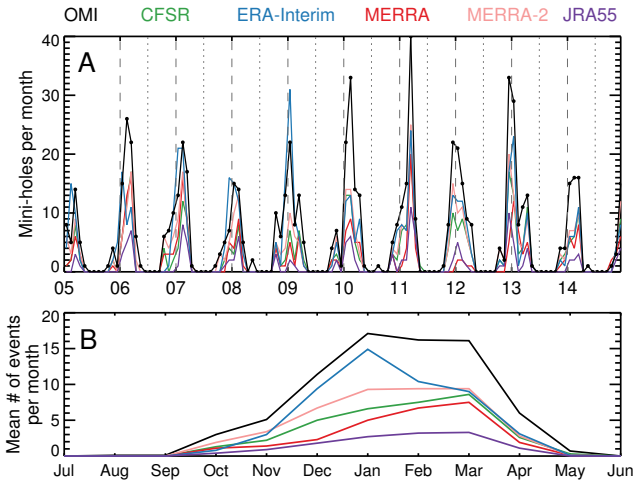

Figure 7.34: *(A) Mini-hole events per month during 2005 - 2014 in the northern hemisphere as found in OMI data and reanalysis fields (Black, green, blue, red, pink, purple lines represent OMI, CFSR/CFSv2, ERA-Interim, MERRA, MERRA-2, and JRA-55 respectively). Dashed vertical lines indicate the beginning of each January, dotted vertical lines the beginning of each July. (B) Mean number of mini-hole events in a given month (during 2005 - 2014). (From Millan and Manney, 2017.)*

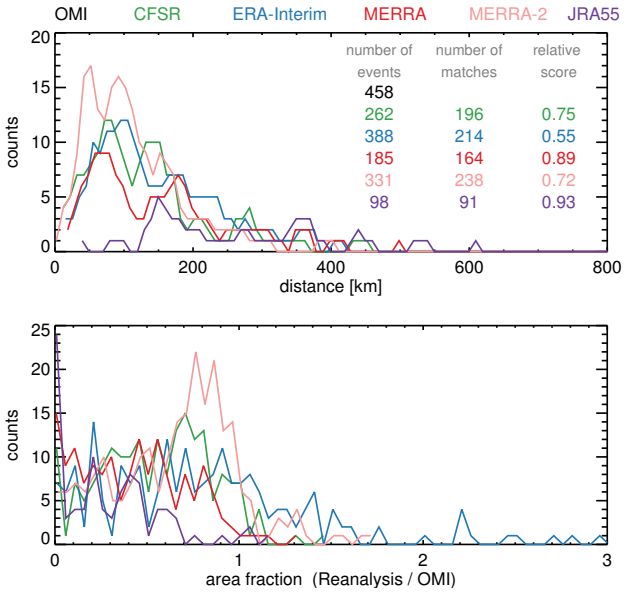

Figure 7.35: *(Top) Histograms of the distance between the mini-hole events found in the reanalysis fields and the ones found in OMI data (Black, green, blue, red, pink, purple lines represent OMI, CFSR, ERA-Interim, MERRA, MERRA-2, and JRA-55 respectively). Also shown is the total number of events as well as the number of matches between the events found in OMI and in the reanalyses. (Bottom) Histograms of the area fraction of mini-hole events. (From Millan and Manney, 2017.)*

OMI and the reanalysis fields also display similar minihole geographical distributions, with mini-holes occurring most frequently over the North Atlantic storm tracks. All of the reanalyses studied underestimate the number of mini-hole events, with the underestimation ranging from 34 % less for ERA-Interim up to 83 % less for JRA-55. Further, reanalyses typically underestimate the area of the mini-hole events and most of the time are between 75 km and 300 km away from the events found in OMI (see **Figure 7.35**). Mini-holes found in CFSR/CFSv2, MERRA, MERRA-2 and ERA-Interim reanalyses display an eastward bias with respect to the events found in OMI data. JRA-55 does not show a consistent bias direction, a feature that is most likely related to their crude treatment of ozone (see *Chapters 2* and *4*).

The composite view of the vertical representation of mini-hole events agrees with previously reported mechanisms for dynamical mini-hole formation: Anticyclonic poleward Rossby wave breaking occurs in the UTLS; local uplift of air near the tropopause brings ozone poor air into the column and is accompanied by equatorward advection of polar air in the mid-stratosphere. On average, in the events found in both MLS and the reanalyses, the vertical structure in the reanalyses qualitatively agrees with that in MLS in that about two-thirds of the ozone reduction originates in the UTLS and the rest in the mid-stratosphere. Mini-hole regions do typically show more double tropopauses (DTs) than in the surrounding air, but the association is not strong because DTs occur most frequently above strong cyclonic circulation systems while mini-holes occur most frequently above anticyclonic systems.

7.7 Summary and Recommendations

In this chapter, we evaluate an extensive set of diagnostics that are critical to understanding ExUTLS dynamical and transport processes, including the representation of the extratropical tropopause, UT jet streams, mixing and transport diagnostics, and ozone distributions and evolution. Because representing these processes requires high resolution, we focus on the recent full-input reanalyses, including MERRA, MERRA-2, ERA-Interim, JRA-55, and CFSR/CFSv2, and provide some comparisons that demonstrate just how important resolution is. The conventional input JRA-55C reanalysis was also compared for a few diagnostics. Earlier reanalysis (*e.g.*, NCEP-R1 and NCEP-R2, ERA-40) are not suitable for detailed UTLS studies because of their coarse resolution, especially in the vertical, and are not evaluated here. We find broadly consistent behavior among modern reanalyses in their representation of the extratropical tropopause, UT jet streams, and transport and mixing diagnostics.

Larger differences are found in the representation of ozone in the ExUTLS, thought to be largely because of differences in treatment of ozone among the reanalyses (*Davis et al.*, 2017) (also see *Chapter 4*). Our key finding and recommendations are given below:

Key findings:

- The reanalyses evaluated here agree well, with each other and with high-resolution radiosonde observations, on the location of the tropopause. CFSR/CFSv2 shows the lowest errors with respect to lapse rate tropopauses in radiosonde data of the analyses evaluated.

- Long-term trends (1981 - 2015) in tropopause altitude are in broad agreement both among the reanalyses and with observations, except for CFSR/CFSv2.

- The representation of multiple lapse-rate tropopause altitudes, which can be an indication of lateral STE events between the tropical UT and ExLS, is highly dependent on the vertical grid resolution of reanalyses. CFSR/CFSv2 has the highest frequency of multiple tropopauses and the highest ExUTLS resolution of the renalyses evaluated here.

- Using pressure and model-level versions of CFSR/CFSv2, we have shown that the degraded vertical resolution in the pressure level fields makes them unsuitable for identifying tropopause locations, especially for multiple tropopause situations.

- JRA-55C was shown to be unsuitable for identifying multiple tropopauses because of its inability to qualitatively reproduce the distributions in SH high latitudes.

- Despite a general under-representation in multiple tropopause frequency compared to observations, most modern reanalyses reproduce the pattern and sign of observed long-term trends in multiple tropopause frequency.

- The reanalyses show good overall agreement in representation of the climatology of UT jets and of the subvortex jet in the LMS.

- Robust trends in UT jets (latitude, altitude, and windspeed) are limited to particular longitude regions and seasons. Disagreement among the reanalyses is most common for the SH jets; in particular, MERRA-2 and/or CFSR/CFSv2 sometimes differ from the other reanalyses even in the sign of the SH jet latitude trends.

- Lagrangian estimates of STE using full 3D kinematic winds are in broad agreement among the reanalyses, with some important differences in the locations and long-term changes of TST and STT. Transport estimates are sensitive to the choice of vertical wind field (i.e., diabatic vs. kinematic) and the time period analyzed.

- Mixing diagnostics including effective diffusivity and PV gradients as a function of EqL show generally good agreement in climatological seasonal cycle and interannual variability.

- Mass flux across the 380 K isentropic surface agrees well between MERRA-2, ERA-Interim and JRA-55, with CFSR/CFSv2 showing inconsistencies in the seasonal cycle.

- Climatological ozone distributions and seasonal cycles show good qualitative agreement; because of the large differences in the ozone products assimilated and the methods of assimilating them, this points to good representation of the dynamics in the UTLS where ozone changes are primarily driven by dynamical and transport processes.

- The reanalyses' ozone mapped in EqL generally reproduces at least qualitatively the interannual variability in MLS observed ozone, but ERA-Interim shows several step function changes that are related to changes in the versions of MLS ozone assimilated; in particular, in mid-2009 through 2012, large biases in ERA-Interim UTLS ozone arise from use of an early version of MLS NRT data.

Recommendations and Future Work:

- Based on previous work, and additional studies shown here, we only recommend the recent high-resolution reanalyses (MERRA-2, ERA-Interim, JRA-55, and CFSR/CFSv2 are such analyses evaluated herein) as suitable for ExUTLS dynamical and transport studies. The dynamical diagnostics derived from these reanalyses indicate that they are all suitable for use in such studies with some limitations.

- Given the inherent sensitivities of transport diagnostics to the method (*e.g.*, Lagrangian *vs.* Eulerian) and time period used, future reanalyses should incorporate tracers (*e.g.*, stratospheric mean age) for more direct transport comparisons.

- A few diagnostics (*e.g.*, effective diffusivity in CFSR/CFSv2; ozone in ERA-Interim) show substantial discontinuities when assessed over many years, and thus should be used with extreme caution and awareness in any analysis of those diagnostics.

- Despite the above point, further studies of mixing diagnostics (which cannot be compared with direct observations), including trends, comparisons with free-running models, and assessment in relation to trace gas observations, could provide useful information for model and DAS improvement.

- Because many diagnostics in this chapter cannot be directly compared with data, using multiple reanalyses and assessing agreement among them should be an important part of ExUTLS studies.

- For diagnostics that cannot be directly compared with data, and in light of similar changes in input data, agreement among the reanalyses should be regarded as a necessary, but by no means a sufficient, condition for robustness of trends.

- As is the case for diagnostics described in other chapters (*e.g.*, *Chapter 10*), differences between the PV fields arising from differing products provided by the reanalysis centers add to the uncertainties in the evaluations. It would be helpful in the future for all reanalysis centers to provide PV on the model grids.

- The results from reanalyses assimilating MLS ozone (which has relatively high vertical resolution compared to other ozone profilers currently used) show promise for future improvements, and more attention to consistently assimilating high-resolution ozone observations in future reanalyses would be extremely beneficial to understanding the processes controlling ozone in this region where it is of such great importance to the radiative balance.

- Future work is needed to better elucidate the role of various elements of model design in producing observed differences in tropopause location and characteristics (*e.g.*, through idealized simulations with the core models of each reanalysis).

- In the future, the accuracy of tropopause identifications in reanalyses should improve as the vertical grid spacing decreases. These diagnostics should be evaluated in forthcoming reanalyses (most immediately, in ERA5) and the impacts of these improvements on estimates of STE and their long-term changes should be explored.

- The accuracy of transport estimates from reanalyses is largely unknown, since global estimates of transport from observing systems are not available and the outcomes are sensitive to the input fields and methods used. Comparison of transport calculations using reanalysis wind fields and trace gas observations is one path to examine the accuracy of transport in reanalyses.

- Errors in transport calculations may also be gleaned from comparison of trajectory calculations driven by the reanalysis winds to long-duration balloon observations when available. However, such observations are infrequent and sometimes assimilated into the reanalysis, which limits their utility for validation studies.

- Given the known errors in trajectory and other transport calculations that arise from coarse temporal resolution of input wind fields (*e.g.*, *Stohl*, 1998; *Bowman et al.*, 2013), more frequent 3D wind field outputs are desired from future reanalyses. Such wind fields, which are already available for ERA5, will allow for improved understanding of transport and STE (*e.g.*, see early work using ERA5 in *Hoffmann et al.*, 2019).

- For studies of reanalysis ozone, several datasets are available for comparisons that have yet to be fully utilized; we recommend further comparisons with data from other satellite instruments (*e.g.*, the Odin OSIRIS and ACE-FTS instruments), ozone sondes, and both campaign and longer term aircraft datasets (*e.g.*, START-08, WISE, IAGOS). Some such studies will be done under the aegis of the SPARC OCTAV-UTLS activity.

- Increased horizontal and vertical grid resolution will also be beneficial for reducing errors in transport calculations and enable analysis of processes at smaller scales.

Figure 7.36 summarizes the results for the main diagnostics evaluated herein. Overall, the latest generation of reanalyses shows good quality for representing UTLS dynamics and transport. Most of the diagnostics discussed herein cannot be verified with observations directly, and, while differences are generally relatively small, the agreement is rarely so good that we can say they are "demonstrated suitable" in cases where direct verification is not possible; hence most of the reanalyses are deemed "suitable with limitations" or "use with caution" for most diagnostics.

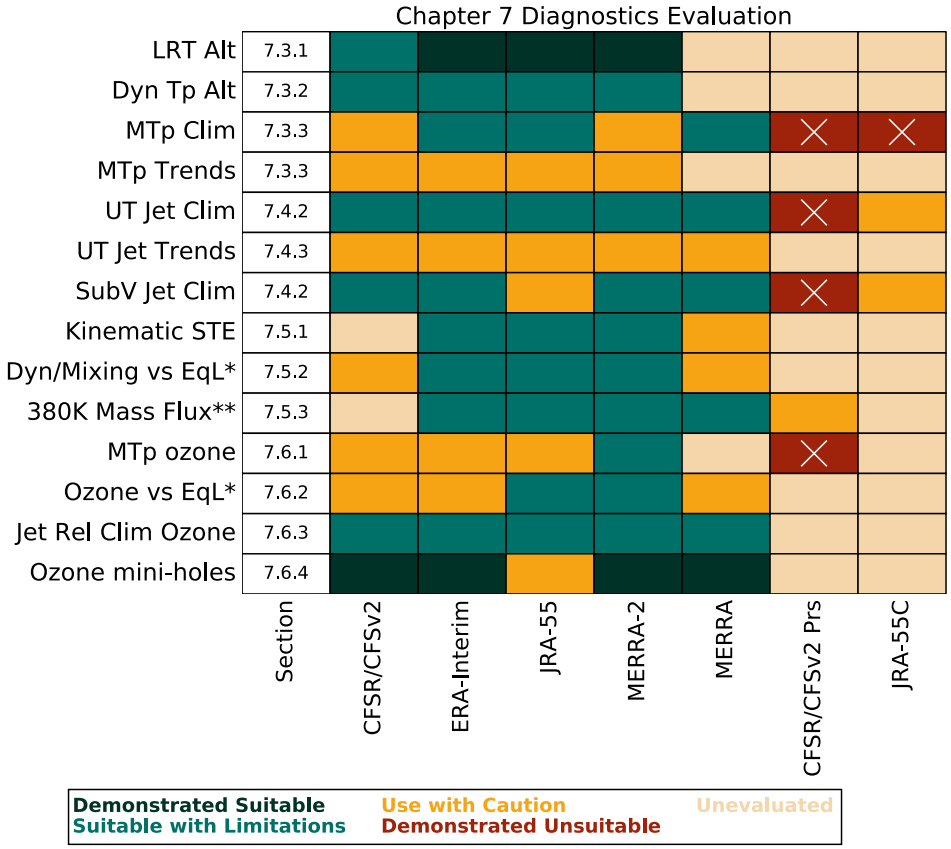

* Because the analysis as a function of EqL depends critically on PV (which is used to compute the EqL), those reanalyses where we have concerns about the PV fields are rated "use with caution" even in the absence of obvious "red flags". "CFSR/CFSv2 Prs" indicates CFSR/CFSv2 was used as interpolated to standard pressure levels; otherwise all diagnostics are calculated using model level data for all reanalyses except where specifically noted.

** The 380 K mass flux analysis was done using pressure level data for all reanalyses.

Figure 7.36: *Summary evaluation table for Chapter 7 diagnostics, per "key findings" highlighted above.*

Data availability

Access information for reanalysis datasets is given in *Chapter 2*.

The version 4.2 MLS ozone data are publicly available at **https://disc.gsfc.nasa.gov/datasets?page=1&source=Aura%20MLS&processingLevel=2**

JETPAC products at MLS locations used in the ozone analysis are publicly available at **https://mls.jpl.nasa.gov/dmp/**

The NWS radiosonde data used were retrieved from the Integrated Global Radiosonde Archive (IGRA; *Durre et al.*, 2016, **https://doi.org/10.7289/V5X63K0Q**).

Additional JETPAC products that are shown herein are not calculated operationally, but diagnostics that have been produced are available upon request.

Acknowledgements

We thank the reanalysis centres for their consistent help throughout the project in providing and helping us understand the reanalysis datasets. We thank the Aura Microwave Limb Sounder (MLS) science team for providing their data, and the MLS team at JPL, especially Brian Knosp and Ryan Fuller, for data management and analysis support. We thank Michelle Santee, Nathaniel Livesey, Kirstin Krüger, Susann Tegtmeier, Daniel Kunkel, and Peter Hoor for helpful discussions and comments during the project, and the reviewers and review editors for their careful reading and helpful comments.

References

Abalos, M., B. Legras, B., and E. Shuckburgh, 2016: Interannual variability in effective diffusivity in the upper troposphere/lower stratosphere from reanalysis data. *Q. J. R. Meteorol. Soc.*, **142**, 1847 - 1861, doi: 10.1002/qj.2779.

Allen, D.R. and N. Nakamura, 2001: A seasonal climatology of effective diffusivity in the stratosphere. *J. Geophys. Res.*, **106**, 7917 - 7935, doi: 10.1029/2000JD900717.

Allen, D.R. and N. Nakamura, 2003: Tracer Equivalent Latitude: A Diagnostic tool for isentropic transport studies. *J. Atmos. Sci.*, **60**, 287 - 304, doi: 10.1175/1520-0469(2003)060<0287:TELADT>2.0.CO;2.

Appenzeller, C., J.R. Holton, and K.H. Rosenlof, 1996: Seasonal variation of mass transport across the tropopause. *J. Geophys. Res.*, **101**, 15,071 - 15,078, doi: 10.1029/96JD00821.

Berthet, G., J.G. Esler, and P.H. Haynes, 2007: A Lagrangian perspective of the tropopause and the ventilation of the lowermost stratosphere. *J. Geophys. Res.*, **112**, D18102, doi: 10.1029/2006JD008295.

Bethan, S., G. Vaughan, and S.J. Reid, 1996: A comparison of ozone and thermal tropopause heights and the impact of tropopause definition on quantifying the ozone content of the troposphere. *Q. J. R. Meteorol. Soc.*, **122**, 929 - 944, doi: 10.1002/qj.49712253207.

Birner, T., D. Sankey, and T.G. Shepherd, 2006: The tropopause inversion layer in models and analyses. *Geophys. Res. Lett.*, **33**, L14804, doi: 10.1029/2006GL026549.

Boothe, A.C. and C.R. Homeyer, 2017: Global large-scale stratosphere–troposphere exchange in modern reanalyses. *Atmos. Chem. Phys.*, **17**, 5537 - 5559, doi: 10.5194/acp-17-5537-2017.

Bowman, K.P., *et al.*, 2013: Input Data Requirements for Lagrangian Trajectory Models. *Bull. Amer. Meteorol. Soc.*, **94**, 1051 - 1058, doi: 10.1175/BAMS-D-12-00076.1.

Davis, S.M., *et al.*, 2017: Assessment of upper tropospheric and stratospheric water vapor and ozone in reanalyses as part of S-RIP. *Atmos. Chem. Phys.*, **17**, 12743 - 12778, doi: 10.5194/acp-17-12743-2017.

Forster, P.M. and K.P. Shine, 1999: Stratospheric water vapour changes as a possible contributor to observed stratospheric cooling. *Geophys. Res. Lett.*, **26**, 3309 - 3312, doi: 10.1029/1999GL010487.

Fujiwara, M., *et al.*, 2017: Introduction to the SPARC Reanalysis Intercomparison Project (S-RIP) and overview of the reanalysis systems. *Atmos. Chem. Phys.*, **17**, 1417 - 1452, doi: 10.5194/acp-17-1417-2017.

Gettelman, A., *et al.*, 2011: The extratropical upper troposphere and lower stratosphere. *Rev. Geophys.*, **49**, RG3003, doi: 10.1029/2011RG000355.

Gettelman, A. and T. Wang, 2015: Structural diagnostics of the tropopause inversion layer and its evolution. *J. Geophys. Res.*, **120**, 46 - 62, doi: 10.1002/2014JD021846.

Grise, K.M., *et al.*, 2013: The ozone hole indirect effect: Cloud-radiative anomalies accompanying the poleward shift of the eddy-driven jet in the Southern Hemisphere. *Geophys. Res. Lett.,* **40**, 1 - 5, doi: 10.1002/grl.50675.

Harnik, N., C.I. Garfinkel, and O. Lachmy, 2016: The influence of jet stream regime on extreme weather events. In J. Li, R. Swinbank, R. Grotjahn, & H. Volkert (Eds.), *Dynamics and Predictability of Large-Scale, High-Impact Weather and Climate Events* (Special Publications of the International Union of Geodesy and Geophysics, pp. 79-94). Cambridge: Cambridge University Press. doi: 10.1017/CBO9781107775541.007.

Haynes, P. and E. Shuckburgh, 2000a: Effective diffusivity as a diagnostic of atmospheric transport 1. Stratosphere. *J. Geophys. Res.*, **105**, 22,777 - 22,794, doi: 10.1029/2000JD900093.

Haynes, P. and E. Shuckburgh, 2000b: Effective diffusivity as a diagnostic of atmospheric transport 2. Troposphere and lower stratosphere. *J. Geophys. Res.*, **105**, 22,795 - 22,810, doi: 10.1029/2000JD900092.

Hegglin, M.I. and T.G. Shepherd, 2009: Large climate-induced changes in ultraviolet index and stratosphere-to-troposphere ozone flux. *Nature Geosci.*, **2**, 687 - 691, doi: 10.1038/ngeo604.

Hegglin, M.I., *et al.*, 2006: Measurements of NO, NO_y, N_2O, and O_3 during SPURT: implications for transport and chemistry in the lowermost stratosphere. *Atmos. Chem. Phys.*, *6*, 1331 - 1350, doi: 10.5194/acp-6-1331-2006.

Hegglin, M.I., *et al.*, 2016: The GAW/NDACC/SPARC Upper Troposphere and Lower Stratosphere (UTLS) Observation Workshop, *SPARC Newsletter*, **47**, 39 - 43, available at: **https://www.sparc-climate.org/publications/newsletter/**.

Hegglin, M.I. *et al.* 2010: Multi-model assessment of the upper troposphere and lower stratosphere: Extratropics. *J. Geophys. Res.*, **115**, D00M09, doi: 10.1029/2010JD013884.

Highwood, E.J., B.J. Hoskins, and P. Berrisford, 2000: Properties of the Arctic tropopause. *Q. J. R. Meteorol. Soc.*, **126**, 1515 - 1532, doi: 10.1002/qj.49712656515.

Hitchman, M.H. and A.S. Huesmann, 2007: A seasonal climatology of Rossby wave breaking in the 320 - 2000 - K layer. *J. Atmos. Sci.*, **64**, 1922 - 1940, doi: 10.1175/JAS3927.1.

Hoffmann, L., *et al.*, 2019: From ERA-Interim to ERA5: the considerable impact of ECMWF's next-generation reanalysis on Lagrangian transport simulations. *Atmos. Chem. Phys.*, **19**, 3097 - 3124, doi: 10.5194/acp-19-3097-2019.

Homeyer, C.R., 2014: Formation of the Enhanced-V Infrared Cloud Top Feature from High-Resolution Three-Dimensional Radar Observations. *J. Atmos. Sci.*, **71**, 332 - 348, doi: 10.1175/JAS-D-13-079.1.

Homeyer, C.R. and K.P. Bowman, 2013: Rossby wave breaking and transport between the tropics and extratropics above the subtropical jet. *J. Atmos. Sci.*, **70**, 607 - 626, doi: 10.1175/JAS-D-12-0198.1.

Homeyer, C., K.P. Bowman, and L.L. Pan, 2010: Extratropical tropopause transition layer characteristics from high-resolution sounding data. *J. Geophys. Res.*, **115**, D13108, doi: 10.1029/2009JD013664.

Homeyer, C.R., J.D. McAuliffe, and K.M. Bedka, 2017: On the Development of Above-Anvil Cirrus Plumes in Extratropical Convection. *J. Atmos. Sci.*, **74**, 1617 - 1633, doi: 10.1175/JAS-D-16-0269.1.

Homeyer, C.R., *et al.*, 2011: Dynamical and chemical characteristics of tropospheric intrusions observed during START08. *J. Geophys. Res.*, **116**, D06111, doi: 10.1029/2010JD015098.

Hood, L.L., B.E. Soukharev, M. Fromm, and J.P. McCormack, 2001: Origin of extreme ozone minima at middle to high northern latitudes. *J. Geophys. Res.: Atmos.*, **106**, 20 925 - 20 940, doi: 10.1029/2001JD900093.

Hoor, P., *et al.*, 2004: Seasonality and extent of extratropical TST derived from in-situ CO measurements during SPURT. *Atmos. Chem. Phys.*, **4**, 1427 - 1442.

Hubert, D., et al., 2016: Ground-based assessment of the bias and long-term stability of 14 limb and occultation ozone profile data records. *Atmos. Meas. Tech.*, **9**, 2497 - 2534, doi: 10.5194/amt-9-2497-2016.

Hudson, R.D., 2012: Measurements of the movement of the jet streams at mid-latitudes, in the Northern and Southern Hemispheres, 1979 to 2010. *Atmos. Chem. Phys.*, **12**, 7797 - 7808, doi: 10.5194/acp-12-7797-2012.

Jaeglé, L., R.Wood, and K. Wargan, 2017: Multiyear Composite View of Ozone Enhancements and Stratosphere-to-Troposphere Transport in Dry Intrusions of Northern Hemisphere Extratropical Cyclones. *J. Geophys. Res.*, **122**, 13,436 - 13,457, doi: 10.1002/2017JD027656.

James, P.M., 1998a: A climatology of ozone mini-holes over the northern hemisphere. *Int. J. Climatol.*, **18**, 1287 - 1303, doi: 10.1002/(SICI)1097-0088(1998100)18:12<1287::AID-JOC315>3.0.CO;2-4.

James, P.M., 1998b: An interhemispheric comparison of ozone mini-hole climatologies. *Geophys Res. Lett.*, **25**, 301 - 304, doi: 10.1029/97GL03643.

Knowland, K.E., L.E. Ott, B.N. Duncan, and K. Wargan, 2017: Stratospheric Intrusion-Influenced Ozone Air Quality Exceedances Investigated in the NASA MERRA-2 Reanalysis. *Geophys. Res. Lett.*, **44**, 10,691 - 10,701, doi: 10.1002/2017GL074532.

Koch, P., H. Wernli, and H.C. Davies, 2006.: An event-based jet-stream climatology and typology. *Int. J. Climatol.*, **26**, 283 - 301, 10.1002/joc.1255.

Koch, G., *et al.*, 2005: A composite study on the structure and formation of ozone miniholes and minihighs over central Europe. *Geophys. Res. Lett.*, **32**, L12810, doi: 10.1029/2004GL022062.

Kunkel, D., *et al.*, 2019: Evidence of small-scale quasi-isentropic mixing in ridges of extratropical baroclinic waves. *Atmos. Chem. Phys.*, **19**, 12 607 - 12 630, doi: 10.5194/acp-19-12607-2019.

Kunz, A., P. Konopka, R. Müller, and L.L. Pan, 2011b: Dynamical tropopause based on isentropic potential vorticity gradients. *J. Geophys. Res.*, **116**, D01110, doi: 10.1029/2010JD014343.

Kunz, A., M. Sprenger, and H. Wernli, 2015: Climatology of potential vorticity streamers and associated isentropic transport pathways across PV gradient barriers. *J. Geophys. Res. Atmos.*, **120**, 3802 - 3821, doi: 10.1002/2014JD022615.

Lacis, A., D.J. Wuebbles, J.A. and Logan, 1990: Radiative forcing of climate by changes in the vertical distribution of ozone. *J. Geophys. Res.*, **95**, 9971 - 9981, doi: 10.1029/JD095iD07p09971.

Lambert, A., *et al.*, 2008: Version 2.2 Level 2 near-real-time data user guide. *Tech. Rep. JPL* **D-48439**, Jet Propulsion Laboratory, 2008.

Lawrence, Z.D., G.L. Manney, and K. Wargan, 2018: Reanalysis intercomparisons of stratospheric polar processing diagnostics. *Atmos. Chem. Phys.*, **18**, 13 547 - 13 579, doi: 10.5194/acp-18-13547-2018.

Levelt, P.F., *et al.*, 2006: Science objectives of the ozone monitoring instrument. *IEEE T. Geosci. Remote* , **44**, 1199 - 1208, doi: 10.1109/TGRS.2006.872336.

Lin, M., *et al.*, 2014: Tropospheric ozone trends at Mauna Loa Observatory tied to decadal climate variability. *Nat. Geosci.*, **7**, 136 - 143, doi: 10.1038/ngeo2066.

Lin, M., *et al.*, 2015: Climate variability modulates western US ozone air quality in spring via deep stratospheric intrusions. *Nature Commun.*, **6**, doi: 10.1038/ncomms8105.

Livesey, N.J., *et al.*, 2018: EOS MLS Version 4.2x Level 2 data quality and description document. *Tech. rep.*, JPL, available t **https://mls.jpl.nasa.gov/data/v4-2_data_quality_document.pdf/**.

Long, C.S., *et al.*, 2017: Climatology and Interannual Variability of Dynamic Variables in Multiple Reanalyses Evaluated by the SPARC Reanalysis Intercomparison Project (S-RIP). *Atmos. Chem. Phys.*, **17**, 14,593 - 14,629, doi: 10.5194/acp-17-14593-2017.

Lorenz, D.J. and E.T. DeWeaver, 2007: Tropopause height and zonal wind response to global warming in the IPCC scenario integrations. *J. Geophys. Res.*, **112**, D10119, doi: 10.1029/2006JD008087.

Mahlman, J.D., 1997: Dynamics of Transport Processes in the Upper Troposphere. *Science*, **276**, 1079 - 1083, doi: 10.1126/science.276.5315.1079.

Mann, M.E., *et al.*, 2017: Influence of Anthropogenic Climate Change on Planetary Wave Resonance and Extreme Weather Events. *Sci. Rep.*, **7**, doi: 10.1038/srep45242.

Manney, G.L. and Z.D. Lawrence, 2016: The major stratospheric final warming in 2016: dispersal of vortex air and termination of Arctic chemical ozone loss. Atmos. Chem. Phys., 16, 15371–15396, doi.org 10.5194/acp-16-15371-2016.

Manney, G.L. and M.I. Hegglin, 2018a: Seasonal and Regional Variations in Long-Term Changes in Upper Tropospheric Jets from Reanalyses. *J. Clim.*, **31**, 423 - 448, doi: 10.1175/JCLI-D-17-0303.1.

Manney, G.L. and M.I. Hegglin, 2018b: Corrigendum for "Seasonal and Regional Variations in Long- Term Changes in Upper Tropospheric Jets from Reanalyses". *J. Clim.*, **31**, 1289 - 1293, doi: 10.1175/JCLI-D-17-0881.1.

Manney, G.L., *et al.*, 2005: EOS Microwave Limb Sounder observations of the Antarctic polar vortex breakup in 2004. *Geophys. Res. Lett.*, **32**, L12811, doi: 10.1029/2005GL022823, 2005.

Manney, G. L. *et al.,* 2009: Satellite observations and modeling of transport in the upper troposphere through the lower mesosphere during the 2006 major stratospheric sudden warming. *Atmos. Chem. Phys.*, **9**, 4775 - 4795, doi: 10.5194/acp-9-4775-2009.

Manney, G.L., *et al.*, 2011: Jet characterization in the upper troposphere/lower stratosphere (UTLS): applications to climatology and transport studies. *Atmos. Chem. Phys.*, **11**, 6115 - 6137, doi: 10.5194/acp-11-6115-2011.

Manney, G.L., *et al.*, 2014: Climatology of Upper Tropospheric/Lower Stratospheric (UTLS) Jets and Tropopauses in MERRA. *J. Clim.*, **27**, 3248 - 3271, doi: 10.1175/JCLI-D-13-00243.1.

Manney, G.L., et al., 2017: Reanalysis comparisons of upper tropospheric/lower stratospheric jets and multiple tropopauses. *Atmos. Chem. Phys.,* **17**, 11541 - 11566, doi: 10.5194/acp-17-11541-2017.

Martineau, P., J.S. Wright, N. Zhu, and M. Fujiwara, 2018: Zonal-mean data set of global atmospheric reanalyses on pressure levels. *Earth Sys. Sci. Data*, **10**, 1925 - 1941, doi: 10.5194/essd-10-1925-2018.

McIntyre, M.E. and T.N. Palmer, 1983: Breaking planetary waves in the stratosphere, *Nature*, **305**, 593 - 600, doi: 10.1038/305593a0.

McLandress, C., *et al.*, 2011: Separating the dynamical effects of climate change and ozone depletion. Part II: Southern Hemisphere troposphere. *J. Clim.*, **24**, 1850 - 1868, doi: 10.1175/2010JCLI3958.1.

Millán, L. and G.L. Manney, 2017: An assessment of Ozone Mini-holes Representation in Reanalyses Over the Northern Hemisphere. *Atmos. Chem. Phys.*, **17**, 9277 - 9289, doi: 10.5194/acp-17-9277-2017.

Millán, L.F., G.L. Manney, and Z.D. Lawrence, 2021: Reanalysis intercomparison of potential vorticity and potential-vorticity-based diagnostics. *Atmos. Chem. Phys.*, **21**, 5355 - 5376, doi: 10.5194/acp-21-5355-2021.

Newman, P.A., L.R. Lait, and M.R. Schoeberl, 1988: The morphology and meteorology of southern hemisphere spring total ozone mini-holes. *Geophys. Res. Lett.*, **15**, 923 - 926, doi: 10.1029/GL015i008p00923.

Olsen, M.A., M.R. Schoeberl, and A.R. Douglass, 2004: Stratosphere-troposphere exchange of mass and ozone. *J. Geophys. Res.*, **109**, D24114, doi: 10.1029/2004JD005186.

Olsen, M.A., A.R. Douglass, and T.B. Kaplan, 2013: Variability of extratropical ozone stratosphere- troposphere exchange using Microwave Limb Sounder observations. *J. Geophys. Res.*, **118**, 1090 - 1099, doi: 10.1029/2012JD018465.

Olsen, M.A., K. Wargan, and S. Pawson, 2016: Tropospheric column ozone response to ENSO in GEOS-5 assimilation of OMI and MLS ozone data. *Atmos. Chem. Phys.*, **16**, 7091 - 7103, doi: 10.5194/acp-16-7091-2016.

Orbe, C., *et al.*, 2018: Large-scale tropospheric transport in the Chemistry–Climate Model Initiative (CCMI) simulations. *Atmos. Chem. Phys.*, **18**, 7217 - 7235, doi: 10.5194/acp-18-7217-2018.

Pan, L.L., *et al.*, 2009: Tropospheric intrusions associated with the secondary tropopause. *J. Geophys. Res.*, **114**, D10 302, doi: 10.1029/2008JD011374.

Pan, L.L. *et al.*, 2010: The Stratosphere-Troposphere Analysis of Regional Transport 2008 Experiment. B*ull. Am. Meteor. Soc.*, **91**, 327 - 342, doi: 10.1175/2009BAMS2865.1.

Pilch Kedzierski, R., L. Neef, and K. Matthes, 2016: Tropopause sharpening by data assimilation. *Geophys. Res. Lett.*, **43**, 8298 - 8305, doi: 10.1002/2016GL069936.

Prather, M.J., *et al.*, 2011: An atmospheric chemist in search of the tropopause. *J. Geophys. Res.*, **116**, D04306, doi: 10.1029/2010JD014939.

Randel, W.J., D.J. Seidel, and L. Pan, 2007: Observational characteristics of double tropopauses. *J. Geophys. Res.*, **112**, D07309, doi: 10.1029/2006JD007904.

Reutter, P., B. Škerlak, M. Sprenger, and H. Wernli, 2015: Stratosphere-troposphere exchange (STE) in the vicinity of North Atlantic cyclones. *Atmos. Chem. Phys.*, **15**, 10,939 - 10,953, doi: 10.5194/acp-15-10939-2015.

Riese, M., *et al.*, 2012: Impact of uncertainties in atmospheric mixing on simulated UTLS composition and related radiative effects. J. *Geophys. Res. Atmos.*, **117**, D16305 , doi: 10.1029/2012JD017751.

Santee, M.L., *et al.*, 2011: Trace gas evolution in the lowermost stratosphere from Aura Microwave Limb Sounder measurements. *J. Geophys. Res.*, **116**, D18306, doi: 10.1029/2011JD015590.

Schoeberl, M.R., 2004: Extratropical stratosphere-troposphere mass exchange. *J. Geophys. Res.*, **109**, D13303, doi: 10.1029/2004JD004525.

Schwartz, M.J., *et al.*, 2015: Climatology and variability of trace gases in extratropical multiple tropopause regions from MLS, HIRDLS and ACE-FTS measurements. *J. Geophys. Res.*, **120**, 843 - 867, doi: 10.1002/2014JD021964.

Seo, K. and K.P. Bowman, 2002: Lagrangian estimate of global stratosphere-troposphere mass exchange. *J. Geophys. Res.*, **107**, 4555, doi: 10.1029/2002JD002441.

Škerlak, B., M. Sprenger, and H. Wernli, 2014: A global climatology of stratosphere-troposphere exchange using the ERA-Interim data set from 1979 to 2011. *Atmos. Chem. Phys.*, **14**, 913 - 937, doi: 10.5194/acp-14-913-2014.

Škerlak, B., et al., 2015: Tropopause folds in ERA-Interim: Global climatology and relation to extreme weather events. *J. Geophys. Res. Atmos.*, **120**, 4860 - 4877, doi: 10.1002/2014JD022787.

Solomon, D.L., K.P. Bowman, and C.R. Homeyer, 2016: Tropopause-Penetrating Convection from Three-Dimensional Gridded NEXRAD Data. *J. Appl. Meteor. Climatol.*, **55**, 465 - 478, doi: 10.1175/JAMC-D-15-0190.1.

Solomon, S., *et al.*, 2010: Contributions of stratospheric water vapor to decadal changes in the rate of global warming. *Science*, **327**, 1219 - 1223, doi: 10.1126/science.1182488.

Song, J., C. Li, J. Pan, and W. Zhou, W., 2011: Climatology of anticyclonic and cyclonic Rossby wave breaking on the dynamical tropopause in the southern hemisphere. *J. Clim.*, **24**, 1239 - 1251, doi: 10.1175/2010JCLI3157.1, 2011.

Sprenger, M. and H. Wernli, H., 2003: A northern hemispheric climatology of cross-tropopause exchange for the ERA15 time period (1979-1993). *J. Geophys. Res.*, **108**, 8521, doi: 10.1029/2002JD002636.

Sprenger, M., M.C. Maspoli, and H. Wernli, 2003: Tropopause folds and cross-tropopause exchange: A global investigation based upon ECMWF analyses for the time period March 2000 to February 2001. *J. Geophys. Res.*, **108**, 8518, doi: 10.1029/2002JD002587.

Sprenger, M., H. Wernli, and M. Bourqui, 2007: Stratosphere-troposphere exchange and its relation to potential vorticity streamers and cutoffs near the extratropical tropopause. *J. Atmos. Sci.*, 64, 1587–1602, doi: 10.1175/JAS3911.1, 2007.

Stohl, A., 1998: Computation, accuracy and applications of trajectories—A review and bibliography. *Atmos. Environ.*, **32,** 947 - 966**,** doi: 10.1016/S1352-2310(97)00457-3.

Stohl, A.:, 2001 A 1-year Lagrangian "climatology" of airstreams in the northern hemisphere troposphere and lowermost stratosphere. *J. Geophys. Res.*, **106**, 7263 - 7279, doi: 10.1029/2000JD900570.

Wang, P.K., *et al.*, 2016a: The origin of the gullwing-shaped cirrus above an Argentinian thunderstorm as seen in CALIPSO images. J. *Geophys. Res. Atmos.*, **121**, 3729 - 3738, doi: 10.1002/2015JD024111.

Wang, R., *et al.*, 2016b: A mechanism to explain the variations of tropopause and tropopause inversion layer in the Arctic region during a sudden stratospheric warming in 2009. *J. Geophys. Res.*, **121**, 11 932 - 11 945, doi: 10.1002/2016JD024958.

Wargan, K. L. and Coy, 2016: Strengthening of the Tropopause Inversion Layer during the 2009 Sudden Stratospheric Warming: A MERRA-2 Study. *J. Atmos. Sci.*, **73**, 1871 - 1887, doi: 10.1175/JAS-D-15-0333.1.

Wargan, K., *et al.*, 2017: Evaluation of the Ozone Fields in NASA's MERRA-2 Reanalysis. *J. Clim.*, **30**, 2961 - 2988, doi: 10.1175/JCLI-D-16-0699.1.

Waters, J.W., et al., 2006: The Earth observing system microwave limb sounder (EOS MLS) on the aura Satellite. *IEEE T Geosci Remote*, **44**, 1075 - 1092, doi: 10.1109/TGRS.2006.873771.

Waugh, D.W., C.I. Garfinkel, and L.M. Polvani, 2015: Drivers of the Recent Tropical Expansion in the Southern Hemisphere: Changing SSTs or Ozone Depletion? *J. Clim.*, **28**, 6581 - 6586, doi: 10.1175/JCLI-D-15-0138.1.

Wernli, H. and M. Bourqui, M., 2002: A Lagrangian "1-year climatology" of (deep) cross-tropopause exchange in the extratropical northern hemisphere. *J. Geophys. Res.*, **107**, 4021, doi: 10.1029/2001JD000812.

WMO, 2011: Scientific assessment of ozone depletion: 2010, *Global Ozone Res. and Monit. Proj. Rep*. **52**, 516 pp., Geneva, Switzerland.

World Meteorological Organization: Meteorology, 1957: A three-dimensional science: Second session of the commission for aerology. *World Meteorol. Organ. Bull.*, **4**, 134 - 138, 1957.

Xian, T. and C.R. Homeyer, 2019: Global Tropopause Altitudes in Radiosondes and Reanalyses. *Atmos. Chem. Phys.*, **19**, 5661 - 5678, doi: 10.5194/acp-19-5661-2019.

Zeng, G., O. Morgenstern,P. Braesicke, and J.A. Pyle, 2010: Impact of stratospheric ozone recovery on tropospheric ozone and its budget. *Geophys. Res. Lett.*, **37**, L09805, doi: 10.1029/2010GL042812, 2010.

Major abbreviations and terms

ACE-FTS	
ANA	Analyzed, referring to MERRA and MERRA-2 products from the analysis step (see *Chapter 2*)
ASM	Assimilated, referring to MERRA and MERRA-2 products from assimilation step (see *Chapter 2*)
ATOVS	Advanced TIROS Operational Vertical Sounder
CFSR	Climate Forecast System Reanalysis of the NCEP
CFSv2	Climate Forecast System version 2
CONUS	CONtiguous United States
CTM	Chemical Transport Model
DJF	December/January/February
DOE	Department of Energy
DT	Double Tropopause
ECMWF	European Centre for Medium-range Weather Forecasts
ENSO	El Niño Southern Oscillation
Eq	Equivalent Latitude
ERA-40	ECMWF 40-year reanalysis
ERA-Interim	ECMWF interim reanalysis
ExLS	Extratropical Lower Stratosphere
ExUTLS	Extratropical Upper Troposphere and Lower Stratosphere
GMAO	Global Modeling and Assimilation Office
GNSS-RO	Global Navigation Satellite System - Radio Occultation
IAGOS	In-service Aircraft for a Global Observing System
JETPAC	JEt and Tropopause Products for Analysis and Characterization
JJA	June/July/August
JRA-55	Japanese 55-year Reanalysis
K_{eff}	Effective Diffusivity
LMS	LowerMost Stratosphere
LRT	Lapse-Rate Tropopause
LS	Lower Stratosphere
MAM	March/April/May

MERRA	Modern Era Retrospective-Analysis for Research and Applications
MERRA-2	Modern Era Retrospective-Analysis for Research and Applications, Version 2
MLS	Microwave Limb Sounder
NCAR	National Center for Atmospheric Research
NCEP	National Centers for Environmental Prediction of the NOAA
NCEP-DOE R2	Reanalysis 2 of the NCEP and DOE
NCEP-NCAR R1	Reanalysis 1 of the NCEP and NCAR
NASA	National Aeronautics and Space Administration
NH	Northern Hemisphere
NRT	Near Real Time
NWS	National Weather Service
OCTAV-UTLS	Observed Composition Trends And Variability in the Upper Troposphere/Lower Stratosphere
OMI	Ozone Monitoring Instrument
OSIRIS	Optical Spectrograph and InfraRed Imaging System
PJ	Polar Jet
PV	Potential Vorticity
PVU	PV units (defined as 10^{-6} K m^2 (kg s)$^{-1}$)
QBO	Quasi-Biennial Oscillation
REM	Reanalysis Ensemble Mean
rms	root mean square
SH	Southern Hemisphere
SON	September/October/November
sPV	scaled Potential Vorticity
START-08	Stratosphere-Troposphere Analyses of Regional Transport 2008
STE	Stratosphere-Troposphere Exchange
STJ	SubTropical Jet
STT	Stratosphere-to-Troposphere Transport
TIROS	The Television Infrared Observation Satellite Program
TOVS-ATOVS	TIROS Operational Vertical Sounde
TST	Troposphere-to-Stratosphere Transport
TTL	Tropical Tropopause Layer
UT	Upper Troposphere
UTLS	Upper Troposphere and Lower Stratosphere
WISE	Wave-driven ISentropic Exchange
WMO	World Meteorological Organization